

(two dislocations of the same sign on the same plane). These dislocation pairs are discussed in more detail in chapters 4 and 5. As shown in figure 3.8, if the two dislocations are of the same type and sense then, when  $\underline{g}$  is reversed, both the images will move in the same direction and there will be no change in image spacing (fig. 3.8a). However, if the dislocations are of opposite sign, then the image spacing will change when  $\underline{g}$  is reversed (fig. 3.8b). Simply, then, if the image spacing changes on reversing  $\underline{g}$  then the dislocation pair is usually a dipole. If it does not change the dislocation pair is a superdislocation. The technique was first described and used by Bell, Roser and Thomas (1964) to distinguish between superdislocations and dipoles in austenitic stainless steels,  $\alpha$ -brasses and Cu-Sn solid solutions. There is one discrepancy which must be considered when looking at a superdislocation which is dissociated into four partial dislocations as shown in figure 3.9. If this is the case an apparent change in image spacing will be observed if  $\underline{b}_3$  is in contrast for  $+\underline{g}$  and out of contrast for  $-\underline{g}$  and  $\underline{b}_2$  is out of contrast for  $+\underline{g}$  and in contrast for  $-\underline{g}$ . The apparent spacing change will only occur when  $\underline{g}\cdot\underline{b}=\pm\frac{2}{3}$  and  $\pm\frac{4}{3}$ . If  $\underline{g}\cdot\underline{b}$  for the partials is integral, then the image characteristics for any  $\pm\underline{g}$  pair will be as for undissociated superdislocations.

The  $\pm\underline{g}$  pair provides a method of distinguishing between dipoles, superdislocations and dissociated superdislocations.

### 3.3.8 Contrast from stacking faults

The Howie-Whelan equations stated in eqn. 3.2 can be applied to provide a description of the contrast from stacking faults. If a stacking fault is present in a lattice and inclined to the surface of the foil, then the introduction of the phase factor  $\alpha=2\pi\underline{g}\cdot\underline{R}$  creates interference between the transmitted and diffracted waves.  $\alpha$  can have a range of values from 0 to  $2\pi$  depending on  $\underline{R}$ . The specific case of  $\alpha=\pi$  is discussed as a special case in 3.3.9.

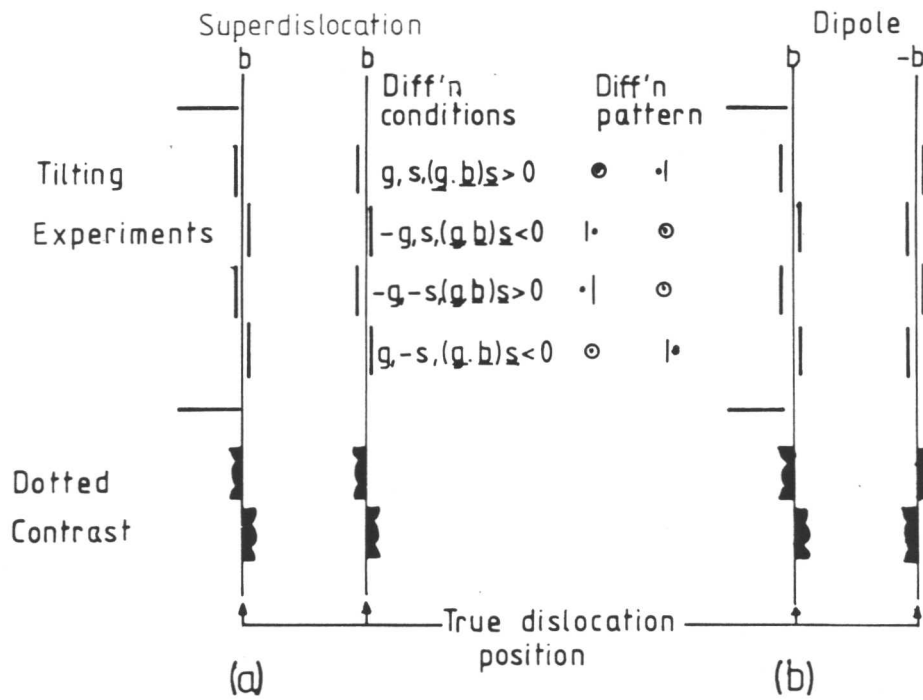


Fig. 3.8. Schematic diagram illustrating the technique for distinguishing between superdislocations and dipoles. When both dislocations are the same there will be no change in spacing when  $g$  is reversed (a). If the dislocations are opposite the image spacing changes on reversing  $g$  (b) (after Bell et al., 1964).

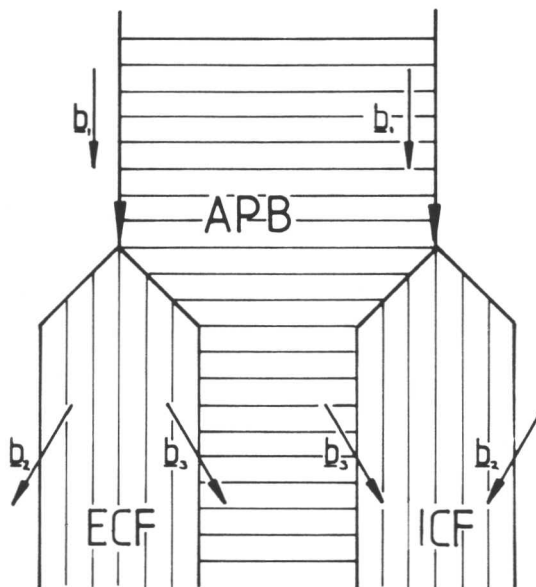


Fig. 3.9. Possible dissociation of a superdislocation to form an extrinsic and an intrinsic fault.  $b_1 = a/2[\bar{1}01]$ ,  $b_2 = a/6[\bar{2}11]$  and  $b_3 = a/6[\bar{1}\bar{1}2]$ .

By way of example consider a stacking fault on a  $\{111\}$  plane of an FCC material. As shown in 4.2 stacking faults in  $L1_2$  structures are different from those in FCC structures but the principle behind their identification in the TEM is the same. In FCC materials stacking faults can be formed either by the splitting of an  $a/2\langle 110 \rangle$  dislocation under a shear stress to form a fault bounded by two  $a/6\langle 211 \rangle$  partial dislocations or by the growth or aggregation of point defects, the fault being bounded by an  $a/3\langle 111 \rangle$  edge loop. Two types of fault exist: the intrinsic stacking fault which is equivalent to the removal of a (111) plane giving an ABCABABC stacking sequence, or the extrinsic stacking fault which is equivalent to the inclusion of an extra (111) plane giving an ABCABACABC stacking sequence. The fault vector,  $\underline{R}$ , is  $\pm\frac{1}{3}[111]$  and  $\alpha=0, \pm\frac{2}{3}\pi, \pm\frac{4}{3}\pi$ , etc. Whelan and Hirsch (1957a,b) studied the contrast arising from these faults and they have shown that when  $\underline{g}\cdot\underline{R}$  is integral the fault is invisible. When  $\underline{g}\cdot\underline{R}$  is non-integral the bright field image will consist of a series of dark and bright fringes running parallel to the intersection of the fault with foil surface (fig. 3.10). In bright field both the outer fringes are either dark or light and the image is symmetric. In dark field the outer fringes are not the same and the image is asymmetric. The intrinsic/extrinsic nature of faults can be determined from this contrast variation. The simplest method has been described by Gevers, Art and Amelinckx (1963) which uses the asymmetric dark field image. If the origin of  $\underline{g}$  is placed at the fault centre when  $\underline{g}$  points away from the light outer fringe the fault is extrinsic and if it points towards the light outer fringe it is intrinsic for Class A reflections ( $\{200\}$ ,  $\{222\}$  and  $\{440\}$ ) and the reverse is true for Class B reflections ( $\{400\}$ ,  $\{111\}$  and  $\{220\}$ ).

An analysis of the fringe contrast from stacking faults cannot distinguish between those created by shear and those created by point defect aggregation because a lattice translation vector can be added to the

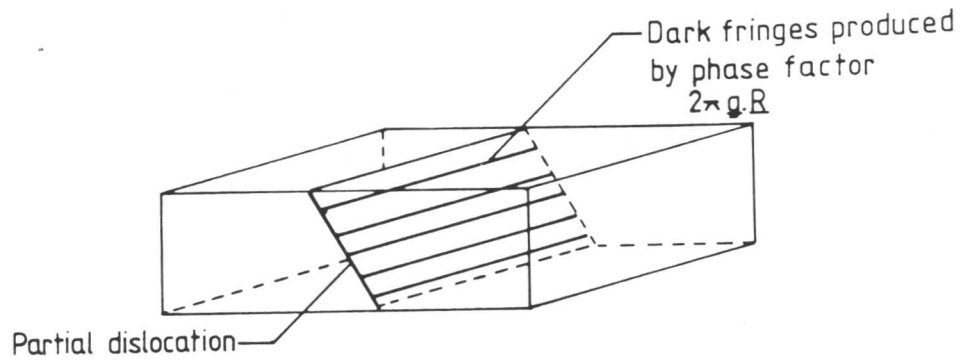


Fig. 3.10. Schematic diagram of a stacking fault lying on a plane which intersects the foil surface showing the dark fringes produced by the phase factor.

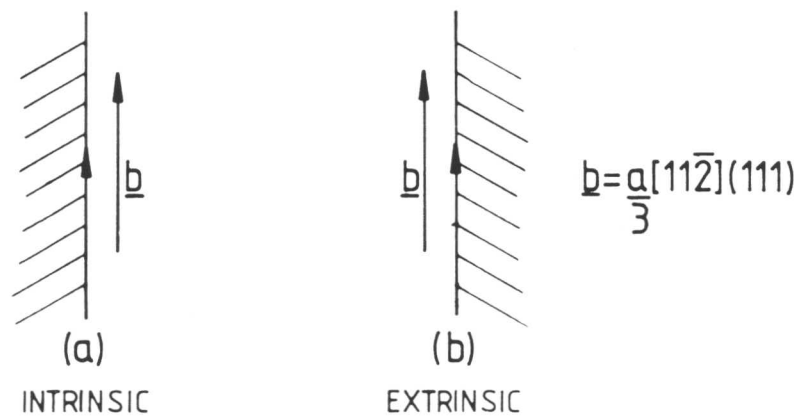


Fig. 3.11. Illustration showing the technique used to identify superlattice stacking faults from the bounding partial dislocation for superlattice intrinsic stacking faults (a), and superlattice extrinsic stacking faults (b).

shear displacement,  $a/6\langle 211 \rangle$ , to produce an  $a/3\langle 111 \rangle$  fault. If it is necessary to distinguish between the fault types the Burgers vectors of the bounding dislocations must be determined.

Stacking faults lying parallel to the foil surface (e.g. those on (111) in a [111] foil) do not exhibit fringe contrast. However, the phase change,  $\alpha = 2\pi \underline{g} \cdot \underline{R}$ , still occurs and contrast will result from the fault except when  $\underline{g} \cdot \underline{R}$  takes an integral value. The rules for fault nature determination as outlined above cannot be applied to faults totally enclosed within the foil. However, if the Burgers vector of the bounding partial dislocation and its line sense are determined as described in 3.3.5 and 3.3.6 then the fault nature may be determined as follows. If the stacking fault lies to the left of a bounding  $a/3\langle 211 \rangle$  screw partial dislocation it is an intrinsic stacking fault, but if the stacking fault lies to the right of the same bounding partial it is an extrinsic stacking fault (fig. 3.11). Further confirmation of the nature of flat faults can be gained by use of the anomalous contrast from weak beam images of extrinsic stacking faults. This effect was first noted in silicon by Cullis and Booker (1972); they reported that extrinsic stacking faults showed a marked change in contrast when imaged using  $+\underline{g}$  and  $-\underline{g}$  beams but that intrinsic faults showed no such anomaly. Later, Föll, Carter and Wilkens (1980) showed that the contrast anomaly was much weaker for  $\underline{g} = (111)$  than other reflections and that there was a slight but weak anomaly from intrinsic stacking faults. The origins of the contrast anomaly have since been studied by Self, Shaw and Stobbs (1982) and Cockayne, Pirouz, Liu, Anstis and Karnthaler (1984) who used a Bloch wave approach. In this investigation, where possible, the anomaly has been qualitatively applied to support the results gained by the determination of the Burgers vector bounding the faults. Only (200) and (220) reflections have been used and in many cases any contrast change was indistinguishable from changes in dislocation contrast as the faults, particularly the intrinsic faults, were very small.

### 3.3.9 Contrast from APBs

The contrast from APBs is similar to that described in 3.3.8 but for fundamental reflections in ordered materials the phase factor,  $\alpha = 2\pi \underline{g} \cdot \underline{R}$ , can only take the values  $0, 2\pi, 4\pi$ , etc. because  $\underline{R}$  is a lattice vector of the disordered lattice. This means that the APB is always invisible in fundamental reflections. For superlattice reflections  $\alpha$  can take the values  $0, \pi, 2\pi$ , etc. so fringe contrast will occur from inclined faults when  $\alpha = (2n-1)\pi$ . The contrast is due to the ~~change in phase~~ change in phase across the APB because of the change in the ordering sequence (4.2.2). When  $\underline{\omega} = 0$  the dark field and bright field images are symmetric about the centre of the foil. When  $\underline{\omega} > 0$  the bright field image is still symmetric, but the dark field image is not. It has proved impossible to image APBs using the  $\gamma'$  superlattice reflections. This is probably due to the large extinction distance of  $\gamma'$ . No values have been calculated for the  $\gamma'$  of the alloys studied in this investigation but Oblak and Kear (1972) quote extinction distances for  $\gamma'$  superlattice reflections in Mar-M 200 (table 3.1).

### 3.3.10 Stereo pairs

Many of the dislocation configurations created by deformation and annealing had complex forms. To aid glide plane determination (6.2.2) and analysis many stereo pairs were taken using tilts of between  $12-14^\circ$ . A two beam condition was set up and the image recorded. The foil was then tilted along the Kikuchi lines associated with the chosen reflection until the necessary tilt had been applied and an equivalent image recorded with the same diffraction conditions. After printing and marking  $\underline{g}$  onto the micrographs they were viewed in a stereoviewer with  $\underline{g}$  along the tilt axis. No quantitative measurements were performed on these images: they were only used to give a qualitative representation of the dislocation configurations.

### 3.3.11 Tilting experiments

To determine the habit plane of a screw superdislocation a tilting experiment can be performed. If a  $\underline{g}$  vector parallel to the dislocation line is chosen the dislocation can be tilted *clockwise* or *anticlockwise* around this  $\underline{g}$  and if the tilt is measured it is possible to evaluate the superdislocation habit plane from its change in spacing on tilting. An experiment of this type was performed once in this investigation.

## CHAPTER 4

### PLANAR DEFECTS AND HEXAGONAL DISLOCATION NETWORKS

#### 4.1 Introduction

Dislocation configurations of many diverse types have been predicted and observed in  $L1_2$  structures. Many papers have been published about these interactions, for instance, Flinn (1960) on all  $L1_2$  structures, Kear (1974), Staton-Bevan and Rawlings (1975(a) and (b)) and Nicholls and Rawlings (1977) on  $\gamma'$  in Ni-base alloys, Kear and Wilsdorf (1962) on  $Cu_3Au$ , Takeuchi, Kuramoto, Yamamoto and Taaka (1973) and Suzuki, Ichihara and Takeuchi (1979) on  $Ni_3Ga$  and Howe et al. (1974) on  $Zr_3Al$ . According to Yamaguchi, Vitek and Pope (1981), almost forty different  $L1_2$  alloys have been studied in some way. Most of these studies have been brought together in the most comprehensive review of the deformation and mechanical properties of  $L1_2$  related alloys by Pope and Ezz (1984).

These investigations have shown that the deformation of  $L1_2$  structures can be temperature and strain rate sensitive, can occur on one or more planes of the same or different types, and that dislocation interaction can occur between groups of identical or different dislocations. Because of the immense complexity of the possible deformation mechanisms, this chapter and chapter 5 are limited to the interactions observed in the  $\gamma'$  of alloys A-G. Where necessary, reference has been made to the work of others but no attempt has been made to review all the available literature. The results presented here are those which were considered to be relevant to the evaluation of the anti-phase boundary (APB) and superlattice stacking fault energies (SSF) and those which may help in the explanation of the alloy deformation mechanisms.

Three main types of planar defects can be formed in the  $L1_2$  structure. They are the APB, the complex fault (CF) and the two SSFs. This chapter describes the planar defects which can occur and discusses how these are related to the bounding dislocations when the defects are created by shear. It goes on to report the dislocation configurations in annealed, and annealed and deformed TEM foils. The major part of the chapter, 4.5, is devoted to the formation and observation of superlattice nodes (supernodes) and hexagonal dislocation networks. The creation of these networks is shown to be important to the evaluation of the fundamental defect energies.

## 4.2 Planar Defects in the $L1_2$ Structure

### 4.2.1 The $L1_2$ structure

The ordered  $L1_2$  structure has the chemical formula  $A_3B$ . Gamma prime has the  $L1_2$  structure and for convenience will be referred to as  $Ni_3Al$  or  $Ni_3(Al,Ti)$ , although in most commercial superalloys it contains significant amounts of alloying additions (1.5). It has already been reported that the  $\gamma'$  of alloys A-G has atomic species other than the Ni and Al within its structure (2.6.2).

Disordered  $Ni_3Al$  has the FCC structure where the shortest lattice repeat distance is  $a/2\langle 110 \rangle$ . On ordering the structure becomes primitive cubic; the shortest lattice repeat being  $a\langle 110 \rangle$ . This lattice can be thought of as four interpenetrating simple cubic lattices, figure 4.1 (Fisher and Marcinkowski, 1961). The lattice has four lattice sites as shown: 1 at  $(0,0,0)$ ; 2 at  $(0, \frac{1}{2}, \frac{1}{2})$ ; 3 at  $(\frac{1}{2}, 0, \frac{1}{2})$  and 4 at  $(\frac{1}{2}, \frac{1}{2}, 0)$ . Perfectly ordered  $Ni_3Al$  is usually said to have site 1 occupied by Al while 2, 3 and 4 are all occupied by Ni. In fact, any one of the sites may be occupied by Al as long as the others are occupied by Ni.

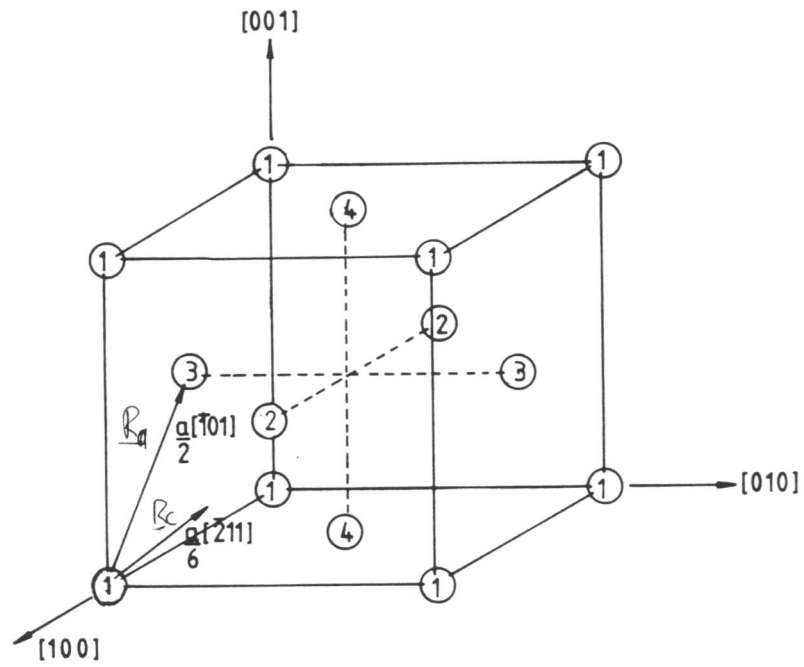


Fig. 4.1. Diagram of the  $L1_2$  structure showing the four lattice sites (1, 2, 3 and 4) and the APB and CF displacements  $\underline{R}_a$  and  $\underline{R}_c$  respectively.

#### 4.2.2 Antiphase boundaries in $L1_2$ structures

In  $L1_2$  APBs can lie on any plane. In many cases the APB energy is not increased significantly by displacements from the glide plane (Hirth and Lothe, 1982). In fact, in  $L1_2$  the APB energy may well be considerably decreased by such a displacement (Flinn, 1960). The most important APBs for the purposes of this discussion lie on  $\{111\}$  and  $\{001\}$ . Only these will be discussed in detail, although those displaced from these planes will be mentioned in 4.5.2.

To create an APB an Al atom must be displaced from a corner site (1) to a face centred site (2, 3 or 4), see figure 4.1. A (111) section is shown in figure 4.2. In figures 4.1 and 4.2 the vector  $\underline{R}_a (=a/2[\bar{1}01])$  is the displacement necessary to create an APB on the (111) plane. The vectors  $a/2[\bar{1}10]$  and  $a/2[01\bar{1}]$  are exactly equivalent to  $a/2[\bar{1}01]$ , therefore there are three displacement vectors associated with APBs on each of the  $\{111\}$  planes. When an APB is created on  $\{111\}$  a certain number of incorrect nearest neighbours are produced (fig. 4.3b). These nearest neighbour violations will contribute to the fault energy.

As shown in figure 4.4, the  $\underline{R}_a$  displacement can also be made to create an APB on the (001) plane. In this case there are only two equivalent displacement vectors on each  $\{001\}$  plane. When an APB is created on  $\{001\}$  there is no change in <sup>the</sup> first order nearest neighbours distribution, but there is in <sup>the</sup> second order nearest neighbours. (fig. 4.3c).

Flinn (1960) derived expressions for the APB energy on both the  $\{111\}$  and  $\{001\}$  planes by calculating the increase in energy when 'wrong' first order nearest neighbour bonds were created by an  $\underline{R}_a$  displacement. He ignored the second order nearest neighbour interactions and consequently found the  $\{001\}$  APB energy to be zero. This is clearly not true as second order interactions do contribute to the overall APB energy; a better expression considering second order interactions is that presented by Yamaguchi et al. (1981). Despite the difference in com-

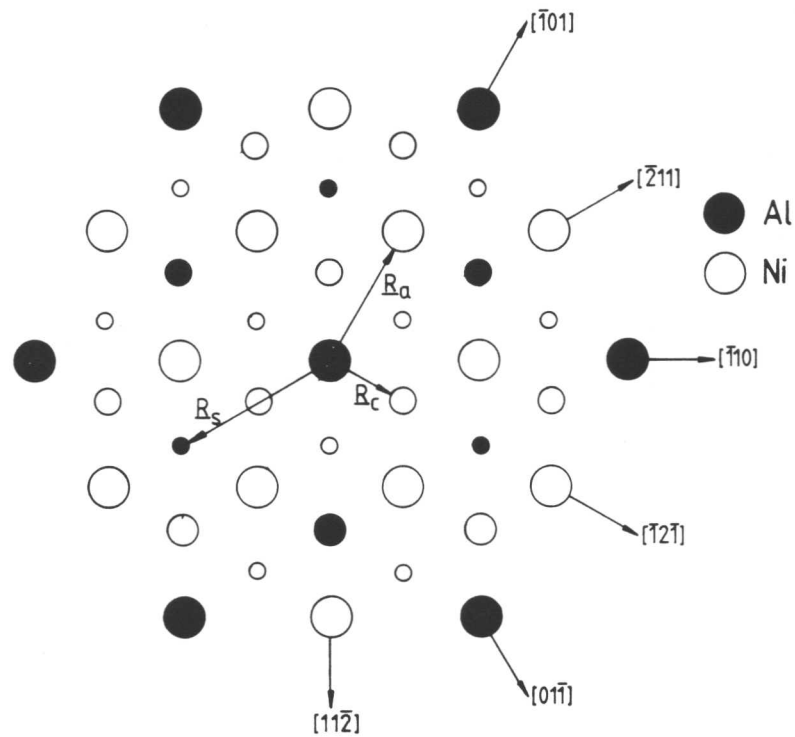


Fig. 4.2. Plan view of (111) planes in the L1<sub>2</sub> lattice. The full circles represent atomic species which occupy Al sites and open circles represent atomic species which occupy Ni sites. Large, medium and small circles represent a, b and c layers respectively. The diagram shows examples of the displacement vectors required to produce an APB ( $\underline{R}_a = a/2 [\bar{1}01]$ ), a CF ( $\underline{R}_c = a/6 [\bar{1}2\bar{1}]$ ) and an SSF ( $\underline{R}_s = a/3 [2\bar{1}\bar{1}]$ ) on the (111) plane.

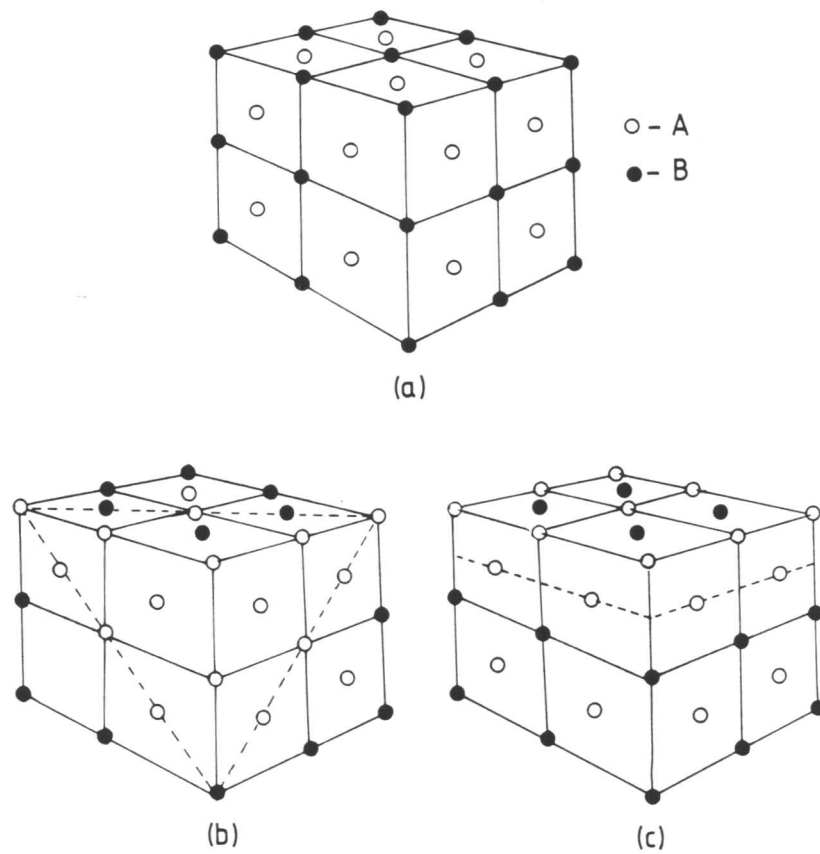


Fig. 4.3. The  $L1_2$  structure (a), with a displacement of  $a/2 \langle 110 \rangle$  on the  $\{111\}$  plane (b), and with a displacement of  $a/2 \langle 110 \rangle$  on the  $\{001\}$  plane (c).

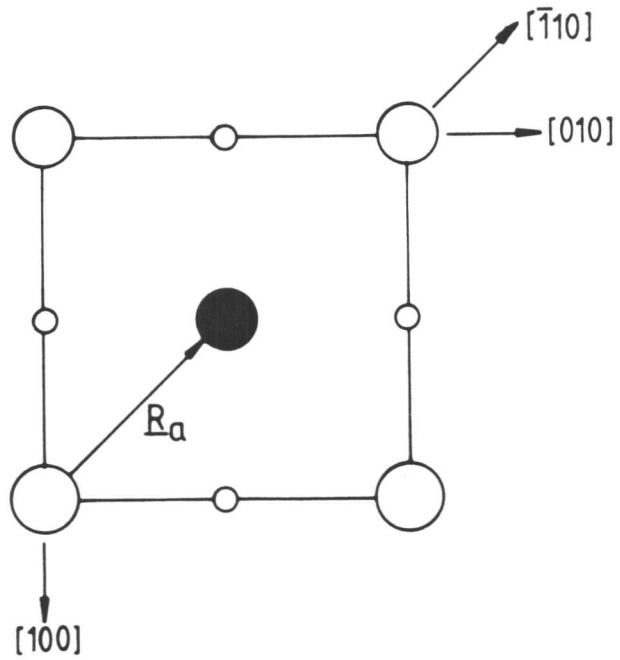


Fig. 4.4. Plan view of (001) planes in the  $L1_2$  lattice showing an example of the displacement vector required to produce an APB ( $\underline{R}_a = a/2[\bar{1}10]$ ) on the (001) plane. The symbols have the same meanings as figure 4.2.

putation, both authors report that the  $\{001\}$  APB has a considerably lower energy than the  $\{111\}$  APB and consequently should be more stable. Yamaguchi et al. studied the stability of APBs, on  $\{111\}$  and  $\{001\}$ , superlattice intrinsic stacking faults (SISFs) and complex faults (CFs), using a central force potential to calculate the  $\gamma$ -surface energy.

In this way they have shown that an APB will always have the lowest fault energy on a  $\{001\}$  plane and will therefore always be the most stable defect. The energy of an APB on a  $\{111\}$  plane increases as the degree of ordering increases; thus they showed that in highly ordered structures the APB energy may be too high for a stable APB to form.

#### 4.2.3 Complex faults in $L1_2$ structures

In the FCC structure an  $a/6\langle 211 \rangle$  displacement vector on  $\{111\}$  produces an intrinsic or an extrinsic stacking fault. However, when this displacement is applied to  $L1_2$  (figs. 4.1 and 4.2), a  $\{111\}$  APB is produced in addition to a stacking fault. This combination is known as a complex fault (Marcinkowski, 1963). The vector shown in figure 4.1 is  $a/6[\bar{2}11]$  and in figure 4.2 is  $a/6[\bar{1}2\bar{1}]$ . There are twelve equivalent  $a/6\langle 211 \rangle$  displacements which will produce complex faults. In common with the FCC lattice, CFs can be either intrinsic or extrinsic. No CF can exist on  $\{001\}$  because it is not possible for necessary displacements to be made on these planes.

It is expected that at room temperature the energy of a CF will be considerably larger than that of an APB. Yamaguchi et al. (1981) state that  $\gamma$ -surface calculations show that, in some instances, CFs may be stable in weakly ordered materials when they have energies lower than the APB energy.

#### 4.2.4 Superlattice stacking faults in $L1_2$ structures

As the shortest lattice repeat in  $L1_2$  is twice that in FCC it is

logical to assume that the displacement required to produce a fault equivalent to an FCC stacking fault should be doubled. This is found to be true and a displacement of  $a/3[2\bar{1}\bar{1}]$  (fig. 4.2) produces an SSF. In common with the CF there are twelve equivalent  $a/3\langle 211 \rangle$ s which will produce SSFs. The same fault can also be created by an  $a/3\langle 111 \rangle$  climb displacement. The concept of the SSF was first suggested by Carnahan, Cullen, Demel, McIlwain, Marcinkowski, Munford, Pahlman, Prevender and Warner (1967) who showed that the fault could have intrinsic or extrinsic character and when created the first and second nearest neighbours are unchanged.

It is worth noting that if the stacking sequence of ordered  $\text{Ni}_3\text{Al}$  is assumed to be ABCABCABC, then the stacking sequence of a superlattice intrinsic stacking fault (SISF) is ABCABABABC, which is equivalent to four layers of the  $\text{DO}_{19}$  structure or  $\text{DO}_{24}$  structure. The stacking sequence of a superlattice extrinsic stacking fault (SESF) is ABCABACABACABC which is equivalent to seven layers of the  $\text{DO}_{24}$  structure (Kear et al., 1968 and Kear et al., 1970).

Yamaguchi et al. (1981) found SISFs to be stable irrespective of ordering energy. They did not study the SESF but the results are expected to be the same. It is thought that under certain conditions the SSF energy and APB energy will be similar, and that they will compete for existence. This competition is likely to have a significant effect on the mechanical behaviour of the alloys. The effects of this type of interaction are discussed in detail in chapters 6 and 7.

In their papers, Yamaguchi and co-workers (Yamaguchi et al., 1981 and Yamaguchi, Paidar, Pope and Vitek, 1982) state that their computer modelling techniques predict that the displacement vectors of the faults described may deviate slightly from the exact values. No attempt was made to measure the exact displacement vectors. It was felt that any deviation would be so small that it could be assumed to be negligible.

### 4.3 Shear Dislocations in the $L1_2$ Structure

#### 4.3.1 Nomenclature

In FCC structures  $a/2\langle 110 \rangle$  dislocations are known as perfect dislocations because the passage of one leaves perfect crystal behind and has no effect on the crystal stacking.  $a/6\langle 211 \rangle$  dislocations are known as partial dislocations because their passage changes the crystal stacking sequence.

In  $L1_2$  an  $a\langle 110 \rangle$  dislocation is a perfect dislocation. An  $a/2\langle 110 \rangle$  dislocation has no effect on the crystal stacking sequence but does change the chemical bonding.  $a/3\langle 211 \rangle$  and  $a/6\langle 211 \rangle$  dislocations do change the crystal stacking and are partial dislocations. In this thesis a total Burgers vector of  $a\langle 110 \rangle$  will be referred to as a superdislocation, usually consisting of a pair of  $a/2\langle 110 \rangle$  dislocations which will simply be referred to as  $a/2\langle 110 \rangle$  dislocations, while  $a/3\langle 211 \rangle$  and  $a/6\langle 211 \rangle$  will be referred to as partial dislocations.

#### 4.3.2 Antiphase boundary dislocations

Koehler and Seitz (1947) were the first to suggest that the shear deformation of ordered material may take place by a pair of perfect dislocations from disordered material. Bakish and Robertson (1956) suggested that for (111) deformation an  $a[\bar{1}10]$  superdislocation would split to form two equivalent  $a/2[\bar{1}10]$  dislocations. The first dislocation through the material destroys the order to create an APB and the second identical dislocation travelling in the same direction on the same crystallographic plane restores it (fig. 4.5a). The region between the two dislocations contains APB and its width will be controlled by a balance between the APB energy pulling the dislocations together and the repulsion between the dislocations pushing them apart. By measuring the dislocation spacing it is possible to compute the APB energy (6.2.1).

Pairs of dislocations forming  $\{111\}$  superdislocations were first

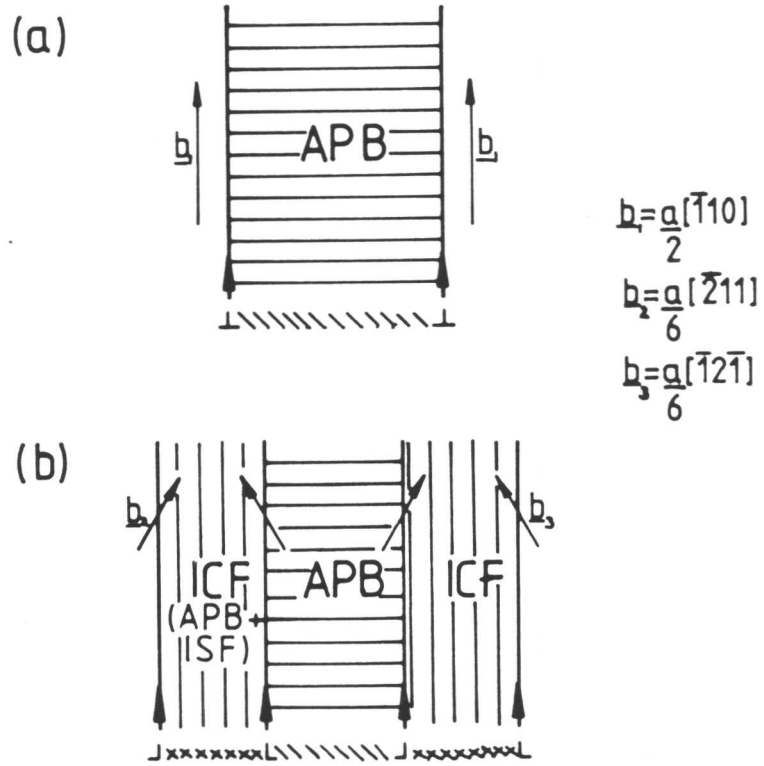


Fig. 4.5(a) and (b). Illustration of a superdislocation split into two  $\frac{a}{2} [\bar{1}10]$  dislocations bounding an APB (a). Each of the  $\frac{a}{2} [\bar{1}10]$  dislocations can dissociate into two  $\frac{a}{6} \langle 211 \rangle$  Shockley partials bounding CF on (111) (b).

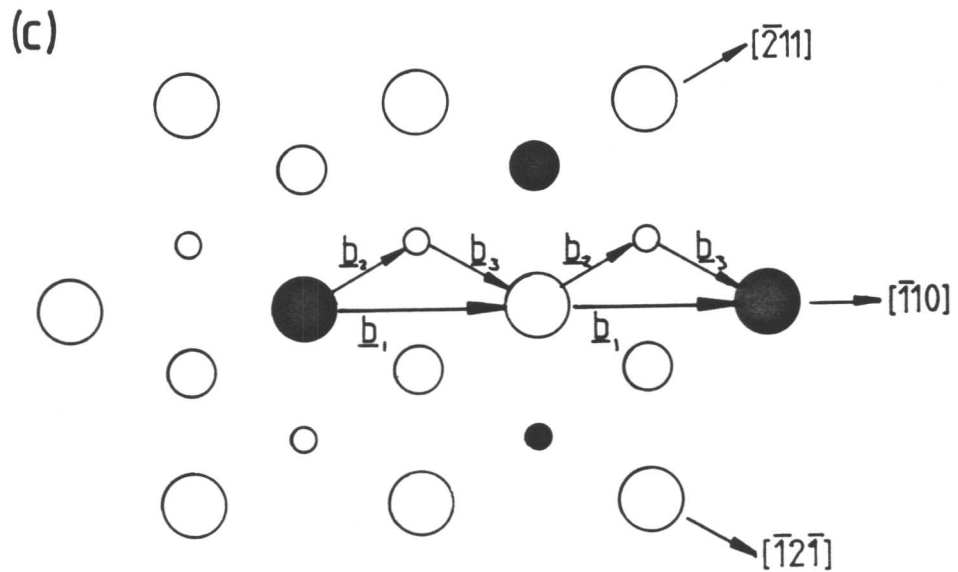


Fig. 4.5(c). Plan view of (111) showing a typical superdislocation displacement by two  $\frac{a}{2} [\bar{1}10]$  dislocations ( $b_1$ ) and the equivalent dissociated dislocations ( $b_2$  and  $b_3$ ).

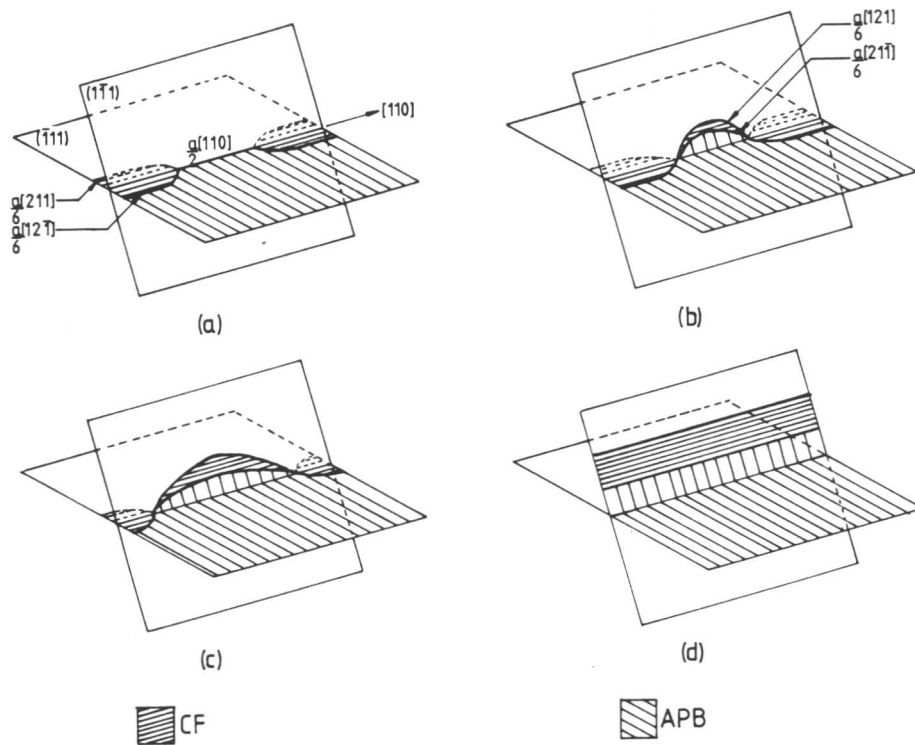


Fig. 4.6. Stages of cross-slip from  $(\bar{1}\bar{1}1)$  to  $(1\bar{1}\bar{1})$  for a dissociated  $a/2[110]$  dislocation bounding an APB showing constriction of the dislocation on  $(\bar{1}\bar{1}1)$  (a), cross-slip and dissociation on  $(1\bar{1}\bar{1})$  (b), and glide on  $(1\bar{1}\bar{1})$  (c). As glide continues the APB will be dragged onto  $(1\bar{1}\bar{1})$  (d).

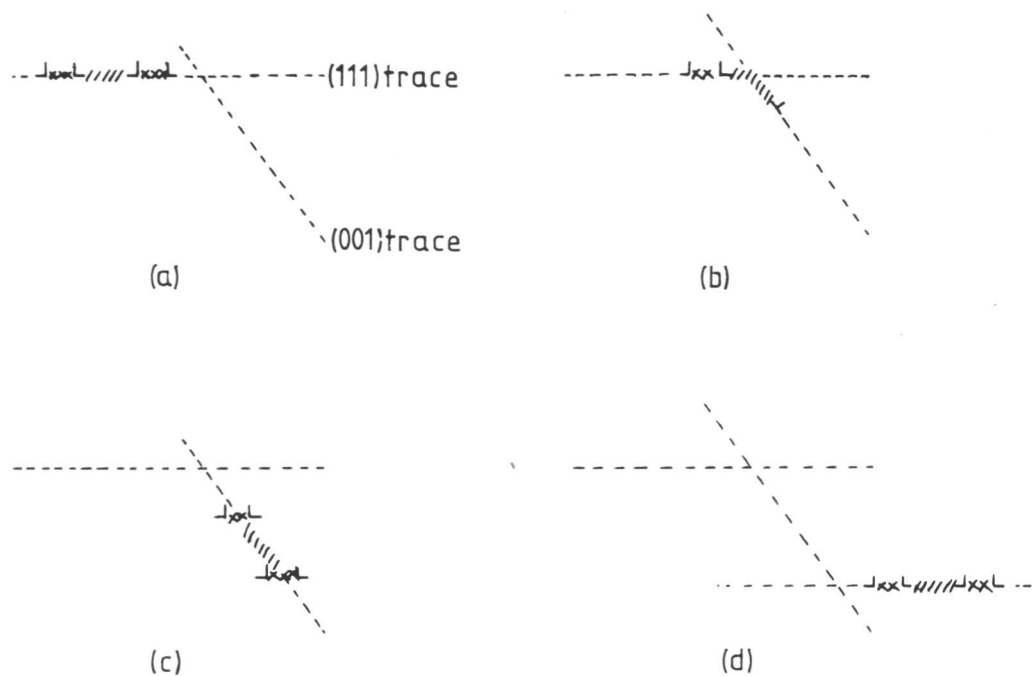


Fig. 4.7. Stages of cross-slip from  $\{111\}$  to  $\{001\}$  to form a Kear-Wilsdorf lock showing a superdislocation gliding on  $(111)$  (a), the leading dislocation is constricted on  $(111)$  and cross-slips onto  $(001)$  (b). Dissociation of the dislocations occurs on  $(111)$ , thereby locking the superdislocation (c). In certain cases cross-slip back onto  $(111)$  may occur (d).

observed in the TEM by Marcinkowski, Brown and Fisher (1961). They suggested that if the CF energy was small the  $a/2\langle 110 \rangle$  dislocations may each dissociate into two  $a/6\langle 211 \rangle$  partial dislocations forming a CF on either side of the APB (fig. 4.5b). Figure 4.5(c) shows the displacement in terms of Burgers vectors on a (111) section. The dissociation hinders cross-slip between {111} planes and from high APB energy {111} planes, where the superdislocations are glissile, to the low APB energy {001} planes, where the superdislocations are less mobile. This is because the  $a/6\langle 211 \rangle$  partials are unique to one plane and must be constricted to  $a/2\langle 110 \rangle$  before cross-slip can occur - as shown for {111} cross-slip in figure 4.6 and for {111} to {001} cross-slip in figure 4.7. Once on {001} the superdislocation is relatively immobile because the non-close-packed plane will have a high Peierls stress and because any dissociation of the dislocation will occur on {111} (fig. 4.7c). If enough energy and stress are available to constrict the dislocation, glide on {001} may occur (Yamaguchi et al., 1982, and Paidar, Pope and Vitek, 1984). Otherwise the dislocations can only move by climb, or cross-slip back onto {111} (figure 4.7d).

At high temperatures the probability of cross-slip onto {001} is increased. The resulting difficulty of motion once cross-slip has taken place forms the basis of the Kear-Wilks (1962) strengthening mechanism. Slip by  $a/2\langle 110 \rangle$  dislocation pairs on {001} has been seen to occur at high temperatures when the dislocations are constricted - see, for instance, Copley and Kear (1967), Takeuchi and Kuramoto (1973), and Staton-Bevan and Rawlings (1975a).

However complex the dislocation dissociation bounding an APB, the total Burgers vector between the APB and perfect crystal will always be  $a/2\langle 110 \rangle$ . Figure 4.5(c) shows the displacements necessary to form an APB on (111).

### 4.3.3 Superlattice stacking fault dislocations

In addition to splitting into two  $a/2\langle 110 \rangle$  dislocations an  $a\langle 110 \rangle$  superdislocation can be split into two  $a/3\langle 211 \rangle$  partial dislocations (fig. 4.8a). The fault shown has intrinsic character. The leading  $a/3\langle 211 \rangle \{111\}$  partial dislocation gliding through the  $\gamma'$  will create an SSF. The trailing  $a/3\langle 211 \rangle$  will destroy the SSF and restore perfect order. As with the APB, measurement of the partial dislocation spacing should allow calculation of the SSF energy. However, all the reported observations of SSF ribbons (Kear, 1974; Howe et al., 1974; and Suzuki et al., 1979) have either shown faults which passed through more than one  $\gamma'$  particle or were metastable due to interaction with the foil surface. Spacing measurements made from SSFs in these conditions cannot be used to calculate fault energies.

Under certain conditions, it has been shown by Kear et al. (1968) and by Kear et al. (1970) that the  $a/3\langle 211 \rangle$  partials can dissociate into six  $a/6\langle 211 \rangle$  partials.

$$a[\bar{1}10] = a/3[\bar{1}2\bar{1}] + a/3[\bar{2}11] \quad \text{eqn. 4.1a}$$

$$a[\bar{1}10] = a/6[11\bar{2}] + a/6[\bar{1}2\bar{1}] + a/6[\bar{2}11] + a/6[\bar{1}2\bar{1}] + a/6[\bar{2}11] + a/6[\bar{1}\bar{1}2] \quad \text{eqn. 4.1b}$$

The dissociation is shown for a SISF in figures 4.8(b). It can be seen that the first  $a/6\langle 211 \rangle$  partial of the leading dislocation creates an extrinsic CF, the second creates an APB and the third creates the SISF. The trailing dislocations reverse the process. It is expected that the widths of the defects are an inverse function of their energies. In most practical situations when the APB and CF energies are high relative to the SSF energy, the bounding dislocation will exhibit the TEM contrast expected from an  $a/3\langle 211 \rangle$  partial dislocation because the separation of the  $a/6\langle 211 \rangle$  partials will be of the same order as the dislocation image width.

However complex the dislocation structure, the total Burgers

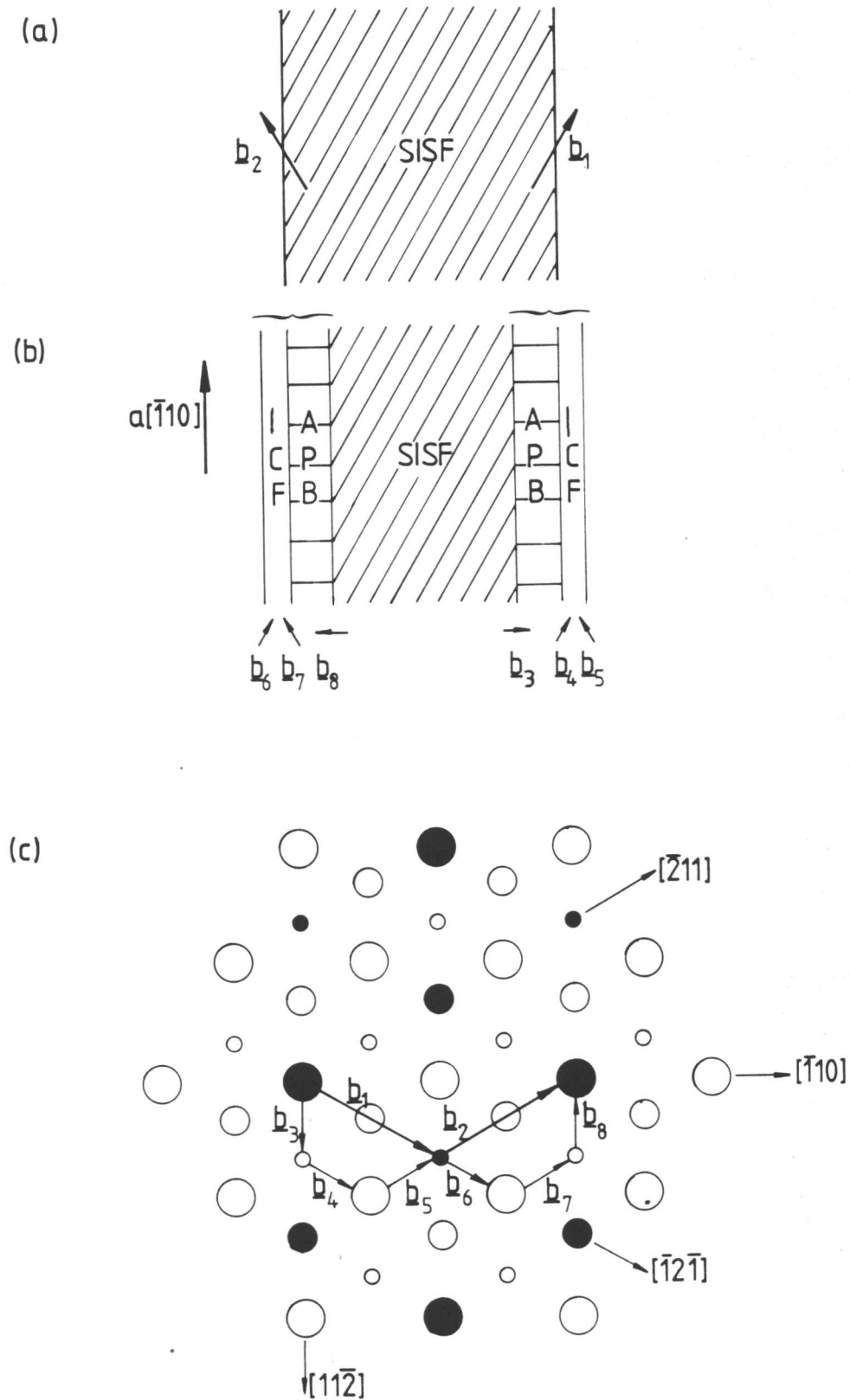


Fig. 4.8. Dissociation of an  $a[\bar{1}10]$  superdislocation on (111) into  $a/3\langle 211 \rangle$  partial dislocations ( $b_1$  and  $b_2$ ) bounding an SISF (a). The  $a/3\langle 211 \rangle$  partial dislocations may each dissociate into three  $a/6\langle 211 \rangle$  Shockley partial dislocations ( $b_3$  to  $b_8$ ) producing the faults shown (b). A plan view on (111) showing the superdislocation displacement by two  $a/3\langle 211 \rangle$  partial dislocations ( $b_1$  and  $b_2$ ) producing an SISF and the equivalent  $a/6\langle 211 \rangle$  partial dislocations ( $b_3$  to  $b_8$ ) is also shown (c). The symbols have the same meanings as figure 4.2. The Burgers vectors are  $b_1 = a/3[\bar{1}2\bar{1}]$ ,  $b_2 = a/3[\bar{2}11]$ ,  $b_3 = a/6[11\bar{2}]$ ,  $b_4 = a/6[\bar{1}2\bar{1}]$ ,  $b_5 = a/6[\bar{2}11]$ ,  $b_6 = a/6[\bar{1}2\bar{1}]$ ,  $b_7 = a/6[\bar{2}11]$  and  $b_8 = a/6[11\bar{2}]$ .

vector between the APB and the perfect crystal will be  $a/3\langle 211 \rangle$ , the Burgers vector between APB and SSF will always be  $a/6\langle 211 \rangle$ , and the Burgers vector between CF and SSF can be  $a/2\langle 110 \rangle$  or  $a/6\langle 211 \rangle$ .

The dislocation configuration required to create an SESF has been constructed in the same way as the SISF and is shown in figure 4.9. In this configuration, if an SESF is to form, the cores of the bounding dislocations must stretch over more than one atomic plane if the lattice displacement is to be accommodated.

#### 4.3.4 Complex fault dislocations

It is thought that because of the high energy of the CF they do not occur unless associated with APBs or SSFs (4.3.2 and 4.3.3). No observations of independent CFs have been reported. When observed in association with other defects, the Burgers vector between the CF and perfect crystal will be  $a/6\langle 211 \rangle$ . A Burgers vector of  $a/2\langle 110 \rangle$  has also been observed between two CFs (see 4.5.3).

### 4.4 Dislocation Structures in L1<sub>2</sub> Prior to Annealing

#### 4.4.1 Dislocation structure in undeformed crystals

After homogenisation and growth, very few dislocations were observed in the  $\gamma'$  when foils were examined in the TEM. A typical microstructure is shown in figure 4.10. In many areas no dislocations were observed under any imaging condition.

The dislocations which were present tended to form boundaries of the type shown in figure 4.11. These boundaries were very uncommon. Because the microstructure contained very few dislocations, there are correspondingly few nucleation sites for carbide precipitation. It was found that strings of small FCC MC carbides form along these dislocation tangles with a cube/cube orientation relationship with the matrix (figure 4.12); the carbide lattice parameter is approximately three times greater

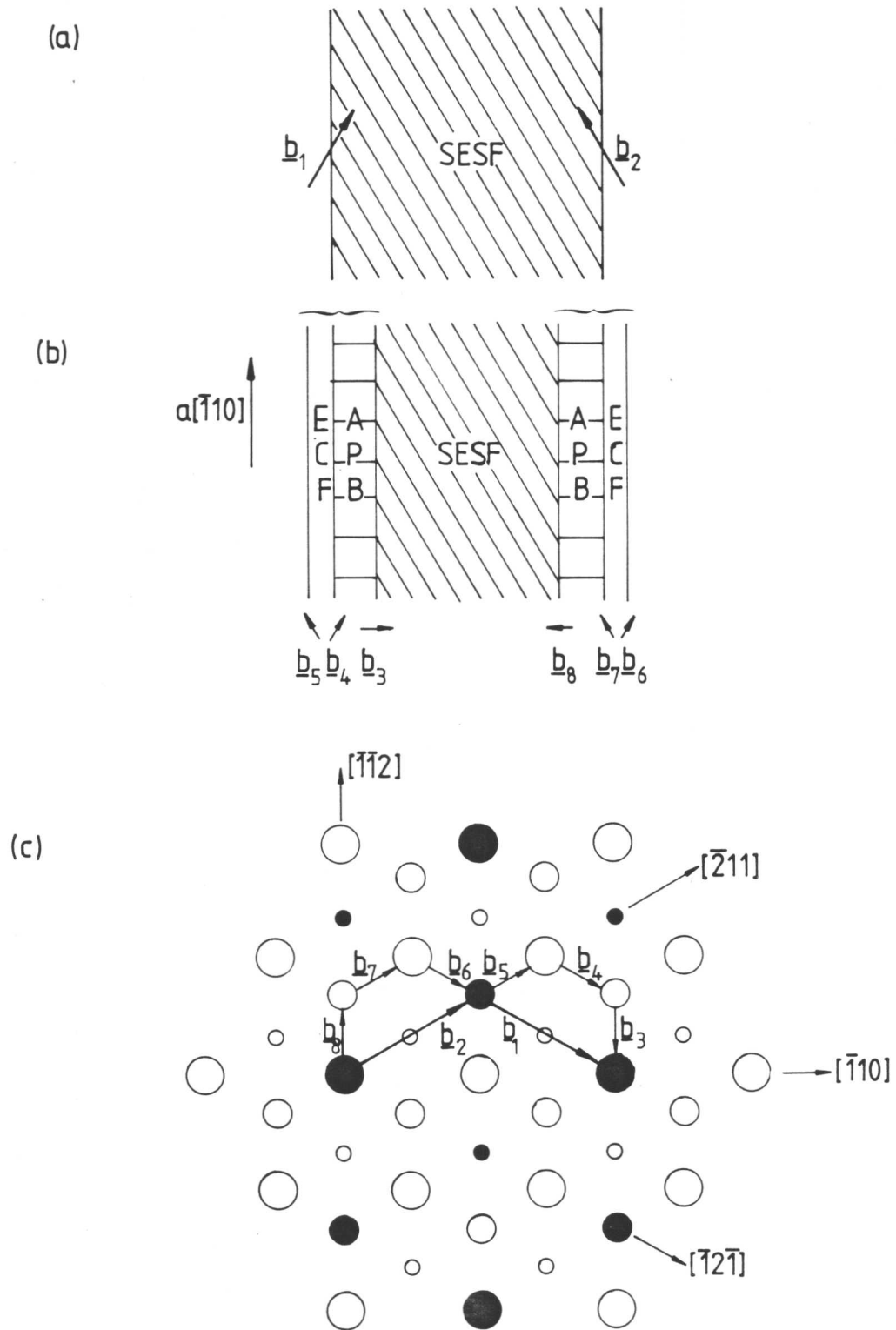


Fig. 4.9. Dissociation of an  $a/3\langle 211 \rangle$  superdislocation on (111) into  $a/3\langle 211 \rangle$  partial dislocations ( $\underline{b}_1$  and  $\underline{b}_2$ ) bounding an SESF (a). The  $a/3\langle 211 \rangle$  partial dislocations may each dissociate into three  $a/3\langle 211 \rangle$  Shockley partial dislocations ( $\underline{b}_3$  to  $\underline{b}_8$ ) producing the faults shown in (b). A plan view on (111) showing the superdislocation displacement by two  $a/3\langle 211 \rangle$  partial dislocations ( $\underline{b}_1$  and  $\underline{b}_2$ ) producing an SESF and the equivalent  $a/6\langle 211 \rangle$  partial dislocations ( $\underline{b}_3$  to  $\underline{b}_8$ ) is also shown (c). The symbols have the same meanings as figure 4.2 and the Burgers vectors are the same as figure 4.8.

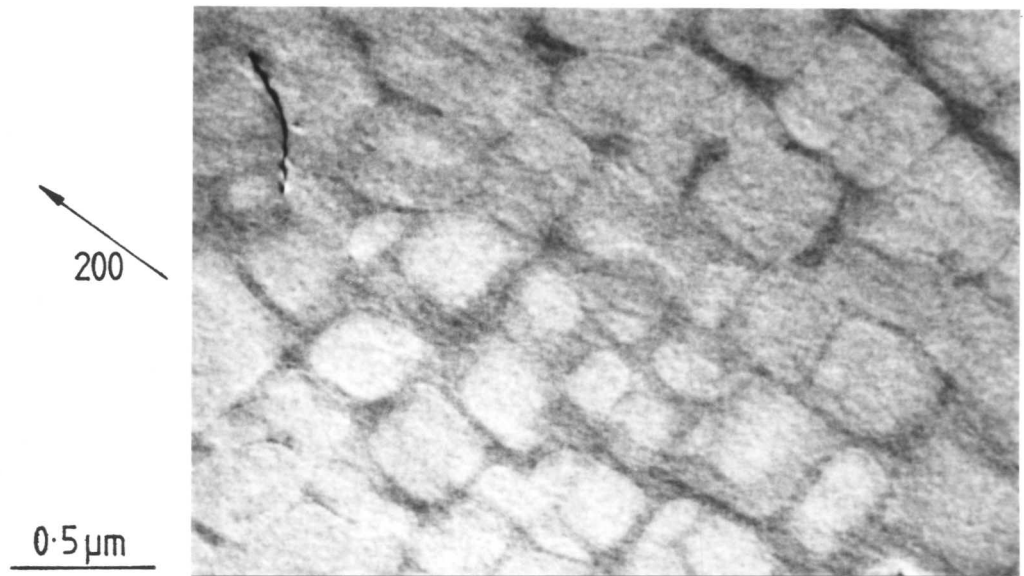


Fig. 4.10. Bright field TEM micrograph showing  $\gamma/\gamma'$  microstructure after homogenisation for 36 hrs at 1570K followed by 16 hrs at 1390K (foil normal:  $\sim[001]$ ).

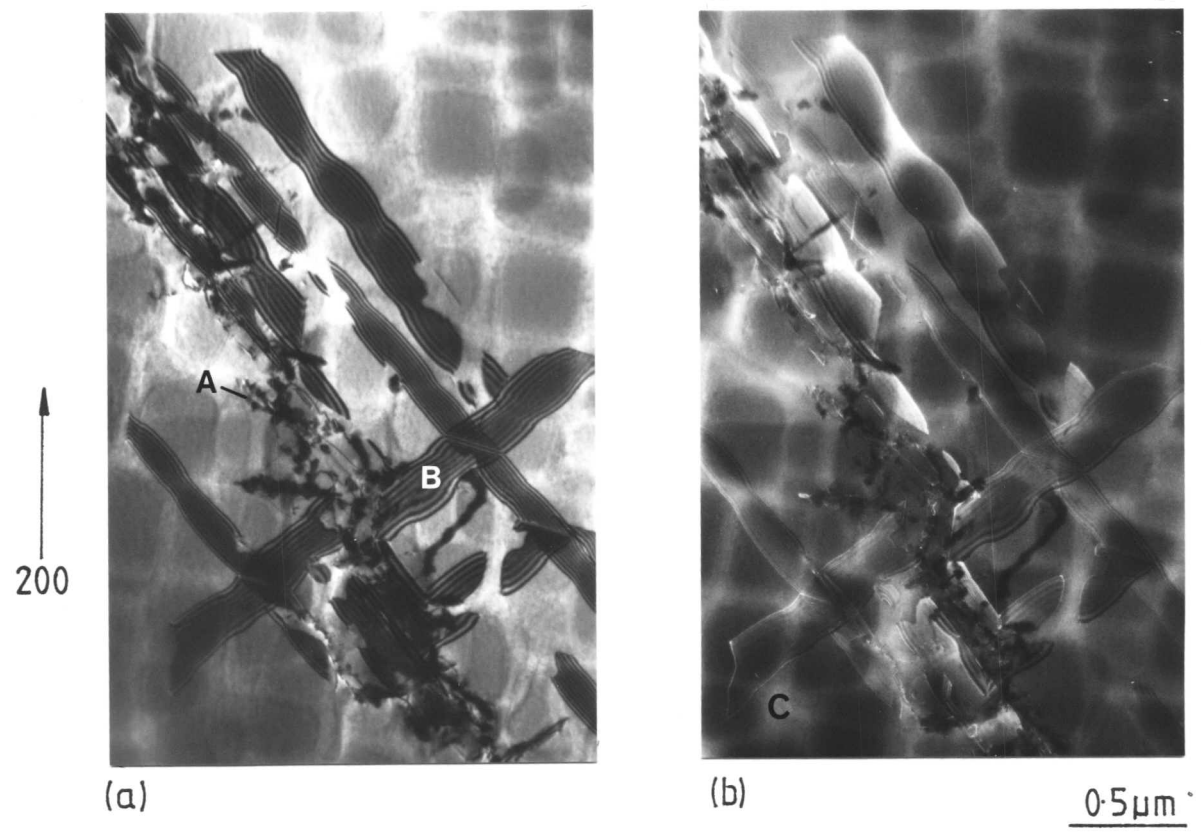


Fig. 4.11. Bright field (a) and weak beam (b) TEM micrograph of dislocation tangles showing globular MC precipitation (A) and planar  $\text{Ni}_3\text{Ti}$  (B) bounded by an  $a/3\langle 111 \rangle$  dislocation (C). (foil normal:  $\sim[001]$ ).

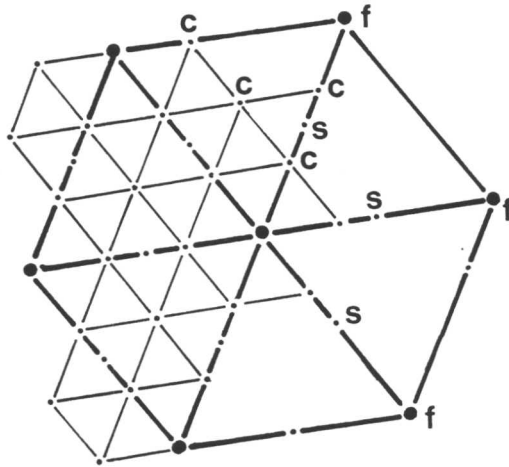
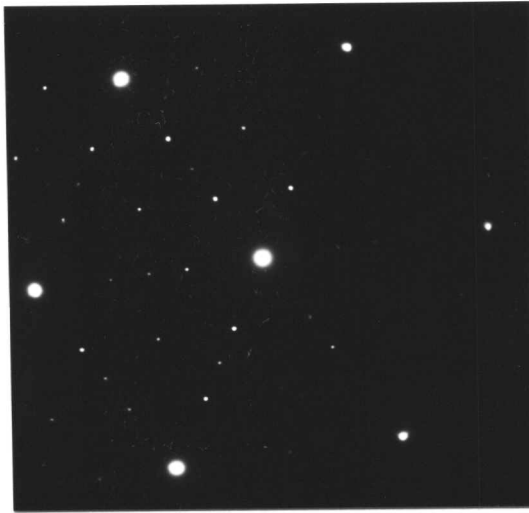


Fig. 4.12. Diffraction pattern taken from carbides, on a boundary similar to that shown in figure 4.11, showing fundamental (f), superlattice (s) and carbide (c) reciprocal lattice points. (foil normal:  $\sim[111]$ ).

than the  $\gamma$  matrix. MC carbides are rich in Ta, Ti and W (see 2.6.2).

The large planar defects visible in figure 4.11 were observed to be linked to boundaries containing carbides. These defects, which exhibit stacking fault contrast, were bounded by  $a/3\langle 111 \rangle$  Frank partial dislocations (Rae, 1984) demonstrating that they could not have been formed by shear. The defects could either be stacking faults, formed by agglomeration of point defects or interstitials, or thin planar precipitates. They were observed to pass through  $\gamma$  and  $\gamma'$  without any change at the interphase boundaries. It is the opinion of Rae and the author that these large planar defects are planar precipitates of  $\text{Ni}_3\text{Ti}$ , similar to those observed in Udimet 700 by Kear et al. (1970), which are growing out into the bulk material from the precipitate loaded boundaries. Further work to confirm this opinion is being undertaken by Rae.

#### 4.4.2 Dislocation structure in deformed crystals

Room temperature deformation considerably increased the dislocation density (fig. 4.13). The majority of the dislocations generated were in the  $\gamma$  matrix between the  $\gamma'$  particles. This is at least in part due to the difficulty encountered by  $a/2\langle 110 \rangle$  dislocations trying to enter the  $\gamma'$  at low temperatures. To enter the  $\gamma'$  dislocations must 'pair-up' to form superdislocations of two  $a/2\langle 110 \rangle$  dislocations of the same type on the same plane. At 293K it is highly unlikely that sufficient cross-slip can occur in the  $\gamma$  to produce superdislocations. The few superdislocations observed in the  $\gamma'$  must have formed by the 'pairing-up' of like dislocations which were lying adjacent on the same plane.

Cold deformation produced inhomogeneous deformation in the form of slip bands on  $\{111\}$  as shown in figure 4.14. This figure shows that most of the deformation took place by dislocations looping around the  $\gamma'$ . Some superdislocations, however, were forced through the  $\gamma'$ . At the intersection of the slip bands, superdislocations on different planes were

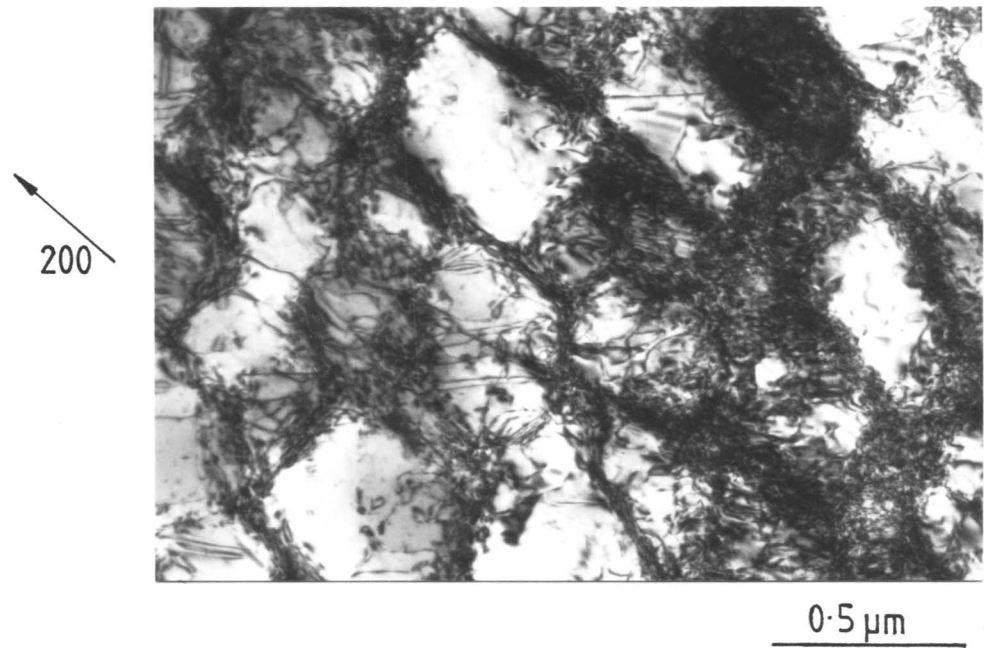


Fig. 4.13. Bright field TEM micrograph showing dislocations generated by cold deformation. Most of the dislocations lie in the  $\gamma$  matrix although some are visible in the  $\gamma'$ . (foil normal:  $\sim[001]$ ).

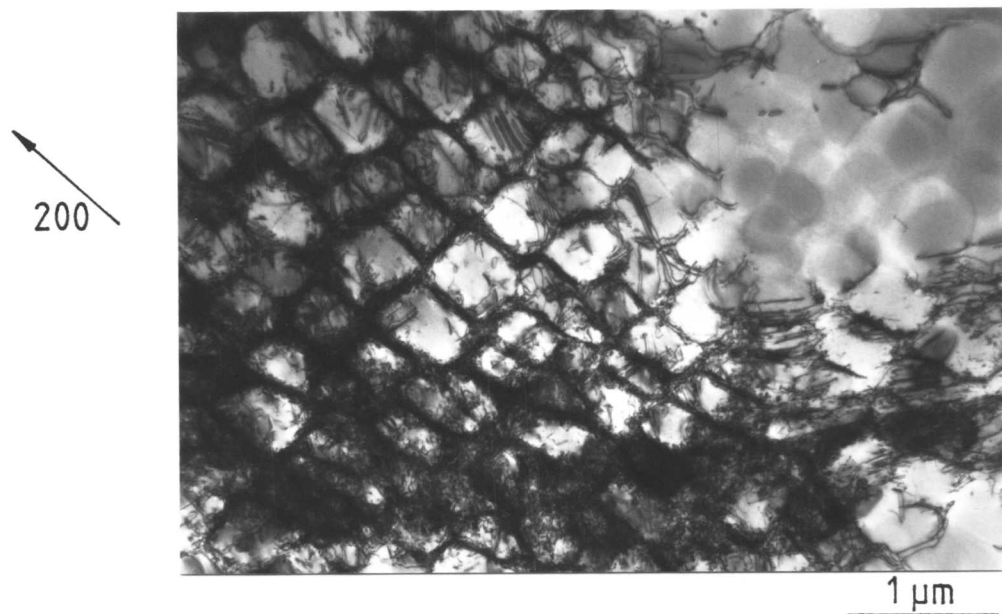


Fig. 4.14. Bright field TEM micrograph showing intersecting slip bands. (foil normal:  $\sim[001]$ ).

seen to interact. In the annealed condition these superdislocations adopted the supernode configurations described later in this chapter.

Little work was carried out to characterise the dislocation interactions in the low temperature deformed structures. But they were carefully examined as it was vital to make certain that the dislocation structures observed in the annealed structures were not residual interactions left from the cold deformed microstructures.

#### 4.5 Hexagonal Dislocation Networks in Deformed and Annealed Crystals

##### 4.5.1 Theoretical arrangement

As discussed more fully in 5.2.1, during annealing  $a/2\langle 110 \rangle$  dislocations in the  $\gamma$  matrix climb to form pairs of  $a/2\langle 110 \rangle$  dislocations on the same plane. These superdislocations glide into the  $\gamma'$  and can interact with other superdislocations. This section describes the formation of the interaction which is most important in the evaluation of APB and SSF energies. As part of the annealing process, the superdislocations gliding through the  $\gamma'$  will aim to adopt the lowest energy configuration possible. In disordered materials the configuration adopted is often a hexagonal network on a  $\{111\}$  plane (Whelan, 1959).

Whelan stated that when two dislocations of different Burgers vector AB and A'B' (figure 4.15a) intersect on the same or different planes, there will be an elastic interaction between the segments of dislocation line at the point of intersection (Read, 1953 and Amelinckx, 1956). The interaction will depend upon the Burgers vectors of the dislocations involved but, in general, if there is an attraction, the dislocations may combine to form a third dislocation A"B" (figure 4.15b). The interaction will <sup>possibly</sup> occur when the angle between the dislocation Burgers vectors is  $120^\circ$  and if the attraction reduces the total strain energy of the system.

In the rest of this chapter Whelan's ideas for interaction between single dislocations in FCC are extended to account for similar interactions

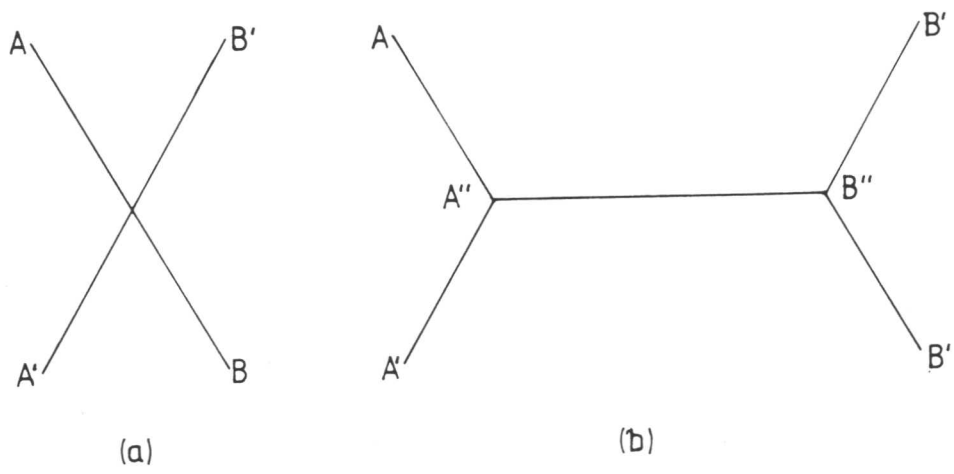


Fig. 4.15. Schematic diagram showing the interaction of two dislocations AB and A'B' to produce a third A''B''.

in  $L1_2$ . For simplicity it will be assumed that the dislocations have pure screw character. In describing the interactions, Thompson's notation (Thompson, 1951 and fig. 4.16) will be used in addition to the normal notation. This will help the reader to appreciate which planes the various dislocations inhabit, particularly when the more complex case is considered.

Two cases are considered. First, when both superdislocations lie in  $(111), \delta$ . The dislocation reaction will be:



Secondly, when  $a[01\bar{1}]$  lies in  $(1\bar{1}\bar{1}), \beta$  and  $a[\bar{1}01]$  lies in  $(\bar{1}\bar{1}\bar{1}), \alpha$ . This reaction produces  $a[\bar{1}\bar{1}0]$  which lies in either  $(111), \delta$  or  $(1\bar{1}\bar{1}), \gamma$

Both interactions will produce the configuration shown in figure 4.17 if it is assumed that each superdislocation is split into two  $a/2\langle 110 \rangle$  dislocations.

#### 4.5.2 Observations of the dislocation interaction

The dislocation interactions at the nodal points are complex and cannot be described adequately without dissociating the  $a/2\langle 110 \rangle$  dislocations into their component  $a/6\langle 211 \rangle$  partials. These reactions are described in 4.5.3 and 4.5.4. However, using the TEM techniques described in this thesis, no dissociation of the  $a/2\langle 110 \rangle$  dislocations was observed in the regions away from the nodal points.

Interactions similar to that shown in figure 4.18 were frequently observed in the  $\gamma'$  of the deformed and annealed foils. Table 4.1 shows some of the  $g \cdot b$  values for the  $a/2\langle 110 \rangle$  dislocations shown in figure 4.18. The dislocations were identified as  $a/2[0\bar{1}1]$  and  $a/2[\bar{1}\bar{1}0]$  which have interacted to produce  $a/2[10\bar{1}]$ , although some residual contrast is visible from  $a/2[\bar{1}\bar{1}0]$  in figure 4.18(b). They have adopted a roughly screw orientation



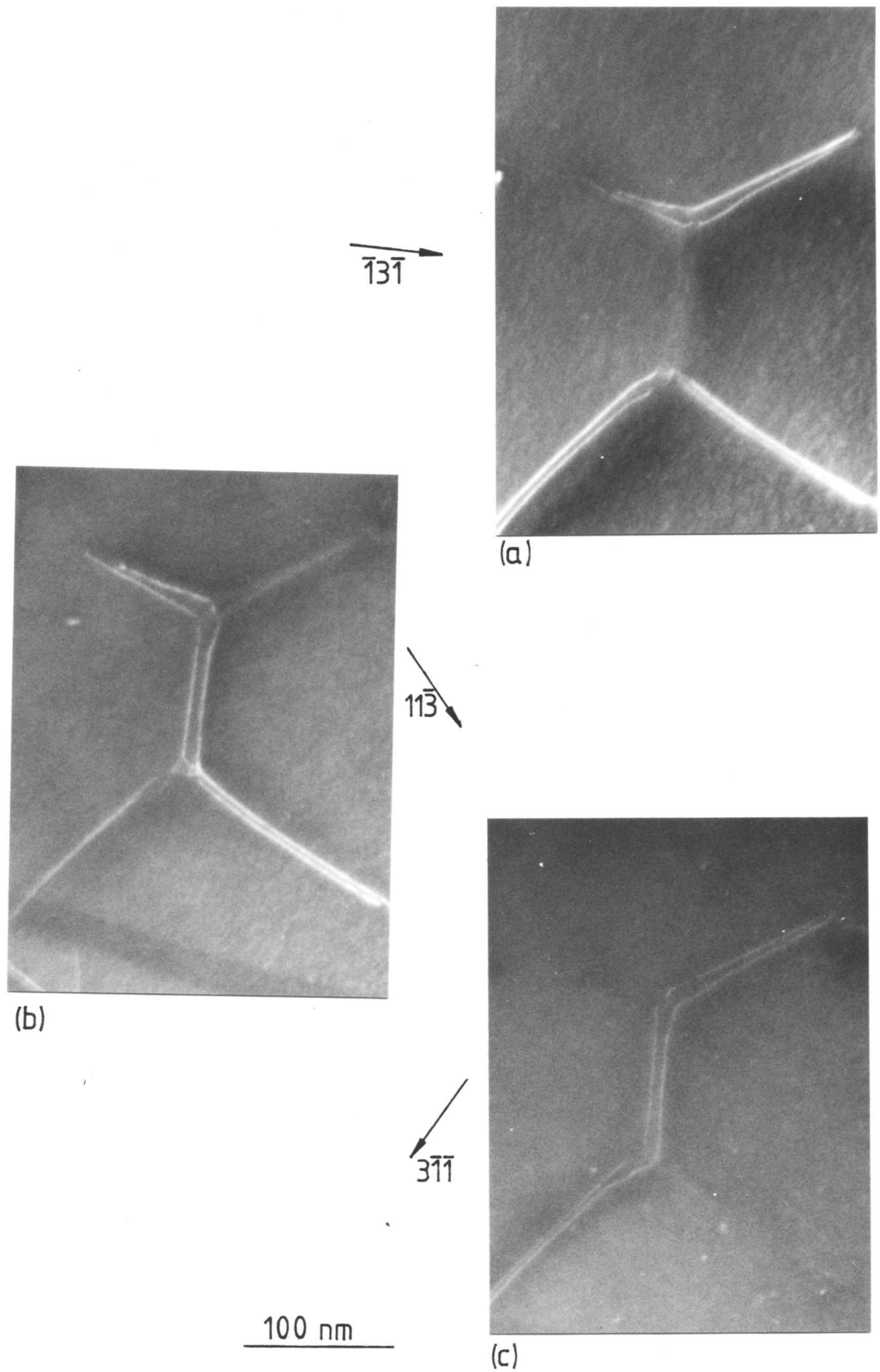
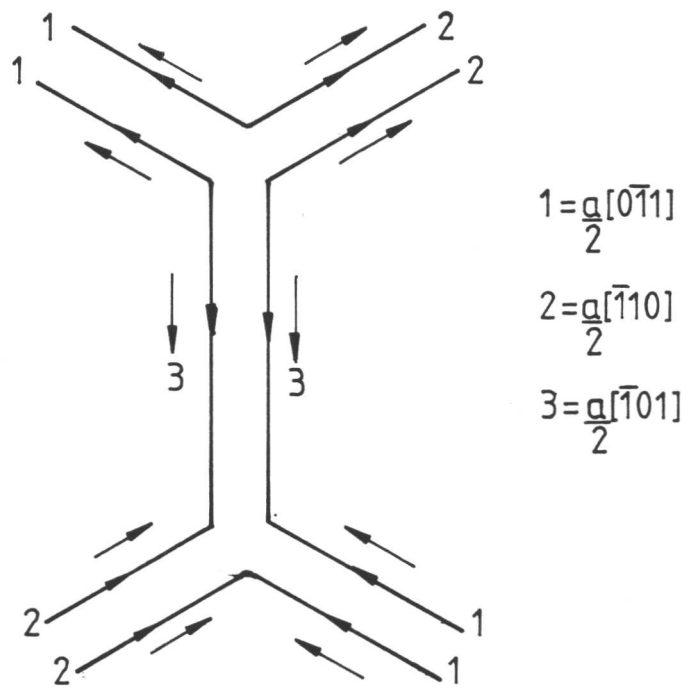


Fig. 4.18. Weak beam dark field TEM micrographs taken in conditions between  $W(\underline{g}, 2\underline{g})$  and  $W(\underline{g}, 4\underline{g})$  showing a typical superdislocation interaction in the  $\gamma'$ . The dislocations were identified using table 4.1 and are shown in (d). Some residual contrast is visible from  $a/2[\bar{1}10]$  in (b). (foil normal:  $\sim[111]$ ).

(Figure continued overleaf)



(d)

Fig. 4.18. For caption see previous page.

Table 4.1.  $\underline{g} \cdot \underline{b}$  values for the  $a/2\langle 110 \rangle$  dislocations shown in figure 4.18

Micrograph	Diffraction vector ( $\underline{g}$ )	Burgers vector ( $\underline{b}$ )		
		$\pm a/2[01\bar{1}]$	$\pm a/2[1\bar{1}0]$	$\pm a/2[10\bar{1}]$
(a)	$\bar{1}3\bar{1}$	$\pm 2$	$\mp 2$	[0]
(b)	$11\bar{3}$	$\pm 2$	[0]	$\pm 2$
(c)	$3\bar{1}\bar{1}$	[0]	$\pm 2$	$\pm 2$

Table 4.2.  $\underline{g} \cdot \underline{b}$  values for the  $a/2\langle 110 \rangle$  dislocations shown in figure 4.22

Micrograph	Diffraction vector ( $\underline{g}$ )	Burgers vector ( $\underline{b}$ )		
		$\pm a/2[10\bar{1}]$	$\pm a/2[1\bar{1}0]$	$\pm a/2[01\bar{1}]$
(a)	$1\bar{1}1$	[0]	$\pm 1$	$\mp 1$
(b)	$11\bar{1}$	$\pm 1$	[0]	$\pm 1$
(c)	$\bar{1}11$	$\mp 1$	$\mp 1$	[0]
(d)	$2\bar{2}0$	$\pm 1$	$\pm 2$	$\mp 1$
(e)	$20\bar{2}$	$\pm 2$	$\pm 1$	$\pm 1$

[ ] - invisible

but close to the nodal regions the superdislocations have been distorted and no longer lie in their original glide planes. This non-planarity is related to the dislocation structure at the nodal points (see 4.5.3).

Planar hexagonal networks were also observed, such as the one shown in figure 4.25. This network lies on (111) in a [001] foil. The network is therefore tilted through the foil. The dislocation structure is discussed in more detail later (4.5.3).

In many cases the networks adopted a hexagonal equilibrium configuration of screw superdislocations at  $120^\circ$ . Many APB energies have been determined by measuring the equilibrium spacing (6.3.3).

#### 4.5.3 Dislocation interactions at the nodal points

In order to interpret the nodal reactions effectively it has proved necessary to split each of the  $a/2\langle 110 \rangle$  dislocations forming the superdislocation into two component  $a/6\langle 211 \rangle$  partial dislocations. As in 4.5.2, the  $a/2\langle 110 \rangle$  dislocations considered are all pure screw and the Burgers vector of these dislocations will always be taken in the same direction as the dislocation line sense.

First, the interaction between an  $a/2[01\bar{1}]$  pair and an  $a/2[\bar{1}01]$  pair at  $120^\circ$  on (111) will be considered. Each of the  $a/2\langle 110 \rangle$  dislocations will be dissociated as follows:

$$a/2[01\bar{1}] = a/6[11\bar{2}] + a/6[\bar{1}\bar{2}\bar{1}] \quad \text{eqn. 4.3a}$$

$$AC = \delta C + A\delta \quad \text{eqn. 4.3b}$$

and

$$a/2[\bar{1}01] = a/6[\bar{2}11] + a/6[\bar{1}\bar{1}2] \quad \text{eqn. 4.4a}$$

$$CB = \delta B + C\delta \quad \text{eqn. 4.4b}$$

If these dislocations were to interact on (111) the initial configuration would be that shown in 4.19(a). The  $a/6\langle 211 \rangle$  partial dislocations crossing at points A, B, C and D would be the same and these will

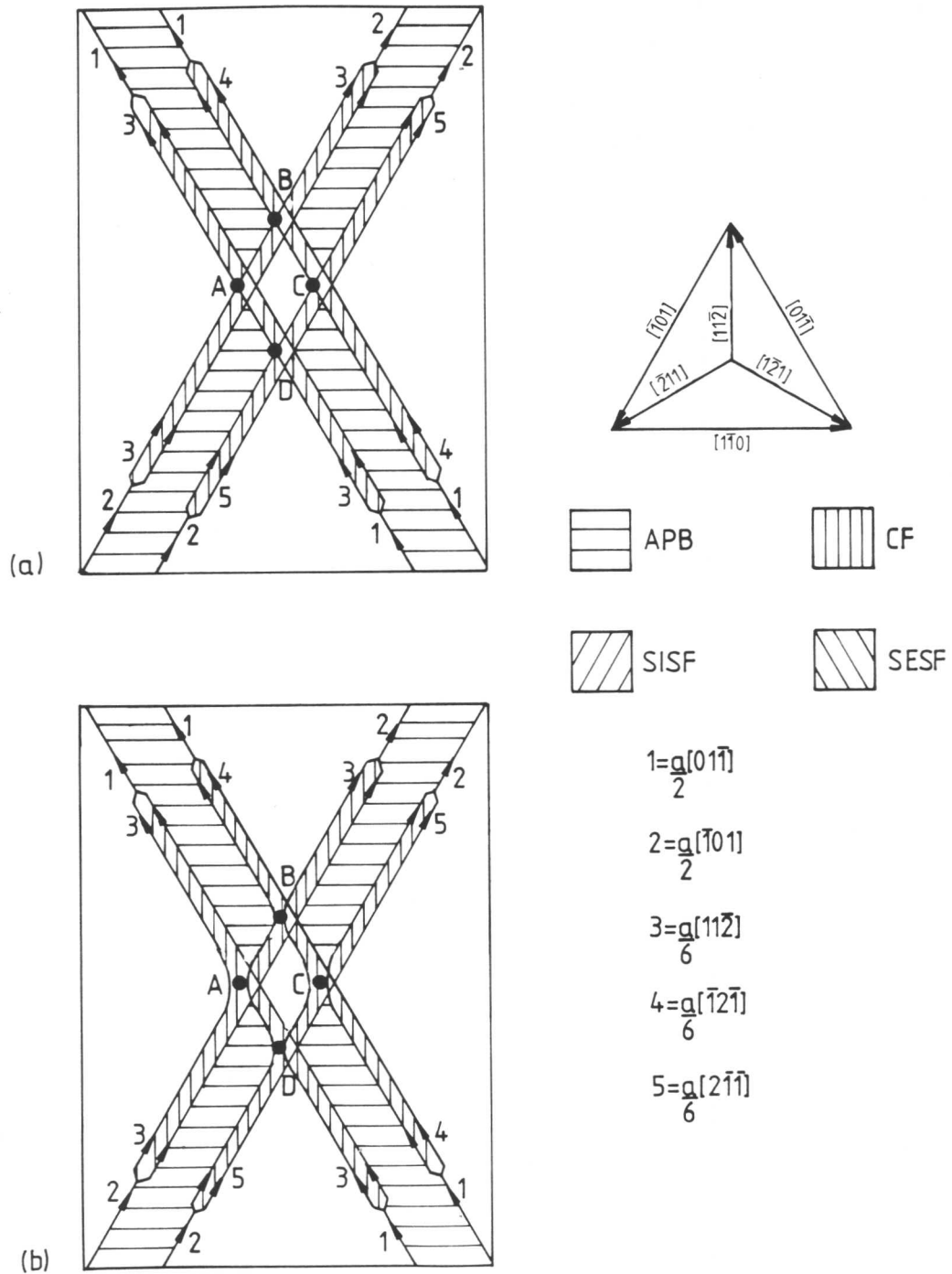


Fig. 4.19. Schematic illustration of the proposed interaction between two superdislocations on (111) showing the initial position (a), the configuration after parting at A, B, C, D (b), the configuration after limited glide (c), and the final configuration (d). See text for details. Each  $a/2 \langle 110 \rangle$  dislocation has been split into two  $a/6 \langle 211 \rangle$  Shockley partial dislocations. The Burgers vectors are shown in the triangle to the right of figure (a).

(Figure continued overleaf)

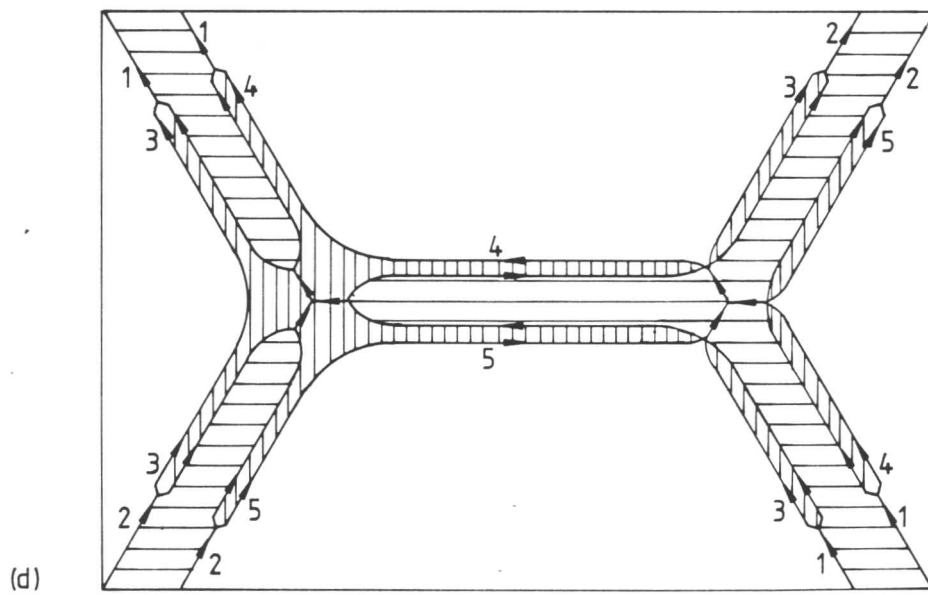
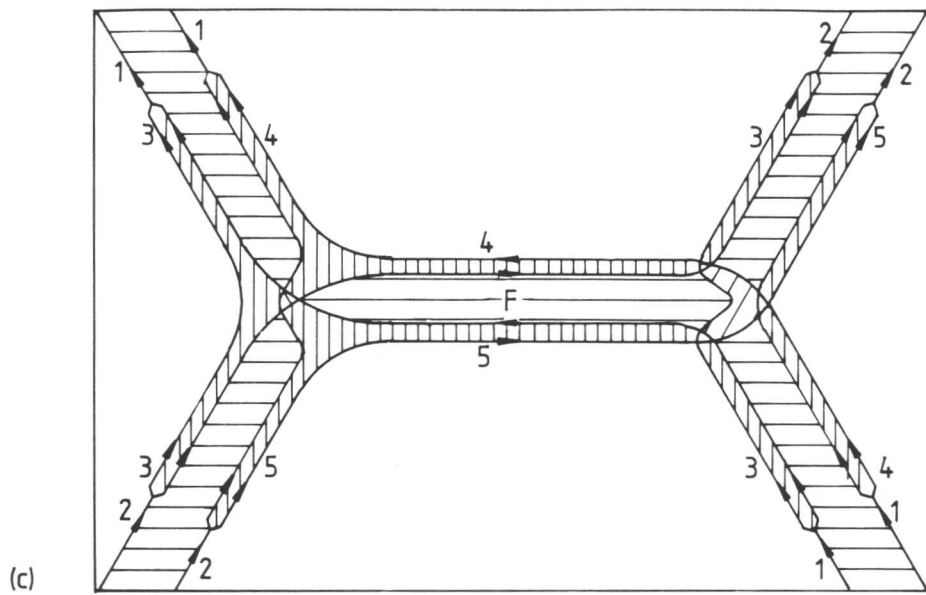


Fig. 4.19. For caption see previous page.

interact (when they are coplanar) to produce the configuration shown in figure 4.19(b). When the two interacting superdislocations glide away, lengths of partial dislocation will be drawn out between them to form two three-fold nodes (fig. 4.19c). If it is assumed that the CF energy is higher than the APB energy, the network will try to lower its energy by expanding the new APB region marked F. Partials 4 and 5 will be strongly attracted to form  $a/2[1\bar{1}0]$ , thus reducing the total CF area. Partials at the nodal points are also likely to be attracted to one another, also to lower their energy by adopting the screw orientation. The dislocations at the nodal points will balance their energies so that when resolved they equal zero. This balance may produce three equal sized metastable regions of CF at some nodes. The predicted equilibrium configuration is shown in figure 4.19(d).

When two superdislocations, on different glide planes, with Burgers vectors which intersect at  $120^\circ$  interact, the dislocation interaction will be considerably more complex. Dislocation cross-slip must occur if a network is to form.  $a/2\langle 110 \rangle$  dislocations can cross-slip between  $\{111\}$  planes but if there is any dissociation into  $a/6\langle 211 \rangle$  partial dislocations, this must be constricted before cross-slip can occur as  $a/6\langle 211 \rangle$  dislocations only have one glide plane (fig. 4.7).

Consider the same two superdislocations as previously but in this case the  $a/2[01\bar{1}]$  pair lies in  $(\bar{1}11), \beta$  and the  $a/2[\bar{1}01]$  pair lies in  $(1\bar{1}1), \alpha$ ; the  $a/2[1\bar{1}0]$  dislocation pair produced can lie on  $(111), \delta$  or  $(\bar{1}\bar{1}1), \gamma$ . It will be assumed to lie on  $(111), \delta$ .

The dislocation dissociations are:

$$a/2[01\bar{1}] = a/6[12\bar{1}] + a/6[\bar{1}\bar{1}\bar{2}] \quad \text{eqn. 4.5a}$$

$$AC = \beta C + A\beta \quad \text{eqn. 4.5b}$$

$$a/2[\bar{1}01] = a/6[\bar{1}\bar{1}2] + a/6[\bar{2}\bar{1}1] \quad \text{eqn. 4.6a}$$

$$CB = \alpha B + C\alpha \quad \text{eqn. 4.6b}$$

and

$$a/2[1\bar{1}0] = a/6[1\bar{2}1] + a/6[2\bar{1}\bar{1}] \quad \text{eqn. 4.7a}$$

$$\text{BA} \qquad \qquad \delta\text{A} \qquad \qquad \text{B}\delta \qquad \qquad \text{eqn. 4.7b}$$

The expected interaction is shown in figure 4.20. It will be assumed that the interaction and the dislocations produced by the interaction will lie on  $(111), \delta$ . However, it is possible that the nodal interaction may lie on a different plane from the new APB which will be produced. No energy calculations have been performed to evaluate which plane would be energetically most favourable. It is thought that this will be related to the stress direction which was not controlled carefully enough for an accurate determination to be made.

Figure 4.20(a) shows the first stage of the interaction. The leading AC and CB dislocations intersect. The two partials  $\beta\text{C}$  and  $\text{C}\alpha$  combine and cross-slip onto  $\delta$  forming a very short  $\beta\alpha$  stair-rod dislocation at the point of intersection while  $\text{A}\beta$  and  $\alpha\text{B}$  combine and cross-slip onto  $\delta$  to form BA. The applied stress and the line tensions of  $\beta\text{C}/\text{C}\alpha$  and  $\text{A}\beta/\alpha\text{B}$  will pull BA out along  $\delta$  until the trailing CA and CB dislocations interact. Further cross-slip will produce the dislocation configuration shown in figure 4.20(b). The reduction of total strain energy will force this configuration to extend on  $\delta$ . A plan view of the equilibrium structure, which is similar to figure 4.19(d), is shown in figure 4.20(d). In this configuration the interacting superdislocations are twisted away from their original glide planes to meet  $(111), \delta$ . If enough energy is available the APBs and their bounding dislocations will cross-slip to form a planar network on  $(111), \delta$ . The equilibrium structure for a fully cross-slipped network will be the same as that shown in figure 4.21.

Two types of nodes are evident at the junctions (figs. 4.19, 4.20 and 4.21). In this configuration both are constricted. In certain conditions they may expand to form the extended nodes discussed in 4.5.5.

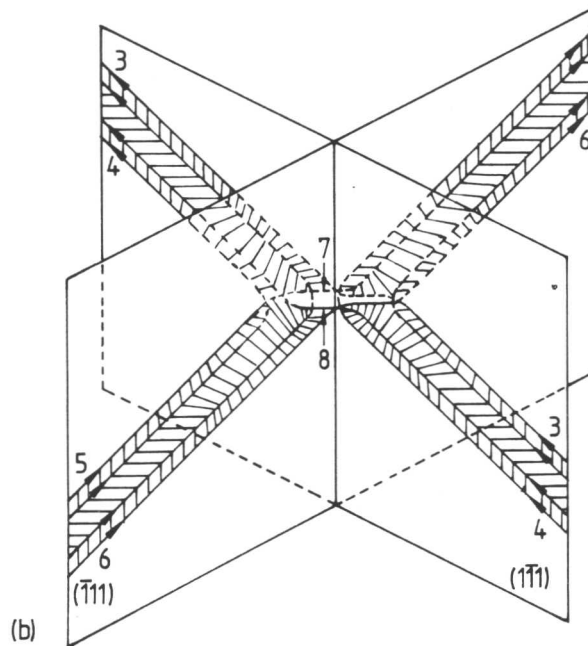
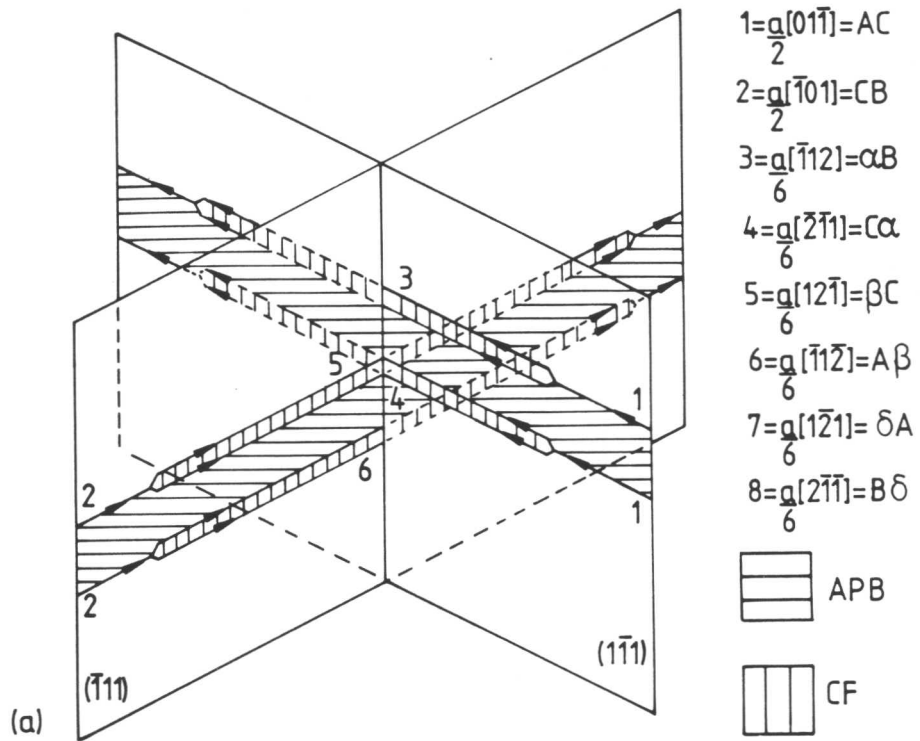


Fig. 4.20. Schematic illustration of the proposed interaction between two superdislocations on different  $\{111\}$  planes showing the initial position (a), a projection of the interaction at an intermediate point showing that the superdislocations are twisted from their glide planes (b), a plan of stage (b), (c), and a plan of the final configuration (d). See text for details.

(Figure continued overleaf)

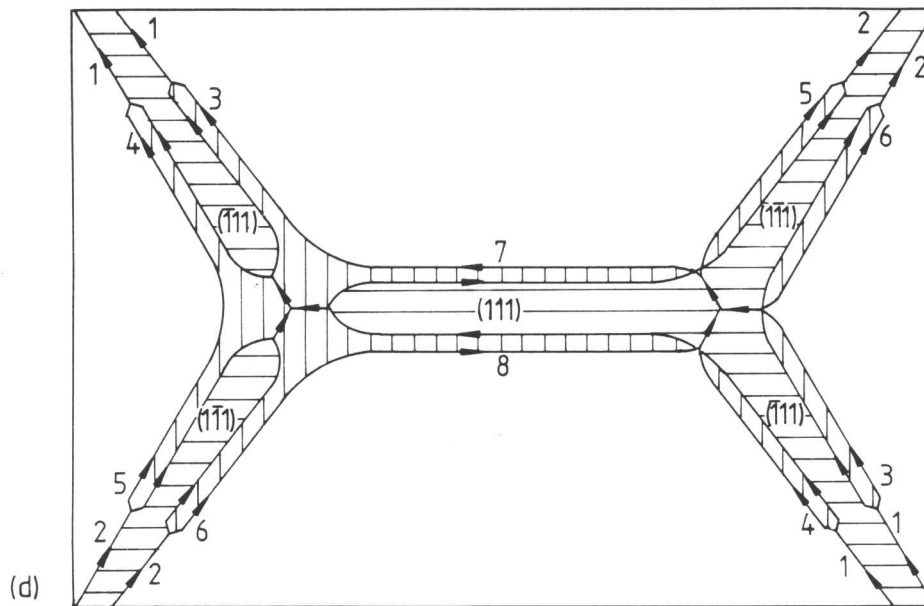
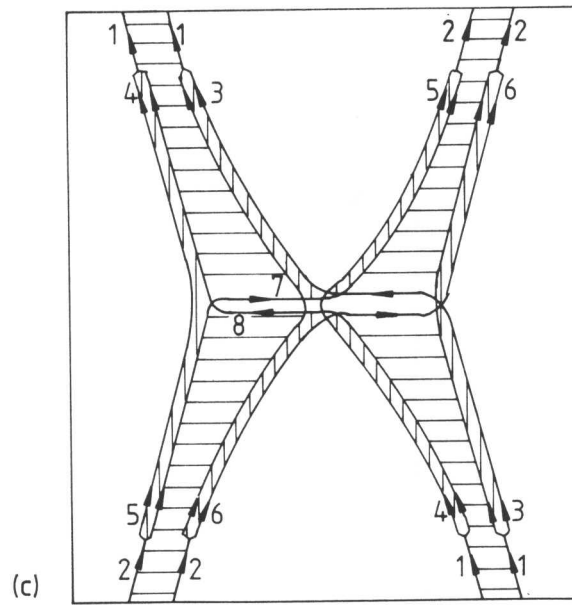


Fig. 4.20. For caption see previous page.

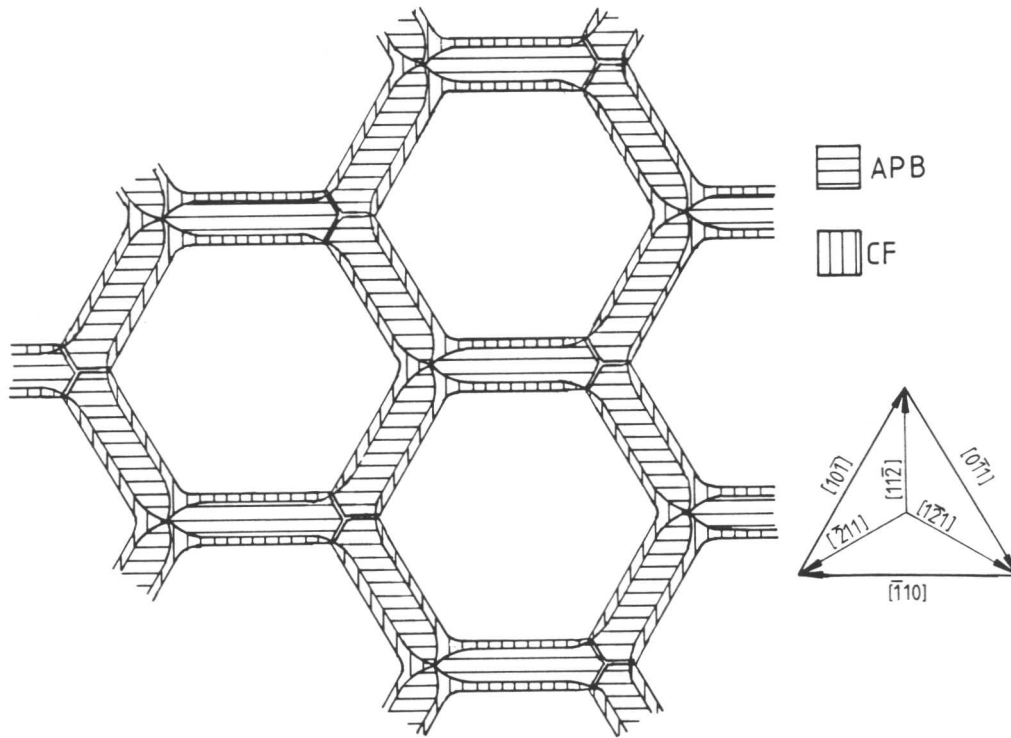


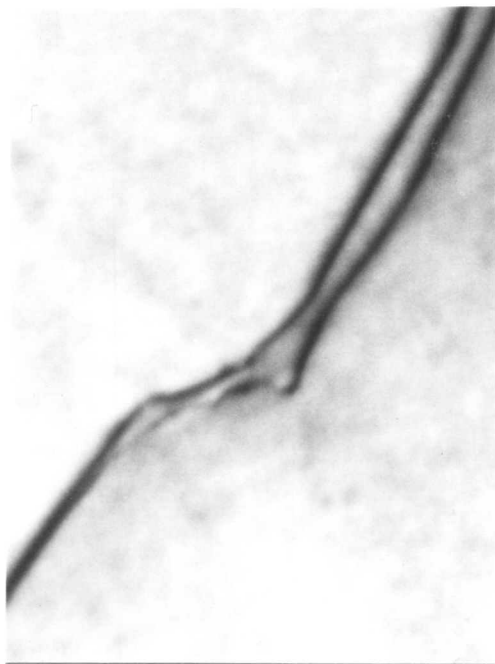
Fig. 4.21. The equilibrium configuration of a superdislocation network in a  $L1_2$  structure (predicted by Amelinckx, 1979).

If these interactions to form networks are to occur in practice, a considerable amount of energy will be required. It is likely that the necessary interactions will only occur by the relief of strain energy held in highly deformed structures when they are annealed at a temperature which provides sufficient energy to promote cross-slip by the constriction of dissociated dislocations. This will initially produce a network which resides on two, three, or even four  $\{111\}$  planes. Figure 4.20(d) shows  $a/2[01\bar{1}](\bar{1}11)$  and  $a/2[\bar{1}01](1\bar{1}1)$  interacting to produce  $a/2[1\bar{1}0]$  on  $(111)$ . The nodal reaction has been assumed to be on  $(111)$ .

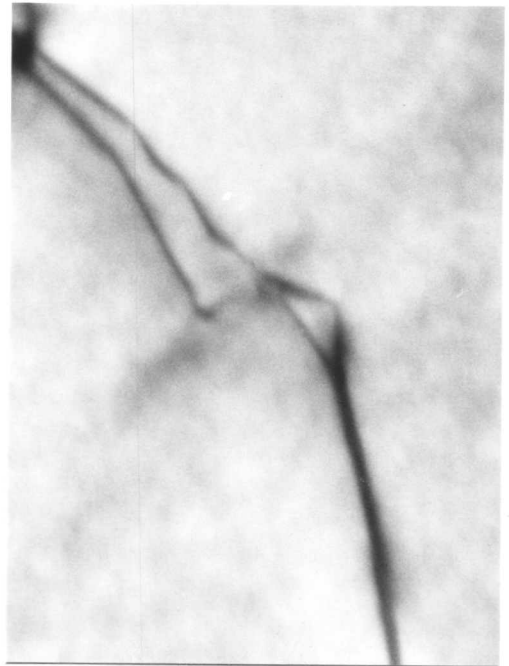
#### 4.5.4 Observations of nodal reactions

Many interactions similar to those described above were observed in deformed and annealed microstructures of alloys A, D and G. Figure 4.22 is part of a g·b series of TEM micrographs recorded from an interaction equivalent to that shown in figure 4.20(b). Table 4.2 lists the g·b values for the  $a/2\langle 110 \rangle$  dislocations in this configuration. It was found that figure 4.22 showed an interaction between an  $a[10\bar{1}]$  superdislocation gliding on  $(1\bar{1}1)$  and an  $a[1\bar{1}0]$  superdislocation gliding on  $(11\bar{1})$ . The interaction produced two segments of  $a/2[01\bar{1}]$  which could lie in either  $(111)$  or  $(1\bar{1}1)$  depending upon the glide plane of the partial dislocations forming the  $a/2[01\bar{1}]$  dislocation. The central dislocation configuration was too fine to be resolved using bright field TEM but if each of the constituent  $a/2\langle 110 \rangle$  dislocations is assumed to be dissociated onto  $(111)$  the dislocation would be that shown in figure 4.22(f). No dissociation of any of the  $a/2\langle 110 \rangle$  dislocations was observed. As predicted in 4.4.3, the APBs were twisted from their initial glide planes by the interaction on  $(111)$ .

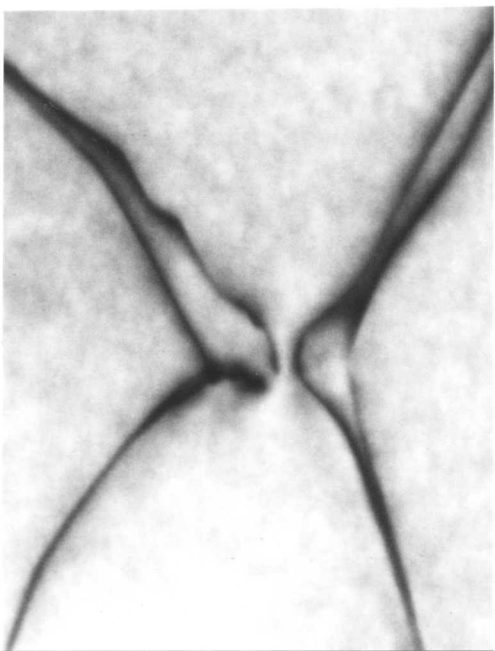
If the interactions were subsequently to follow the scheme proposed in 4.4.3, a structure similar to that shown in 4.20(d) would be formed. Figure 4.23 shows that the reaction did occur. This figure



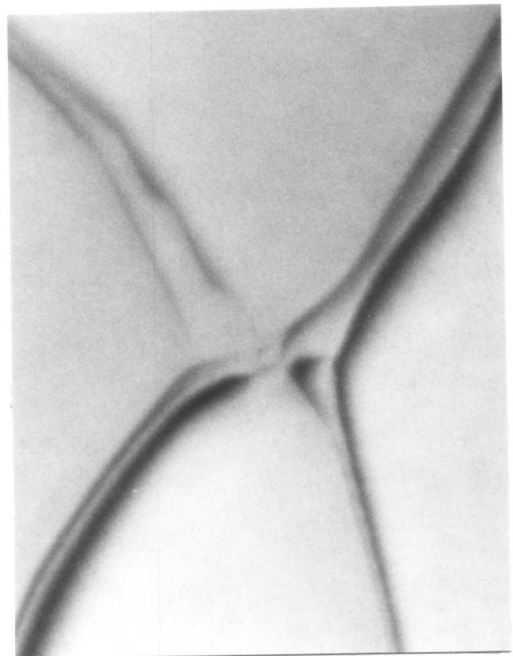
(a)  $\bar{1}1\bar{1}$



(b)  $1\bar{1}1$



(c)  $\bar{1}1\bar{1}$



(d)  $2\bar{2}0$

100 nm

Fig. 4.22. For figure caption, see overleaf.

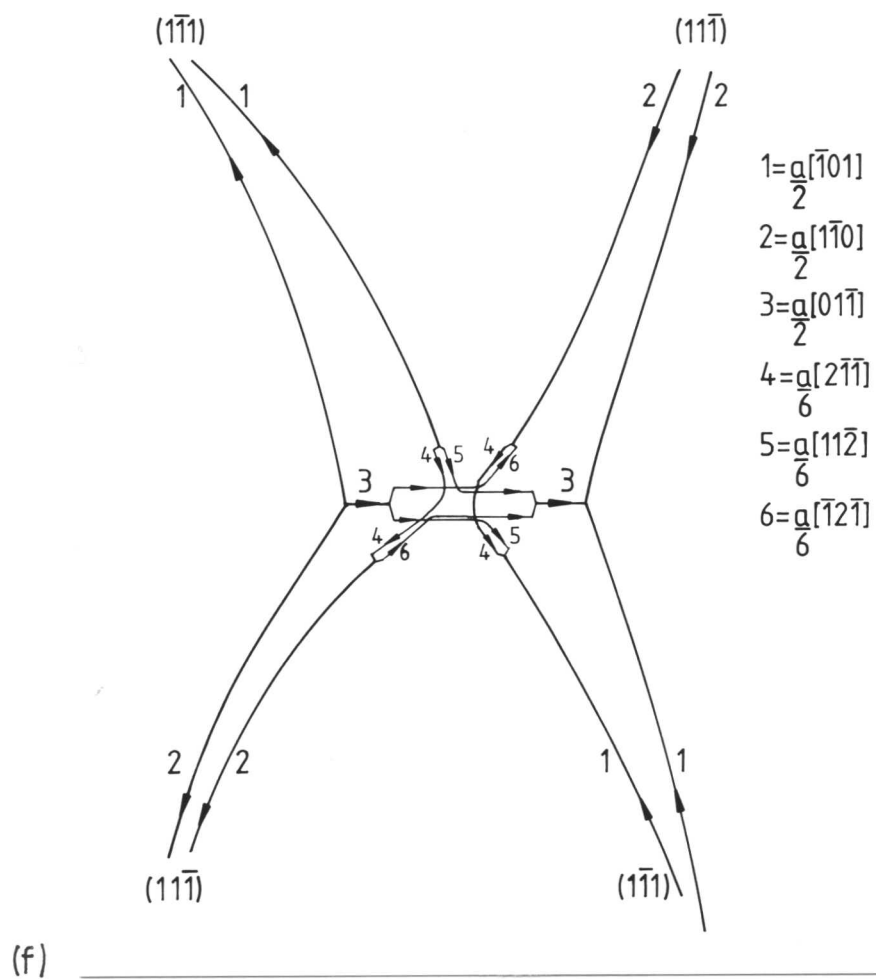
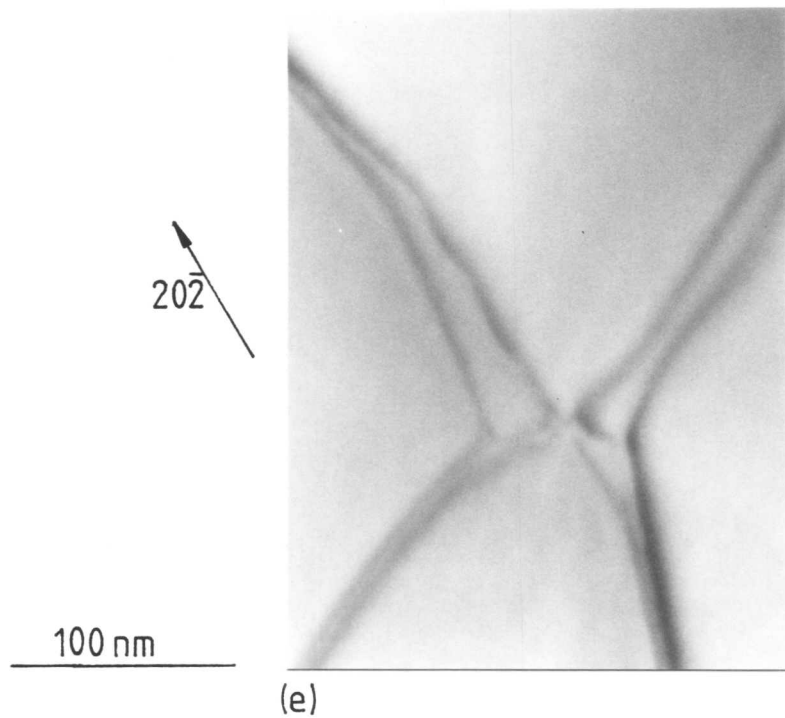
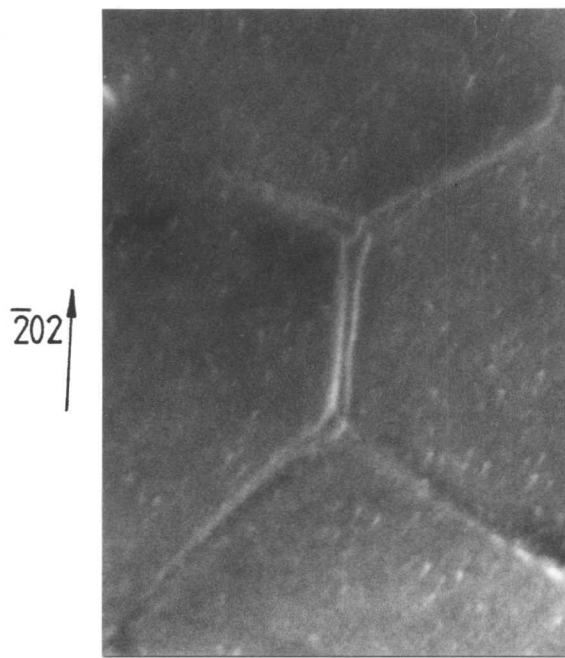
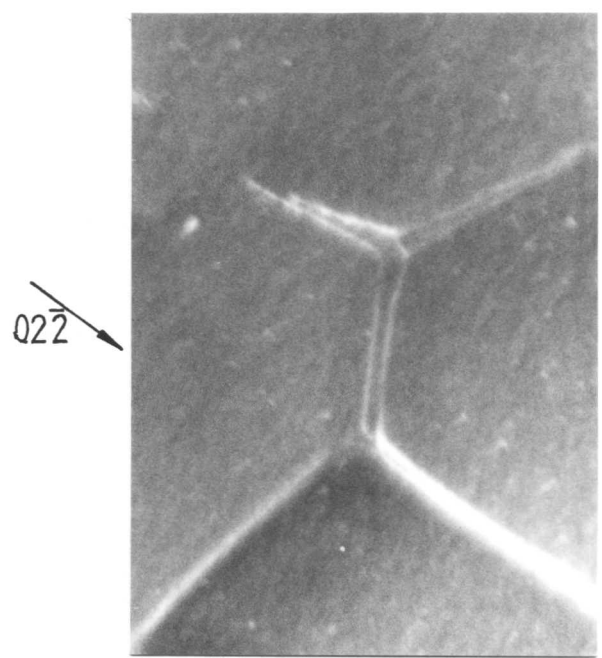


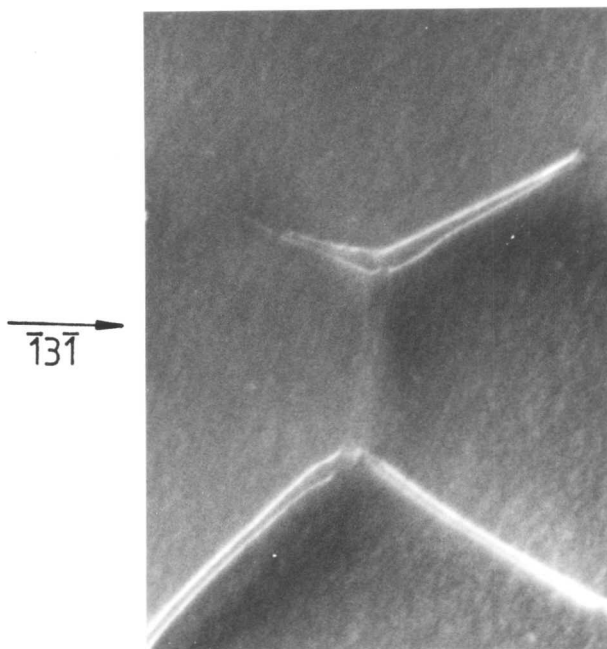
Fig. 4.22. Part of a bright field  $\underline{g}\cdot\underline{b}$  analysis showing an early stage (fig. 4.20b and c) of the interaction between two  $a\langle 110\rangle$  superdislocations on two  $\{111\}$  planes. In the schematic diagram of the interaction (f), it has been assumed that the dislocation dissociation is on  $(111)$ . The  $\underline{g}\cdot\underline{b}$  values of the  $a/2\langle 110\rangle$  dislocations are given in table 4.2. (foil normal:  $\sim[111]$ ).



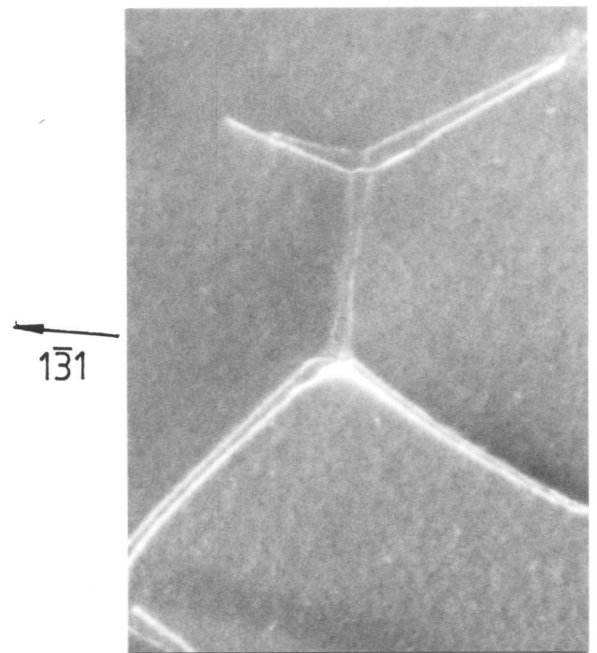
(a)



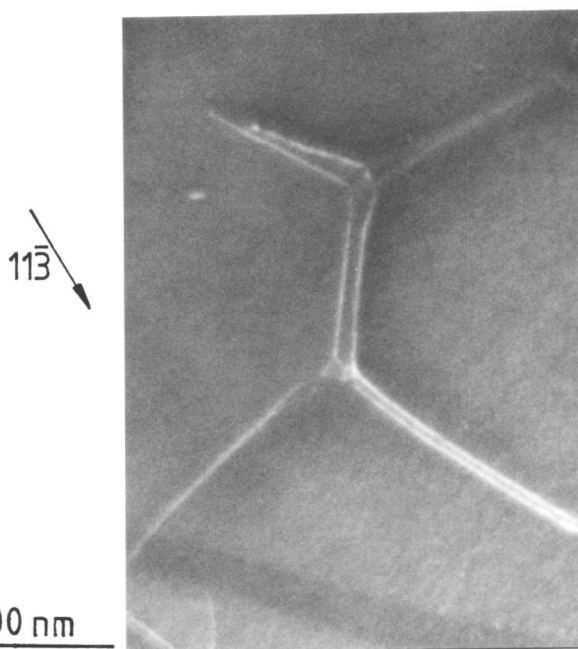
(b)



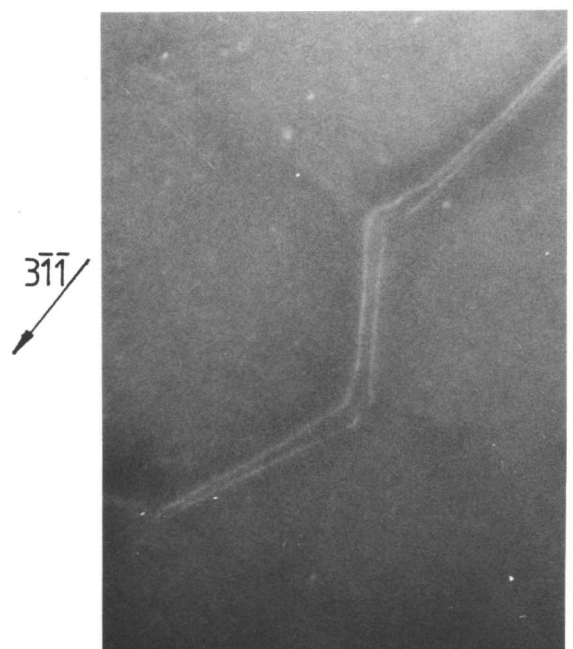
(c)



(d)

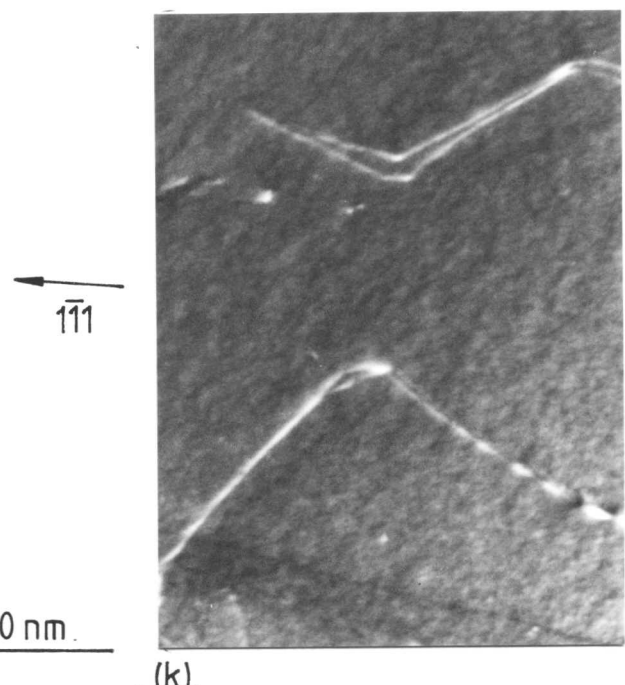
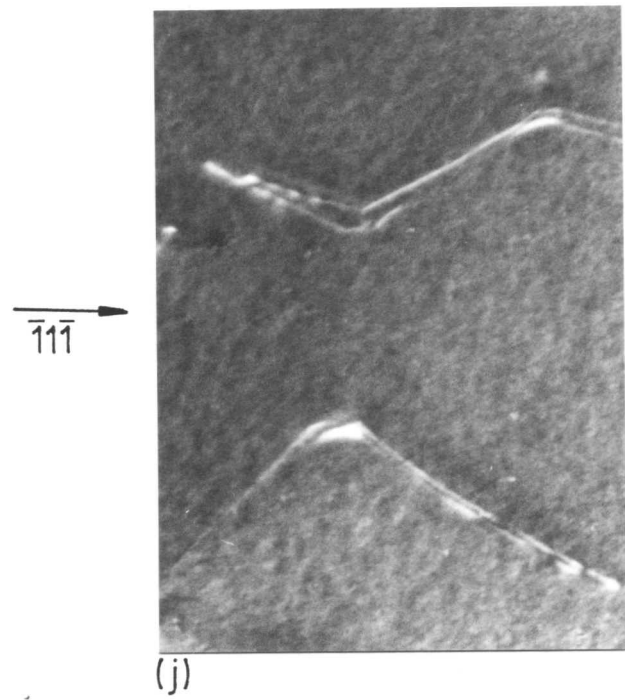
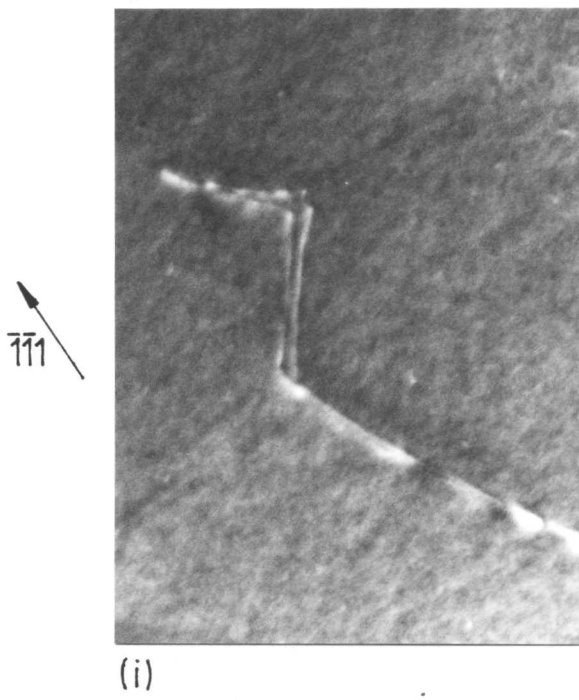
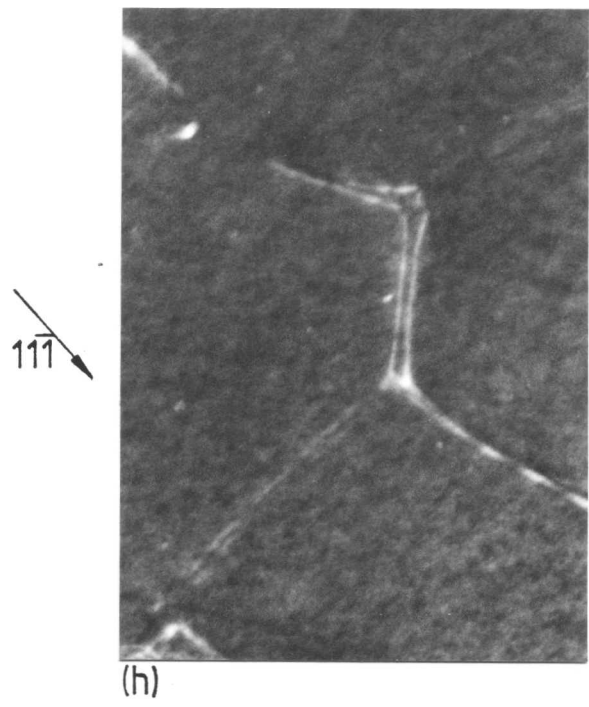
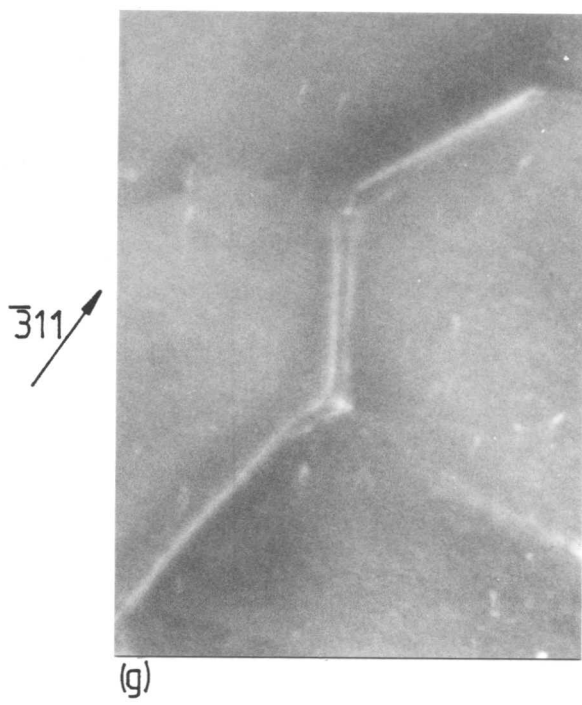


(e)



(f)

Fig. 4.23. For figure caption, see next page but one.



100 nm

Fig. 4.23. For figure caption, see overleaf.

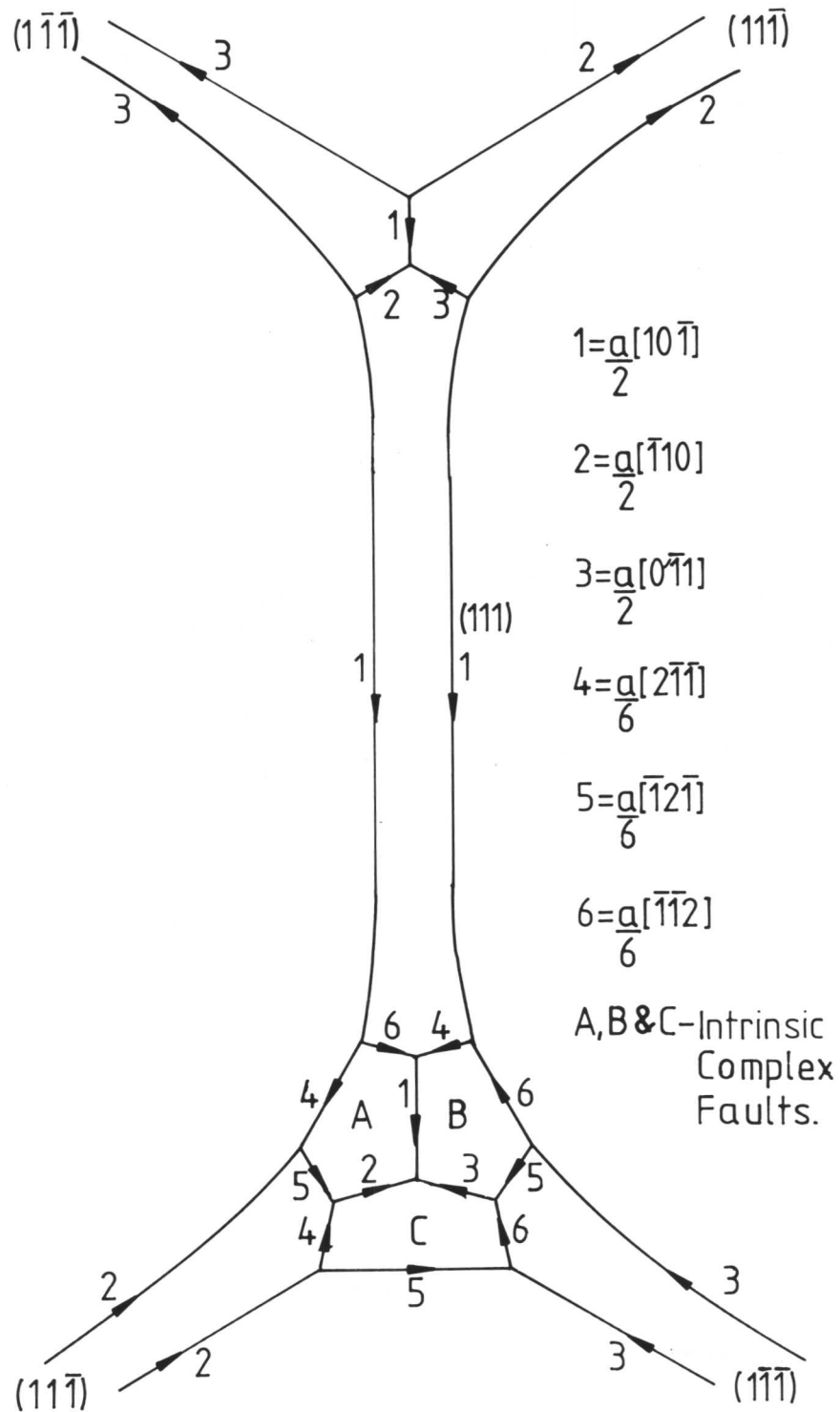


Fig. 4.23. Weak beam dark field TEM micrographs taken in conditions between  $W_{(\underline{g}, 2\underline{g})}$  and  $W_{(\underline{g}, 4\underline{g})}$  showing dislocation configuration, shown in figure 4.20(d), formed after interaction between two  $a\langle 110 \rangle$  superdislocations on different  $\{111\}$  planes. The  $\underline{g}, \underline{b}$  values for the dislocations in the configuration are given in table 4.3. A schematic representation of the configuration is shown in (e) assuming that the nodal regions both lie on (111) (foil normal:  $\sim [111]$ ).

shows a full weak beam  $\underline{g}\cdot\underline{b}$  analysis of the interaction; the  $\underline{g}\cdot\underline{b}$  values for the identified dislocations are tabulated in Table 4.3. In this case the interaction occurred between an  $a[\bar{1}10]$  superdislocation on  $(11\bar{1})$  and an  $a[0\bar{1}1]$  on  $(1\bar{1}\bar{1})$ . The superdislocation produced by the interaction was  $a[10\bar{1}]$  on  $(111)$ . The partial dislocation structure at the nodal points, which is shown in figure 4.23(1) was essentially the same as that described in 4.4.3 and shown in figure 4.19(d). The dislocation analysis can be confirmed by referring to table 4.3. It was not possible to determine the identity of all of the dislocations due to the fine structure of the interactions and the possible effect of the complex faults A, B and C on the images of the dislocations between them. However, the  $a/2\langle 110\rangle$  dislocations forming the superdislocations and the top node were identified unambiguously as were the  $a/6\langle 211\rangle$  partial dislocations between the complex faults and the unfaulted crystal. The identities of the remaining dislocations were deduced from the known dislocations and the image contrast was compared with that predicted in table 4.3. In this way it was possible to identify all the dislocations of the network shown in figure 4.23.

From the dislocation analysis it was concluded that faults A, B and C were intrinsic complex faults. These faults have the highest energy of any of the planar defects possible in  $L1_2$  and should consequently be unstable with respect to the SSFs and APB. It is thought that the CFs are metastable because the desire of the dislocations to minimise their own energy by adopting a screw orientation and to balance the forces at the three-way supernode is greater than the driving force to annihilate the CFs. Consequently, the configuration shown in figure 4.23 could lower its energy further if the complex faults were annihilated and replaced by a lower energy fault. Many of the nodes observed appeared to form extended nodes with no internal structure and these are discussed below.

Table 4.3.  $\underline{g} \cdot \underline{b}$  values for the dislocations shown in figure 4.23

Micro-graph	Diffract-ion vector (g)	Burgers vector (b)					
		$a/2[10\bar{1}]$ (1)	$a/2[\bar{1}10]$ (2)	$a/2[0\bar{1}1]$ (3)	$a/6[2\bar{1}\bar{1}]$ (4)	$a/6[\bar{1}\bar{1}2]$ (5)	$a/6[\bar{1}2\bar{1}]$ (6)
(a)	$\bar{2}02$	-2	+1	+1	-1	$-\frac{2^*}{3}$	[0]
(b)	$02\bar{2}$	+1	+1	-2	[0]	+1	$[\frac{1}{3}]$
(c)	$\bar{1}3\bar{1}$	[0]	+2	-2	$-\frac{2^*}{3}$	$+\frac{2^*}{3}$	$+\frac{4^*}{3}$
(d)	$1\bar{3}1$	[0]	-2	+2	$+\frac{2^*}{3}$	$-\frac{2^*}{3}$	$-\frac{4^*}{3}$
(e)	$11\bar{3}$	+2	[0]	-2	$+\frac{2^*}{3}$	$+\frac{4^*}{3}$	$+\frac{2^*}{3}$
(f)	$3\bar{1}\bar{1}$	+2	-2	[0]	$+\frac{4^*}{3}$	$[-\frac{1}{3}]$	$-\frac{2^*}{3}$
(g)	$\bar{3}11$	-2	+2	[0]	$-\frac{4^*}{3}$	$[\frac{1}{3}]$	$+\frac{2^*}{3}$
(h)	$11\bar{1}$	+1	[0]	-1	$[\frac{1}{3}]$	$+\frac{2^*}{3}$	$[\frac{1}{3}]$
(i)	$\bar{1}\bar{1}1$	-1	[0]	+1	$[-\frac{1}{3}]$	$-\frac{2^*}{3}$	$[-\frac{1}{3}]$
(j)	$1\bar{1}1$	[0]	-1	+1	$[\frac{1}{3}]$	$[-\frac{1}{3}]$	$-\frac{2^*}{3}$
(k)	$\bar{1}1\bar{1}$	[0]	+1	-1	$[-\frac{1}{3}]$	$[\frac{1}{3}]$	$+\frac{2^*}{3}$

[ ] - Invisible

\* - See below

* $\underline{g} \cdot \underline{b}$	Fault to right of dislocation	Fault to left of dislocation
$+\frac{2}{3}$	I	V
$-\frac{2}{3}$	V	I
$+\frac{4}{3}$	V	I
$-\frac{4}{3}$	I	V

#### 4.5.5 Extended nodes in superdislocation networks

The occurrence of extended intrinsic and extrinsic nodes in disordered materials has frequently been reported; see, for instance, Aerts, Delavignette, Siems and Amelinckx (1962) in Si, Loretto (1964) in Au-Sn and Gallagher (1966) in Ag-In. In contrast, the occurrence of extended intrinsic and extrinsic nodes in  $L1_2$  has only been reported twice other than in this investigation. The first observations were made by Howe et al. (1974) in deformed and annealed  $Zr_3Al$ ; their results are compared to those gained from this investigation in 4.6. More recently, Baker, Viens and Schulson (1984) commented on their existence.

Extended nodes were frequently observed in alloys A, D and G. Figures 4.24 and 4.25 are two examples which will be discussed. Figure 4.24 shows a single node, while figure 4.25 shows a planar network on (111) containing a number of extended nodes.

A weak beam  $\underline{g}\cdot\underline{b}$  study was undertaken on one defect; selected micrographs are shown in figure 4.24. The three superdislocations entering the node were identified as pairs of  $a/2\langle 110\rangle$  dislocations. These were all pure screw and were on (111) at the centre of the node. As previously discussed, they were displaced from their original glide plane to form the node. The contrast from the central fault was consistent with a stacking fault displacement of  $\pm a/3[111]$ ; the fault was visible in all diffraction conditions other than  $\underline{g}=(2\bar{2}0)$ . No fault fringes were observed because the fault is almost parallel to the foil surface. The fault must be bounded by six partial dislocations. Segments 1, 3 and 5 (fig. 4.24) were not characterised as any contrast resulting from them became confused with that from the fault. Segments 2, 4 and 6 were identified. They could be  $\pm a/3[111]$ ,  $a/6\langle 211\rangle$  or  $a/3\langle 211\rangle$ . The Frank partial was quickly eliminated as it would be invisible in all conditions except  $\underline{g}=(200)$ . This was clearly not the case as the dislocations under consideration were clearly seen in other conditions. If the dislocations

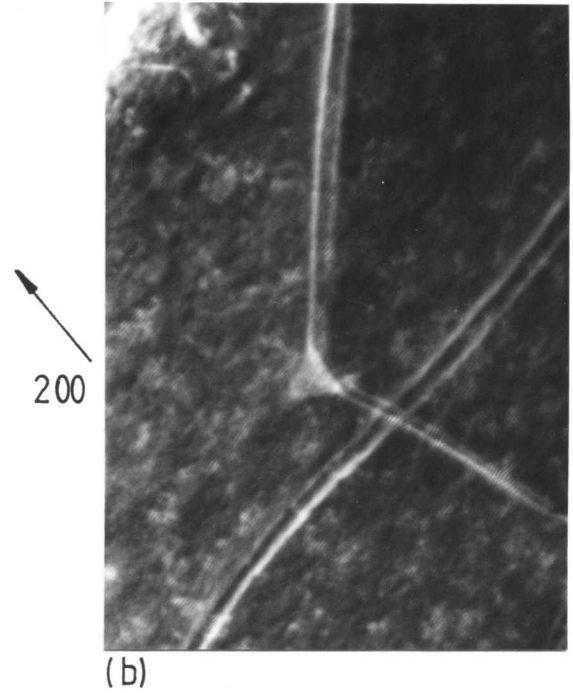
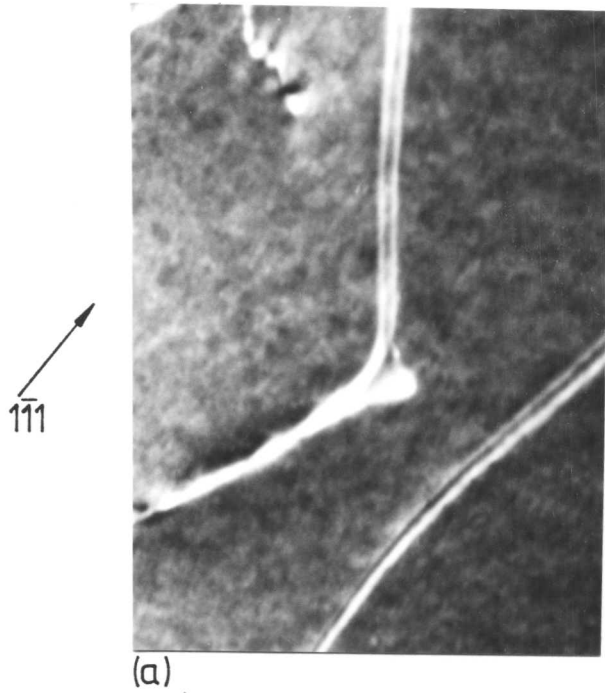
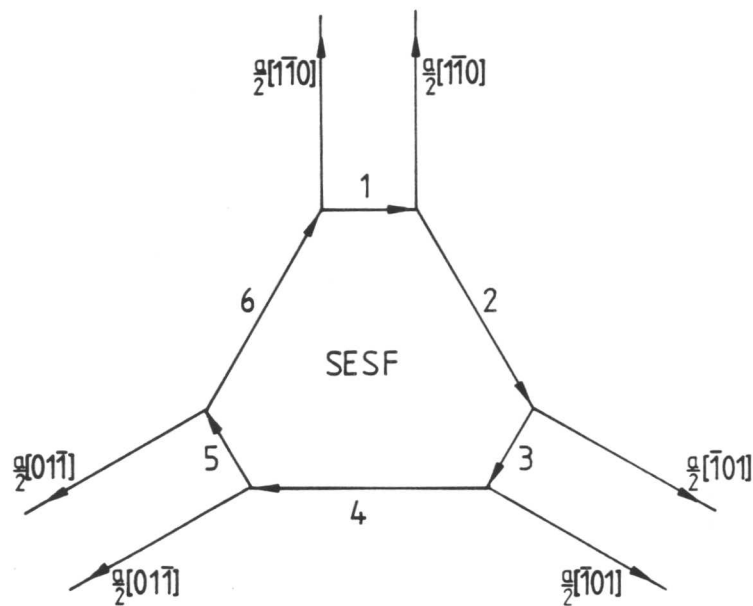
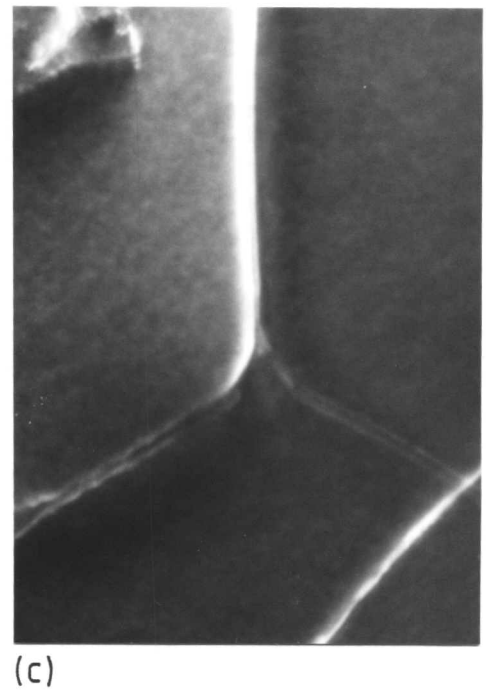


Fig. 4.24. Examples of weak beam dark field TEM micrographs taken in  $W(\underline{g}, 2.5\underline{g})$  conditions showing the dislocations and fault contrast at an extended node. The dislocation configuration identified by  $\underline{g} \cdot \underline{b}$  analysis is shown in (d). (foil normal:  $\sim[111]$ ).



100 nm



- 1 =  $\frac{\alpha}{6}[\bar{1}\bar{1}2]$
- 2 =  $\frac{\alpha}{3}[\bar{2}11]$
- 3 =  $\frac{\alpha}{6}[\bar{1}2\bar{1}]$
- 4 =  $\frac{\alpha}{3}[11\bar{2}]$
- 5 =  $\frac{\alpha}{6}[2\bar{1}\bar{1}]$
- 6 =  $\frac{\alpha}{3}[1\bar{2}1]$

(d)

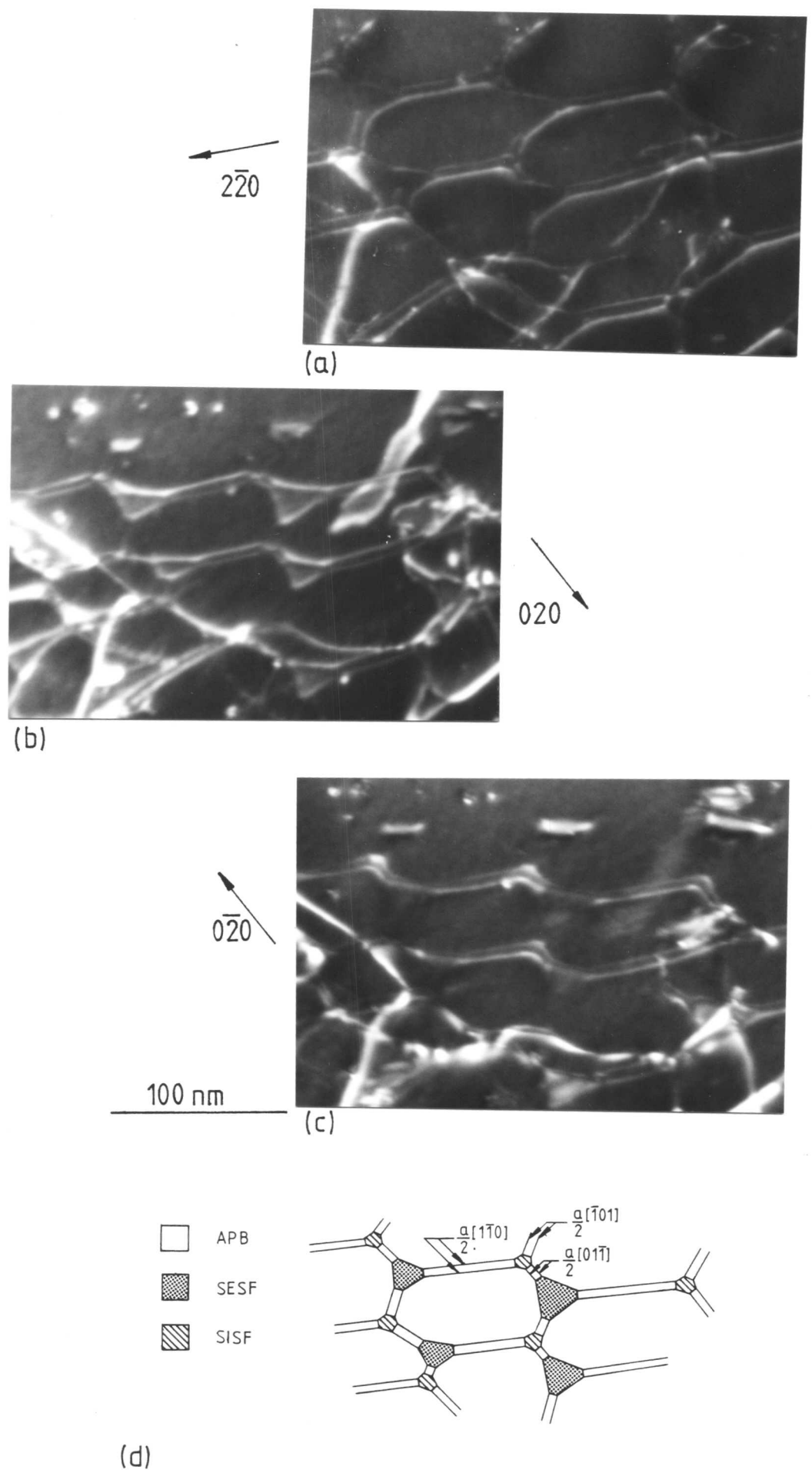


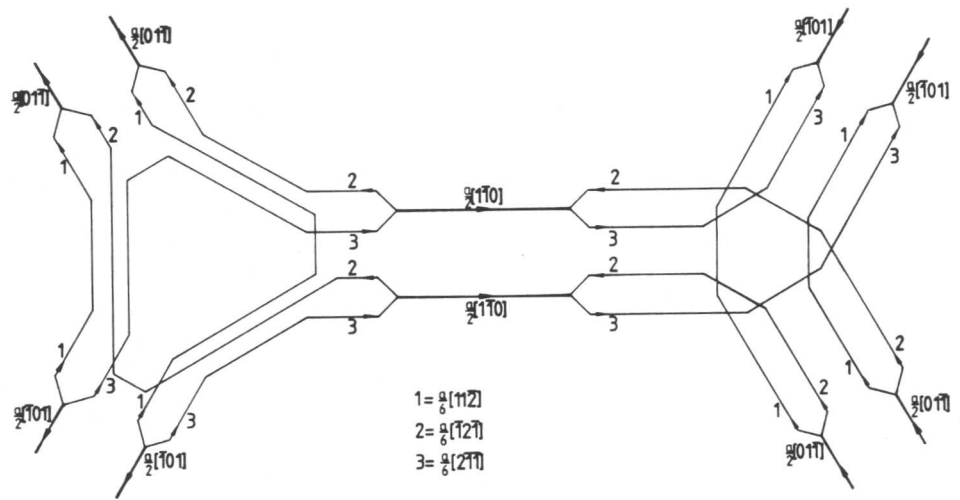
Fig. 4.25. Part of a weak beam dark field TEM  $g \cdot b$  analysis, using  $\bar{W}(g, 2.5g)$ , showing a planar superdislocation network on (111) with extended nodes at the nodal points. The dislocations identified are shown in (d). The SESFs are larger than the SISFs. Note the change in contrast from the SESFs in  $(020)_{3g \pm g}$  conditions (b and c) may be due to anomalous contrast from SESFs<sup>-</sup> (see 3.3.8 for details). (foil normal:  $\sim [001]$ ).

were  $a/6\langle 211 \rangle$ , as in the configuration shown in figure 4.23, the defect would be a CF; if the dislocations were  $a/3\langle 211 \rangle$  the defect would be a SSF.

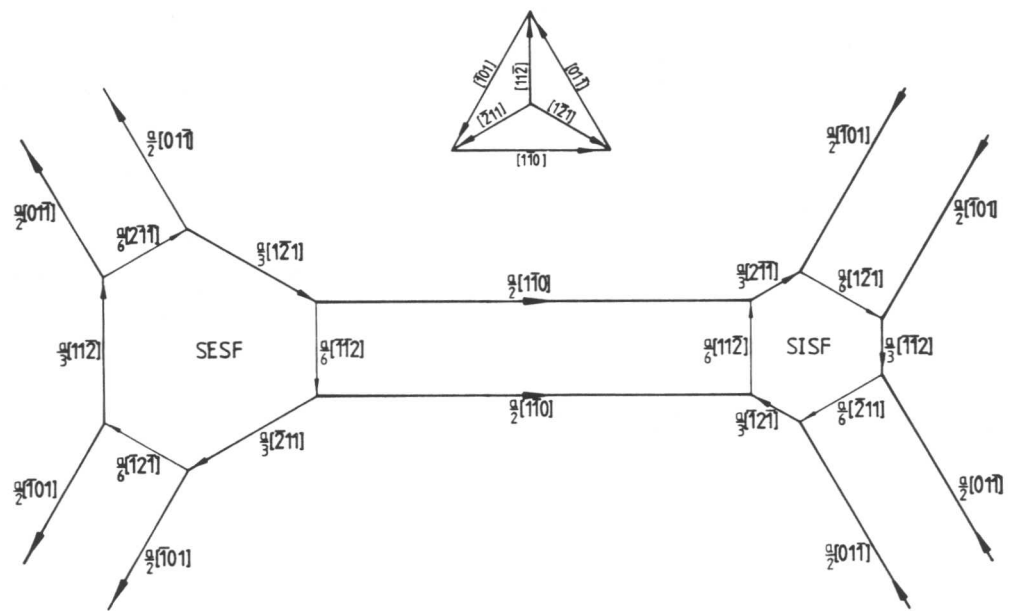
The analysed dislocation configuration is shown in figure 4.24(d). Segments 1, 3 and 5 were deduced from the known dislocations to be  $a/6\langle 211 \rangle$  partial dislocations. The dislocation line sense was determined using a  $\pm g$  pair and dislocation 2 was used to determine the fault type. In this case the fault was found to be a superlattice extrinsic stacking fault.

Figure 4.25 shows a network consisting of two different sizes of superdislocation nodes. Dislocation analysis similar to that described above was carried out on the network. It showed that the larger nodes were SESF while the smaller nodes were SISF (fig. 4.25d). This analysis was supported by the contrast change observed in weak beam conditions at the larger nodes on reversing  $g$ . This observation was only used to confirm the dislocation analysis as the contrast from the smaller nodes cannot easily be observed (3.3.8). The network consisted of alternating intrinsic and extrinsic nodes joined by screw superdislocations (fig. 4.25d).

Extended nodes form from the metastable structure previously proposed and observed (figs. 4.19d and 4.20) in the following way. It can be seen that the central points of the nodes in 4.19(c) contain a small area of extrinsic or intrinsic SSF. Once the activation energy for SSF growth has been overcome, it is proposed that this region will extend on (111) forcing the  $a/6\langle 211 \rangle$  partial dislocations apart until it eventually adopts the structure shown in figure 4.26(a). The three  $a/6\langle 211 \rangle$  partial dislocations bounding the faults would be so close together that their spacing is of the order of the image width and in the TEM they will behave as a  $a/3\langle 211 \rangle$  partial dislocation. The resultant structure would adopt the low energy screw configuration (fig. 4.26b). The driving force for this reaction will be, at least in part, due to the reduction in the area



(a)



(b)

Fig. 4.26. Schematic illustration of the dislocation structure at an extended intrinsic node and an extended extrinsic node on (111). The structure is shown in terms of  $a/6 \langle 211 \rangle$  partial dislocations (a) and with the  $a/6 \langle 211 \rangle$  partials summed to produce the configuration observed in the TEM (b).

of high energy CF, but it is also likely to be accelerated by the presence of alloying elements, in this investigation Ti, which will segregate to the SSFs, particularly the SESF. This effect is discussed in detail in 6.3.4.

#### 4.6 Conclusions and Comparison of the Networks with those Observed by Other Workers

By following a similar approach to that adopted for interactions between  $a/2\langle 110 \rangle$  dislocations in austenitic stainless steels (Whelan, 1959), the hexagonal dislocation supernodes and networks described theoretically and observed experimentally in the  $\gamma'$  of single crystal superalloys have been explained. They were formed by interactions between two  $a\langle 110 \rangle$  superdislocations, consisting of two  $a/2\langle 110 \rangle$  dislocations on the same or different  $\{111\}$  planes bounding an APB and enclosing an angle of  $120^\circ$  between their Burgess vectors, to produce a third  $a\langle 110 \rangle$  superdislocation. Each of the  $a/2\langle 110 \rangle$  dislocations was assumed to have the capacity to dissociate into two  $a/6\langle 211 \rangle$  partial dislocations on the  $\{111\}$  habit plane. This scheme of dislocation interactions was shown to produce networks of superdislocations with supernodes at the junction points. With the nodal reactions in the metastable state (fig. 4.19d), the networks were found to be equivalent to those predicted by Amelinckx (1979) (fig. 4.21). In this state the nodal points support large CFs so that the dislocations can adopt a lower energy pure screw orientation and balance the forces between the dislocations at the supernodes. In his paper of 1979 Amelinckx states that up to that time no observations of hexagonal networks in  $L1_2$  have been reported. This investigation rectifies this situation.

In the configuration shown in figure 4.23 an activation barrier exists which suppresses the nucleation and growth of a more stable SSF at the nodal points. It has been shown that once the activation barrier is

exceeded, SSFs consume the nodal area to create the stable lowest energy nodal structure of alternating intrinsic and extrinsic SSFs linked by superdislocations. By measuring the superdislocation spacing and the size of the supernodes, it was possible to evaluate the APB energy and the SSF energies from one network. This process is described in 6.3. No other suitable method for the evaluation of SSF energy has been developed before this investigation. It was observed that the nodal SESFs were considerably larger than the nodal SISFs. It is thought that this may be a function of the concentration of certain alloying elements, as discussed in 6.3.4.

Howe et al. (1974) published a paper which reported the observation of hexagonal networks in the  $L1_2$  compound,  $Zr_3Al$ . Amelinckx (1979) was clearly not aware of this paper when he wrote his article as no reference was made to it. In the paper, Howe et al. appear to misinterpret the evidence in their micrographs. They correctly state that the  $L1_2$  lattice repeat is  $a\langle 110 \rangle$  and that this can be dissociated to form two  $a/2\langle 110 \rangle$  dislocations bounding an APB (4.3.2) or to form two  $a/3\langle 211 \rangle$  dislocations bounding an SSF (4.3.3). But they incorrectly assume that only one of these dissociation mechanisms can occur at any time so that any dislocations which dissociate can do so by only one method. They assume that dissociation of  $a\langle 110 \rangle$  into two  $a/3\langle 211 \rangle$  partial dislocations occurs and interaction between these pairs produces the network shown in figure 4.27. This allows no segments of  $a/2\langle 110 \rangle$  dislocation pairs between the alternating SESFs and SISFs. It is clear from figure 10 (Howe et al., 1974) that the extended faults are linked by long straight dislocation pairs which exhibit contrast which is consistent with superdislocations but inconsistent with screw  $a/3\langle 211 \rangle$  pairs. It is suggested that the dislocation networks observed in  $Zr_3Al$  are analogous to those observed, and described in the  $\gamma'$  precipitate of cold deformed and annealed single crystal superalloys (4.5.5). It is worth noting that Howe et al. observed the SISFs and SESFs to be equally extended. This is in

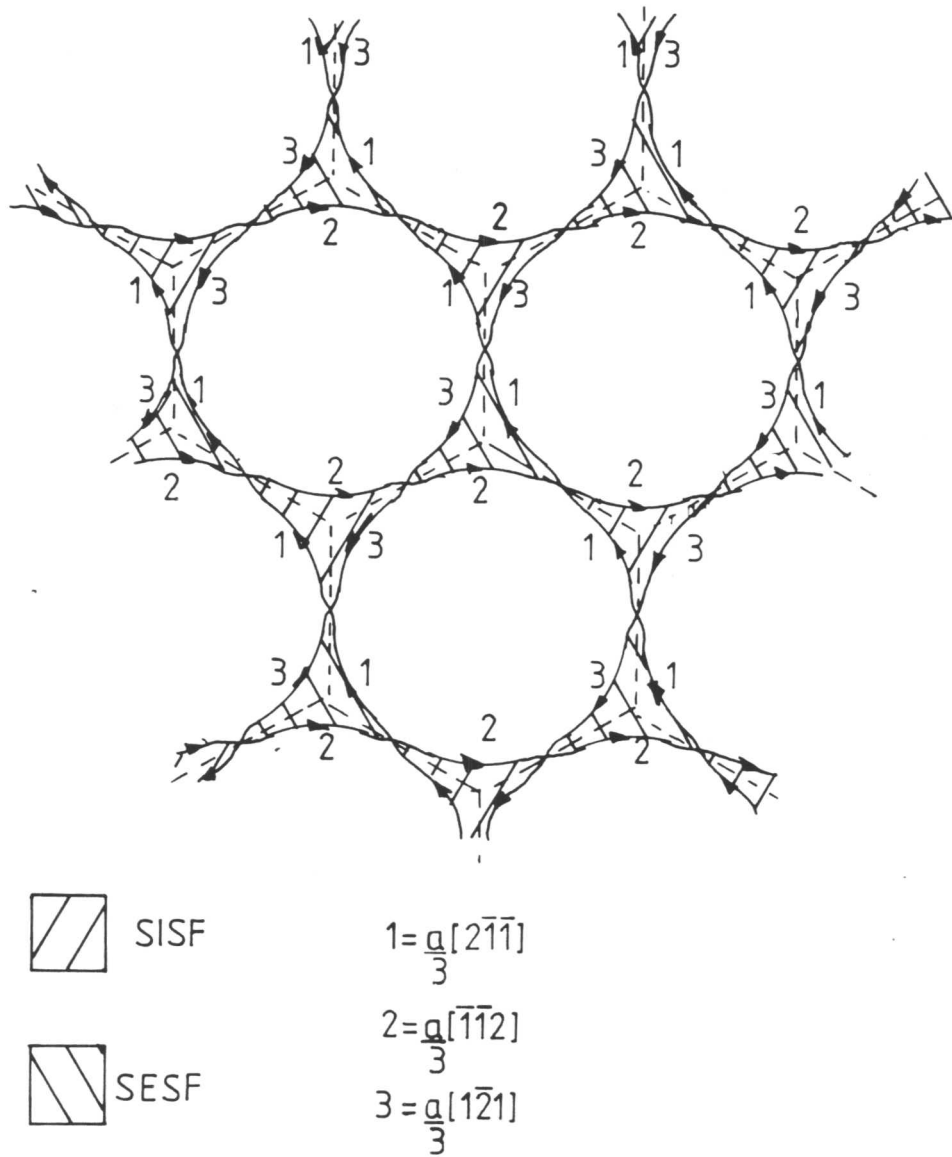


Fig. 4.27. Schematic illustration of the super dislocation network proposed by Howe et al. (1972). Note that there are no  $a/2 \langle 110 \rangle$  dislocation pairs between the nodal points.

marked contrast to this investigation where SESFs were considerably larger than SISFs- see 6.3.4 for discussion.

Although the interaction to form supernodes was by far the most significant to be observed, many other dislocation interactions were observed and some of these, which were relevant to the investigation as a whole, are discussed in the following chapter.

## CHAPTER 5

### FURTHER DISLOCATION INTERACTIONS

#### 5.1 Introduction

Some of the other dislocation interactions observed in deformed and annealed  $\gamma'$  of alloys A, D and G are discussed in this chapter. It includes observations of isolated superdislocations, superdislocation dipoles and large planar faults. Mechanisms for the formation of superdislocation dipoles and planar faults are suggested. Consideration is also given to the formation of square and rectangular dislocation networks by dislocations with Burgers vectors which enclose an angle of  $90^\circ$ .

#### 5.2 Observations of Isolated Dislocations

##### 5.2.1 Superdislocations in the annealed microstructure

At the annealing temperature of 1173K enough energy is available to promote climb of the unpaired  $a/2\langle 110 \rangle$  dislocations in the  $\gamma$  matrix. This process considerably increases the probability of two dislocations of the same type gliding on the same  $\{111\}$  plane. These dislocations can 'pair-up' to form superdislocations which then lower the dislocation density in the  $\gamma$  by gliding into the  $\gamma'$ . Once inside these superdislocations can interact with others entering the  $\gamma'$  and those already present after deformation. In many cases these gliding  $\{111\}$  superdislocations reduced strain energy by forming hexagonal or square dislocation networks as discussed in 4.5 and 5.3 respectively. Some superdislocations, however, remained isolated. Although the majority of these were pure screw  $a/2\langle 110 \rangle$  dislocation pairs on  $\{111\}$  planes some (fig. 5.1) were seen to be curved; probably due to pinning of the superdislocations at the  $\gamma/\gamma'$  interface. The screw orientation was most usually adopted to reduce the dislocation energy.

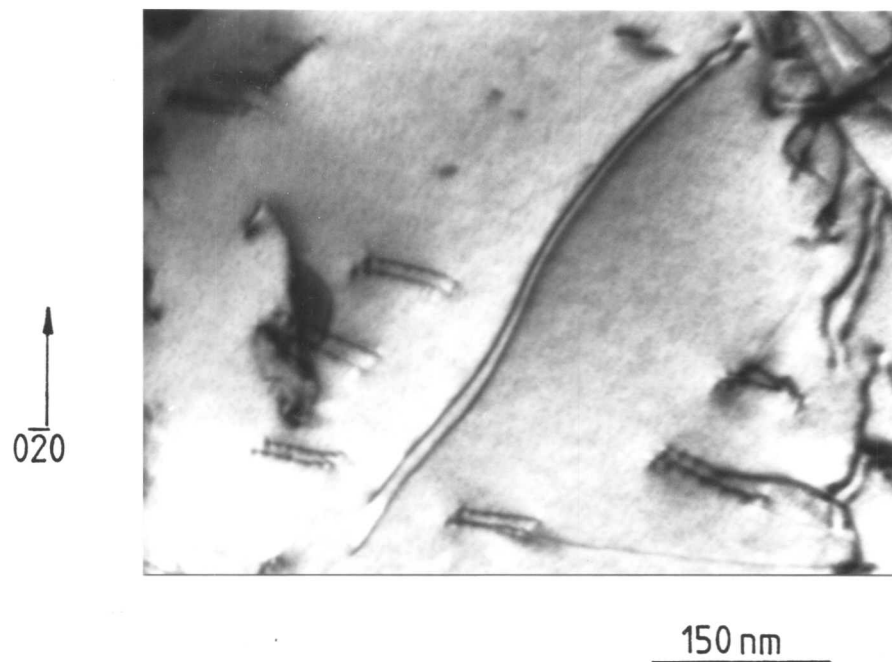


Fig. 5.1. Bright field TEM micrograph showing curved superdislocation in  $\gamma'$ . (foil normal:  $\sim[011]$ ).

It has been suggested (e.g. by Suzuki et al., 1979) that the straightness of the superdislocations is an indication that cross-slip onto  $\{001\}$  has occurred to form Kear-Wilksdorf locks (Kear and Wilksdorf, 1962). This was by no means always the case, although some superdislocations on  $\{001\}$  planes were observed (fig. 5.2). A tilting experiment in the TEM (3.3.11) showed most of the superdislocations to be resident on  $\{111\}$  planes. It was also noted that dislocations in the hexagonal networks invariably adopted a straight screw orientation on  $\{111\}$  planes to minimise the network energy. The cross-slip necessary to produce these networks took place between  $\{111\}$  planes, rather than from  $\{111\}$  planes to  $\{001\}$  planes (fig. 4.25). It is concluded that no generalisation which states that straight screw superdislocations are locked onto  $\{001\}$  planes by the Kear-Wilksdorf mechanism can be made because such dislocations have been observed on  $\{111\}$  planes.

As stated, slip most commonly occurred on  $\{111\}$  planes in  $\gamma'$ . However, cross-slip from  $\{111\}$  planes to  $\{001\}$  planes has been cited many times to explain the unusual work-hardening characteristics of  $\gamma'$  strengthened alloys (for a review see Pope and Ezz, 1984). Cross-slip onto  $\{001\}$  was seen to occur during the deformation and annealing of alloys A, D and G. Figure 5.2 shows the dislocations at A have  $\{111\}$  slip traces while those at B could have  $\{100\}$  slip traces. Observations of  $\{001\}$  slip traces were unusual and it was concluded that most of the superdislocations were on  $\{111\}$  planes. It appeared that cross-slip usually occurred between different  $\{111\}$  planes rather than from  $\{111\}$  onto  $\{001\}$  planes. Very few superdislocations were observed on  $\{001\}$  planes, so it was assumed that Kear-Wilksdorf locking (Kear and Wilksdorf, 1962) was insignificant in specimens annealed at 1173K.

### 5.2.2 Dipoles in annealed microstructures

Analysis of dislocation pairs which exhibited a change in spacing

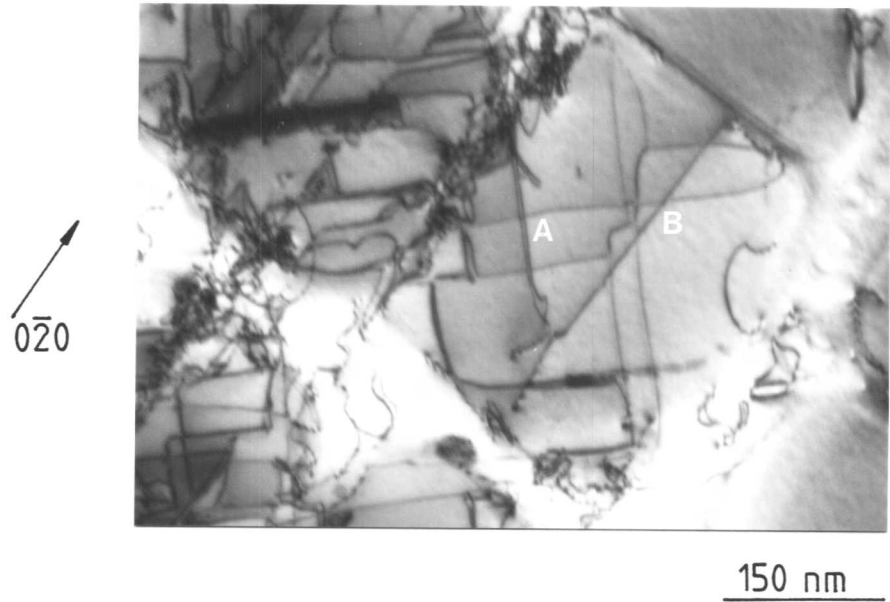


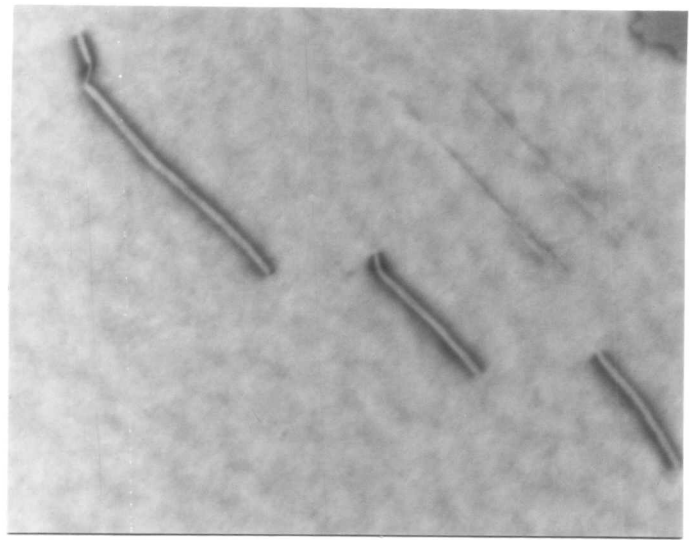
Fig. 5.2. Bright field TEM micrograph showing superdislocations lying on  $\{111\}$  (A) and  $\{001\}$  (B) planes in  $\gamma'$ . (foil normal:  $\sim[001]$ ).  
*possibly*

when  $\underline{g}$  was reversed were all found to have the image characteristics of dipoles rather than the dissociated APBs suggested in 3.3.8. This was expected as the dissociation shown in figure 3.9 is extremely unlikely to occur as it would require opposite dissociations for each  $a/2\langle 110 \rangle$  dislocation.

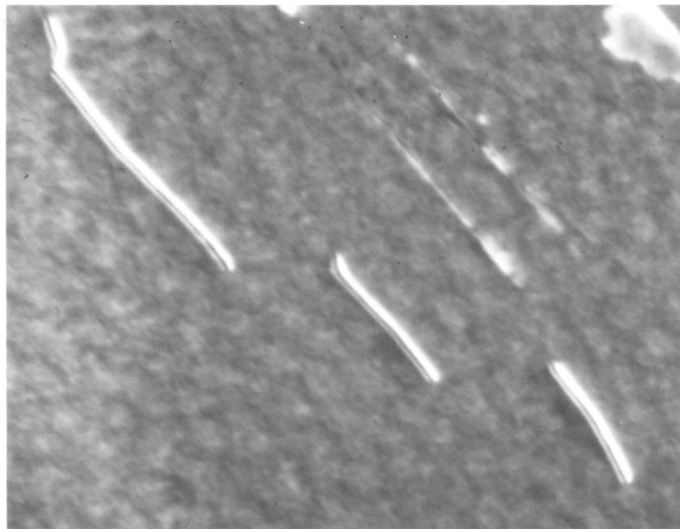
TEM micrographs of dipoles are shown in figure 5.3. It is thought that each of the lines forming the image is a superdislocation. Dipoles are of no direct relevance to the calculation of defect energies but they must be distinguished from superdislocations to prevent misinterpretation of the dislocation images. It is interesting to consider how the dipoles may have been formed. Two methods are to be considered: the first based on the mechanism of Johnston and Gilman (1960) and the second based on the mechanism of Tetelman (1962). Both were proposed to explain dipole formation in disordered structures. These proposals have been developed to explain dipole formation in  $L1_2$  structures.

Johnston and Gilman suggested that an undissociated screw dislocation (AB fig. 5.4a), travelling in its own glide plane, may become jogged either by interaction with another dislocation (Cottrell, 1953) or by cross-slip. If the jog formed is more than one atomic spacing high, the jogged section CD (figure 5.4b) will be sessile on the glide plane. Movement of AB will then drag out a pure edge dipole (fig. 5.4c) behind the gliding screw. Under certain circumstances cross-slip may subsequently occur to produce an edge dislocation loop in the unfaulted crystal (fig. 5.4d). If the dislocation is a screw superdislocation, the same type of process would occur as shown in figure 5.5. The defect produced would be a pure edge superdislocation dipole (fig. 5.5c) which may part to form a superdipole loop. As shown in figure 5.5(e), the region between the  $a/2\langle 110 \rangle$  dislocation loops would be an APB. This mechanism of loop formation was observed in this investigation. Figure 5.6 shows a TEM micrograph of a pure screw superdislocation which is trailing a line

$\overline{111}$

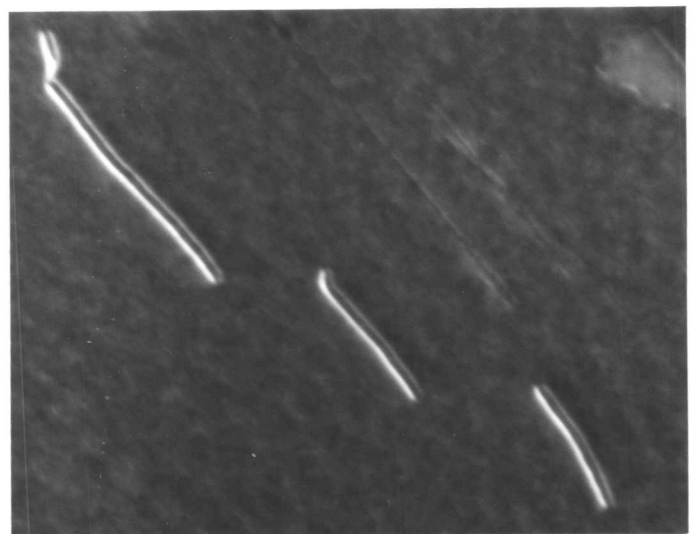


(a)



(b)

$\overline{111}$



(c)

150 nm

Fig. 5.3. TEM micrographs in bright field (a) and  $W_{(g, 3g)}$  weak beam dark field (b and c) showing possible superdislocation dipoles. The weak beam micrographs show the change in spacing on reversing  $g$ . Note there is a large difference in image intensity between the dislocations bounding the APB. See text for details. (foil normal:  $\sim[111]$ ).

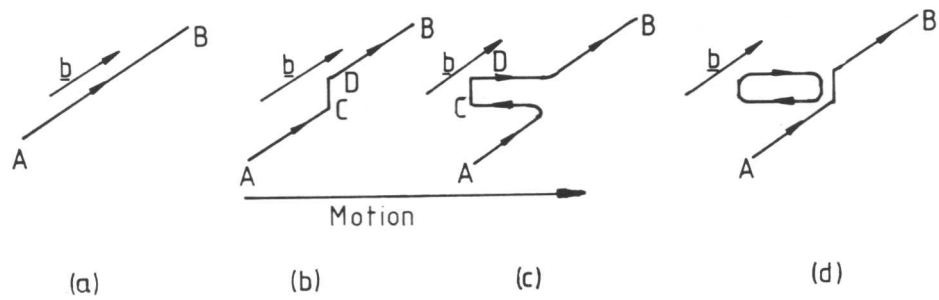


Fig. 5.4. Formation of an edge dipole from a jog on a screw dislocation (b). The jogged segment CD is dragged out to form a dipole (c) which may be pinched off to form a dislocation loop (d).

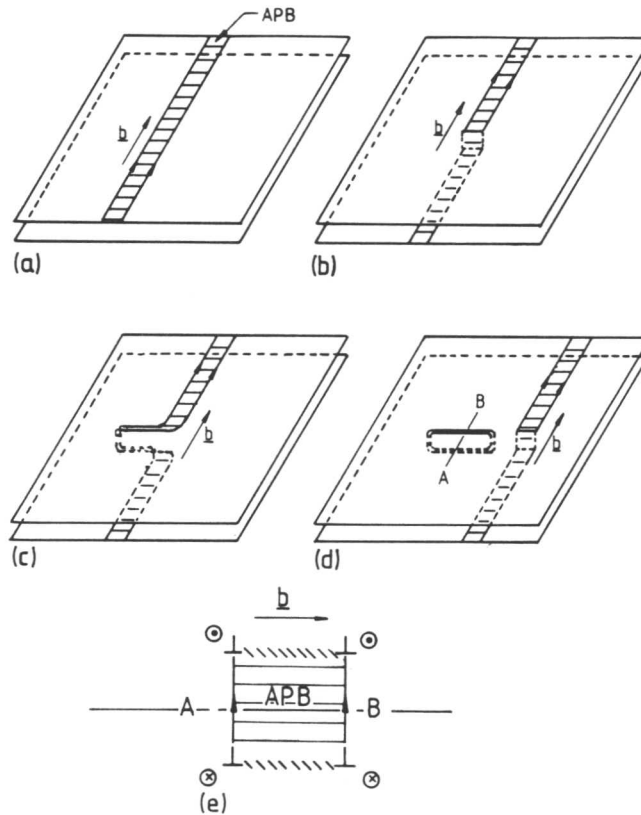


Fig. 5.5. Formation of an edge superdipole by the formation of a double jog in a superdislocation (b). An edge superdipole of APB is dragged out behind the superdislocation (c), which can pinch off to form an APB loop (d). A section through the APB loop along AB is shown in (e).

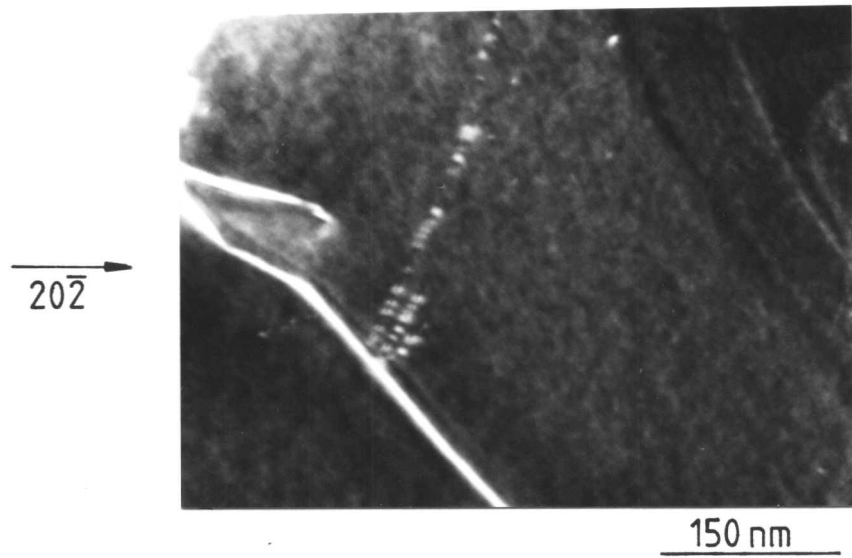


Fig. 5.6.  $W_{(g,3g)}$  weak beam dark field TEM micrograph of an APB trailing a line of small dislocation loops. (foil normal:  $\sim[111]$ ).

of small dislocation loops behind it. However, the Johnston and Gilman mechanism predicts that the trails behind a moving screw dislocation will always be pure edge. While these were often observed, many dipoles (including that shown in figure 5.3) were of mixed character. A model for the formation of these dipoles has been proposed by Tetelman (1962).

Tetelman assumed that during shear deformation two mixed dislocations of equal and opposite Burgers vector may intersect while gliding on parallel  $\{111\}$  planes, as shown in figure 5.7(a). These two dislocations may lower their total energy by reorientation in the same glide plane (fig. 5.7b). If cross-slip occurs at the cross-over point, the sum of the dislocations will be zero and a dipole will form as shown in figure 5.7(c). If the opposite end also cross-slips, as shown in figure 5.7(d), a dipole is created. This model provides an explanation for the occurrence of mixed dislocation dipoles. The model can also be extended to ordered materials as shown in figure 5.8. The initial interaction for this reaction is similar to the mechanism proposed for the creation of hexagonal networks (fig. 4.15). Limited cross-slip must occur at the cross-over points before the superdipole can form. As in the previous case the region between the two  $a/2\langle 110 \rangle$  dislocation loops would contain APB.

Superdipoles of pure and mixed character can be generated by these two mechanisms. In each case they will consist of a loop of APB between  $a/2\langle 110 \rangle$  dislocations. Superdipoles are low energy configurations and it is expected that they will be sessile.

The interaction of two superdislocations to form a jog which could form a superdipole (fig. 5.5) will only occur if one of the superdislocations is stationary at the moment of intersection. If, for any reason, both superdislocations are moving the jogged superdislocation will form an APB tube when it glides away from the intersection. The result is shown in figure 5.9. This process was proposed by Vidoz and Brown (1962)

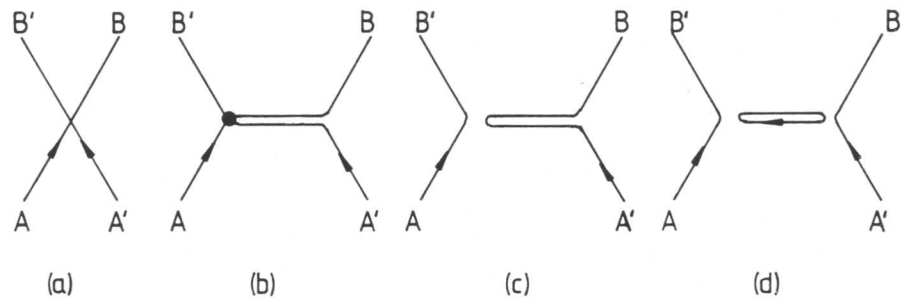


Fig. 5.7. Formation of a dipole by the interaction of two similar dislocations  $AB$  and  $A'B'$  (a). The dislocations lower their energy by reorienting to form a region with equal and opposite parallel Burgers vectors (b). This region may pinch off at  $\bullet$  to form a dipole (c), which may then pinch off to form loop (d). (After Tetelman, 1962.)

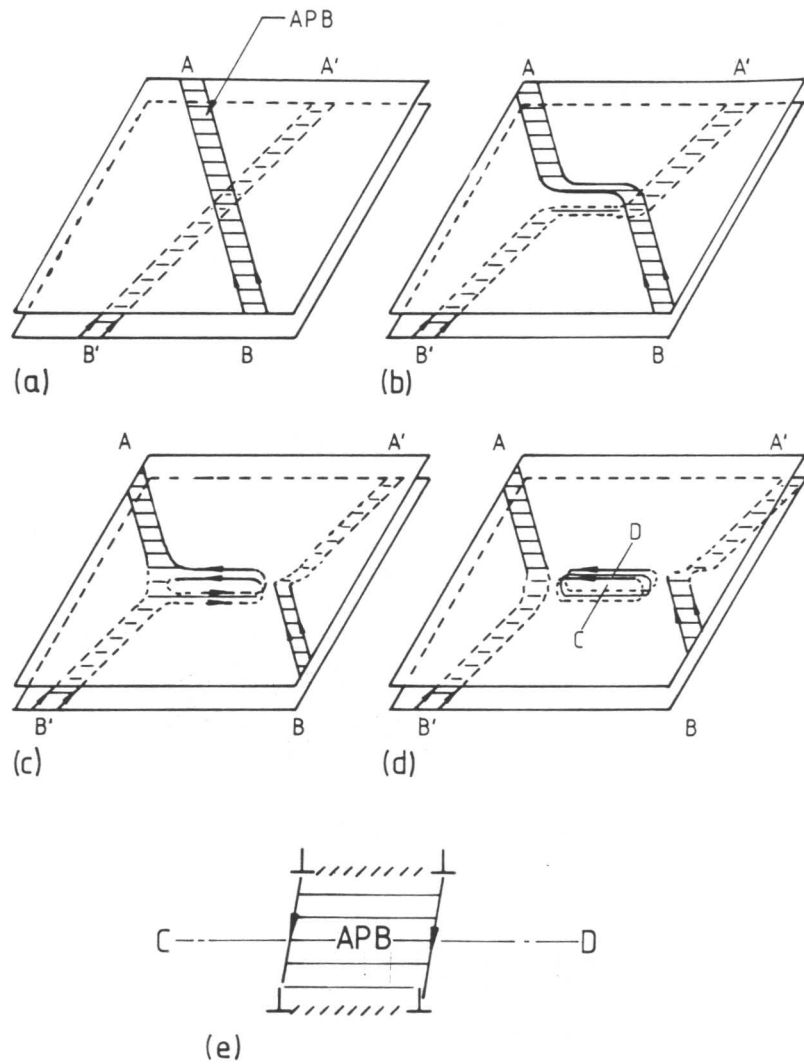


Fig. 5.8. Formation of a superdipole loop from an interaction between two superdislocations (a), showing reorientation to lower the configuration energy (b), cross-slip to form a superdipole (c) and further cross-slip to produce a superdipole loop (d). The loop is shown in section along  $CD$  (e).

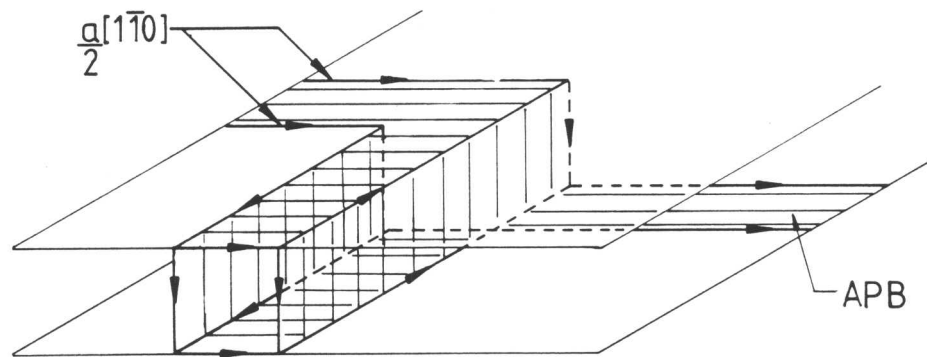


Fig. 5.9. Illustration showing an APB tube which will form if both superdislocations are gliding at the time of interaction.

and has been cited as a strengthening mechanism in  $L1_2$  structures (Kear, 1966). At present, there is little evidence for the existence of APB tubes. Chou, Hirsch, McLean and Hondros (1982) claim to have observed APB tubes in  $Ni_3Al$ . The tubes gave strong contrast in superlattice weak beam imaging conditions but no contrast was observed in fundamental weak beam imaging conditions. The defects observed in this investigation showed strong dislocation contrast in fundamental weak beam and superlattice weak beam imaging conditions. They were assumed to be superdipoles rather than APB tubes.

The superdipoles observed exhibited unusual dislocation contrast in weak beam micrographs as shown in figure 5.3(b) and (c). These micrographs show that the dislocations at the edges of the defects exhibited a large difference in intensity. The difference was judged to be much greater than that from a superdislocation in the same imaging conditions. It is proposed that figure 5.3 shows a superdipole observed along one of its edges, thus, only two dislocation images were seen, and the change in image intensity was caused by the extra layer of APB and the occurrence of one dislocation directly above another (fig. 5.5e and 5.8e).

Dislocation loops and dipoles have previously been reported in  $L1_2$  structures by Kear (1966), Staton-Bevan and Rawlings (1975a) and Baldan (1983). Baldan has drawn similar conclusions to those drawn from this investigation.

In summary, it has been shown that the established techniques for the generation of dipoles in disordered crystals can be adapted to explain the occurrence of dipoles in  $L1_2$  ordered crystals. It is proposed that both the Johnston and Gilman and Tetelman models operate to produce sessile superdipoles of all characters. Unusually, screw dipoles were observed. In disordered materials these would annihilate by cross-slip but in  $\gamma'$  they were stabilised, probably by the APB regions. The loops and

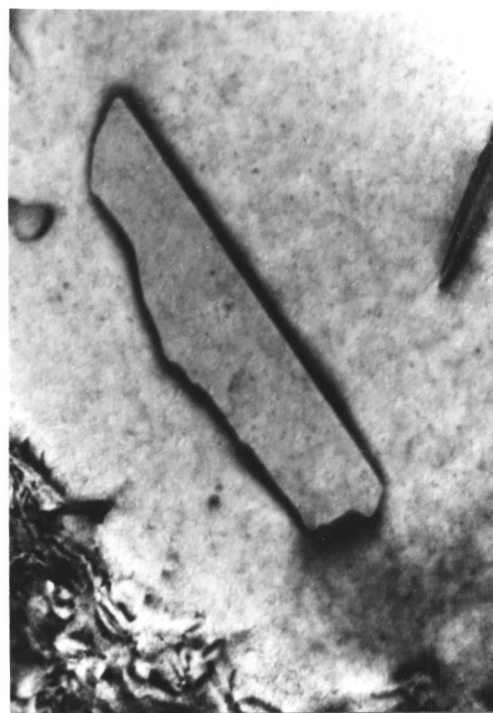
dipoles will hinder the movement of other superdislocations and may generate more jogs and produce more dipoles when intersected by gliding dislocations. This process was suggested by Thornton, Davies and Johnston (1970) to explain the work hardening of superalloys by what they termed 'debris hardening'.

### 5.2.3 Large planar defects

Large planar defects of the type shown in figure 5.10 were observed in foils cut on (111). g.b analyses coupled with line vector determination and fault contrast studies have shown that defects exhibit the contrast expected from extrinsic superlattice stacking faults lying parallel to the plane of the foil. The faults were bounded by a loop of  $a/3\langle 211 \rangle$  dislocation (fig. 5.10), showing that they were formed by a shear process and not by the agglomeration of vacancies or interstitial atoms. The latter processes would produce an  $a/3\langle 111 \rangle$  bounding dislocation.

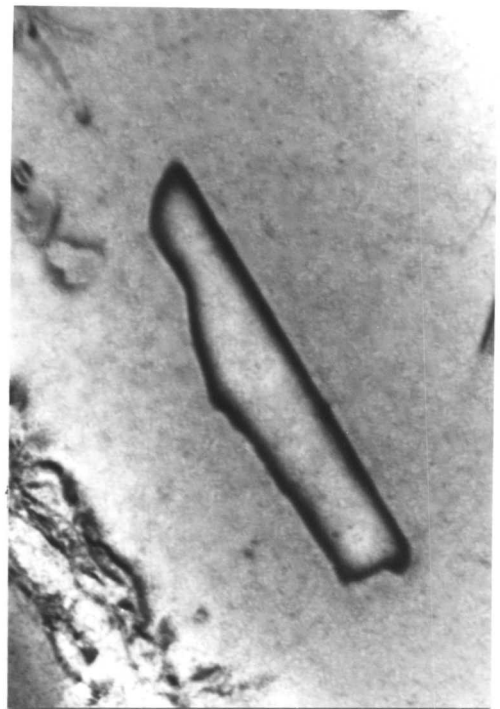
Superlattice stacking faults of this type have been frequently observed in  $L1_2$  for example by Enami and Nenno (1968), Giamei, Oblak, Kear and Rand (1970), Oblak and Kear (1971), Takeuchi et al. (1973), Howe et al. (1974), Pak, Saburi and Nenno (1976) and Suzuki et al. (1979). All these workers report that the majority of the defects observed were intrinsic. The dislocation line vector was determined for all the SSFs analysed in this investigation and it was shown that the majority of faults were extrinsic. A possible reason for this discrepancy is given below.

This type of planar defect can be formed by the following mechanism proposed by Suzuki et al. (1979). The mechanism is inaugurated by the immobilisation of one, usually the trailing one, of the  $a/2\langle 110 \rangle$  dislocations forming the superdislocation. Takeuchi and Kuramoto (1973) suggested that this could occur by the cross-slip of a short segment of dislocation onto an  $\{001\}$  plane. Alternatively the trailing dislocation may become jogged while the other does not. Whatever the reaction, a part of the trailing



(a)

$20\bar{2}$  ↗



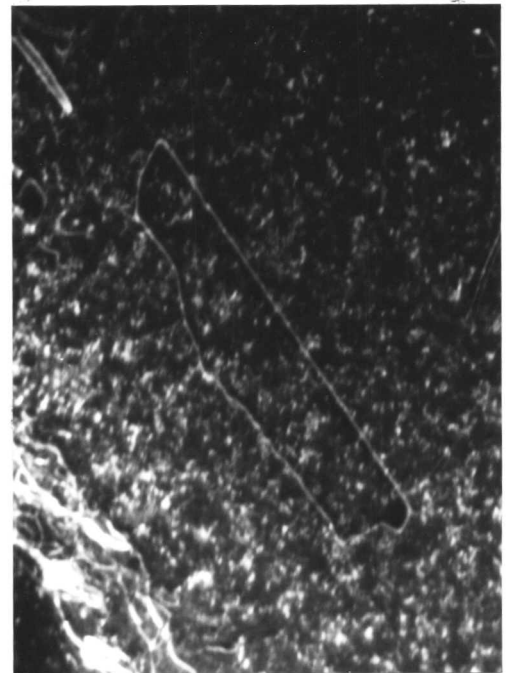
(b)

$20\bar{2}$  ↘



(c)

$1\bar{1}\bar{1}$  ↘



(d)

$20\bar{2}$  ↗

150 nm

Fig. 5.10. Bright field TEM  $\pm g$  pair (a and b) and two  $W_{(g,3g)}$  weak beam dark field TEM micrographs showing a large SESF. (a) and (b) show that the SESF is bounded by a dislocation loop; in this case an  $a/3[11\bar{2}]$  shear dislocation which is shown in (d). Contrast from the fault lying parallel to the foil surface is shown in (c). (foil normal:  $\sim[111]$ ).

dislocation becomes pinned, the leading dislocation glides on extending the APB (fig. 5.11a). Suzuki et al. suggest that the extension of the APB was aided by the line tension of the superdislocation attempting to straighten itself; otherwise the force required to separate the superdislocation would be too large for the reaction to occur. After a certain extension it becomes energetically favourable for the APB to transform to an intrinsic or extrinsic SSF by nucleating an  $a/6\langle 211 \rangle$  dislocation loop or by the splitting of the bounding  $a/2\langle 110 \rangle$  dislocation into an  $a/3\langle 211 \rangle$  partial and an  $a/6\langle 211 \rangle$

e.g. 
$$a/2[10\bar{1}] = a/3[11\bar{2}] + a/6[1\bar{2}1] \quad \text{eqn. 5.1}$$

The superdislocation must continue to glide forward dragging out an SSF bounded by an  $a/3\langle 211 \rangle$  partial dislocation which is apparently locked in position by the Kear-Wilksdorf mechanism (fig. 5.11b) (Pak et al., 1976). To form the defect shown in figure 5.10 the fault would need to be pinched off at some point (fig. 5.11c).

Many SESF defects of this type were observed in deformed and annealed foils of alloy A, while very few were seen in alloys D and G. It is proposed that formation of a very thin layer of  $\text{Ni}_3\text{Ti}$  occurs at this type of defect thus promoting the formation of defects with extrinsic characteristics rather than those with intrinsic characteristics observed by other workers. This is possible because SESFs are equivalent to seven layers of the hexagonal  $\text{Ni}_3\text{Ti}$  structure (4.2.4). Titanium may diffuse to the faults and stabilise them by forming a very thin layer of  $\text{Ni}_3\text{Ti}$ . (Heterogeneous precipitation of  $\text{Ni}_3\text{Ti}$  on stacking faults has previously been reported in the Ni-base alloy Nimonic 901 by Oblak, Owczarski and Kear (1971).) The formation of  $\text{Ni}_3\text{Ti}$  on the fault plane would effectively pin the  $a/3\langle 211 \rangle$  dislocation. It could also aid fault growth by assisting the passage of the leading dislocation. If this mechanism does operate it could be significant that the lower titanium alloy contains fewer defects. The likelihood of this pinning mechanism occurring and its effect on the SSF

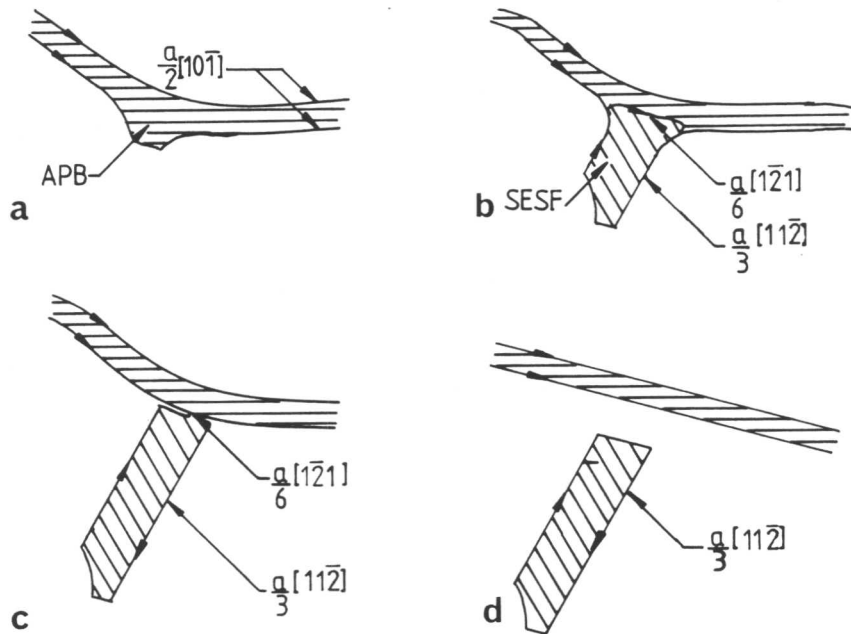


Fig. 5.11. Schematic illustration showing the proposed mechanism for the formation of a large SESF from a moving superlattice dislocation. See text for details. (After Suzuki et al., 1979).

energies are discussed in 6.3; its effect on the deformation mechanism is discussed in chapter 7.

Because these defects were locked in a metastable condition it was impossible to use them to evaluate the SSF energies. It is expected that defects of this type will slow the passage of superdislocations through the  $\gamma'$  and thereby assist the strengthening of the material.

### 5.3 Rectangular Networks formed by Dislocations with Burgers Vectors which Intersect at $90^\circ$

#### 5.3.1 Theoretical arrangement

Rectangular or square networks will occur in  $L1_2$  when two different screw superdislocations with perpendicular Burgers vectors intersect on the same or different  $\{111\}$  planes. The networks formed will appear rectangular on both  $\{001\}$  and  $\{111\}$  planes as shown in figure 5.12. No interaction can occur between perpendicular dislocations to form SSFs but it is possible for the APB fault vectors to cancel out to produce an area of unfaulted crystal.

#### 5.3.2 Square networks on $\{111\}$

Square and rectangular networks have been frequently observed in the  $\gamma'$  of alloys A-G by TEM. Stereo pairs have produced qualitative evidence for the existence of two different rectangular networks. One which has a stepped configuration is discussed below; the other, which is coplanar, is discussed in 5.3.2.

Analysis of the dislocations constituting the square network shown in figure 5.13 shows that the network was formed by an interaction between  $a[1\bar{1}0]$  screw superdislocations on  $\{11\bar{1}\}$  and  $a[110]$  screw superdislocations on  $\{1\bar{1}1\}$ . No dissociation of the  $a/2\langle 110 \rangle$  dislocations constituting the superdislocations was observed and was therefore assumed to be negligible.

The interaction occurred by the passage of one  $a/2\langle 110 \rangle$  dislocation

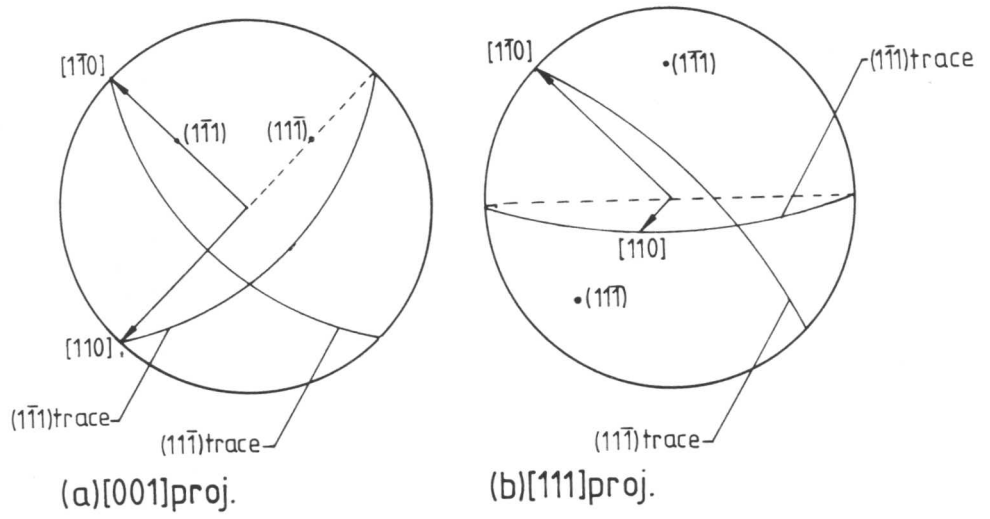


Fig. 5.12. Stereographic projections on [001] (a) and [111] (b) showing that screw dislocations with Burgers vectors at  $90^\circ$  produce networks which appear square or rectangular in both [001] and [111] TEM foils.

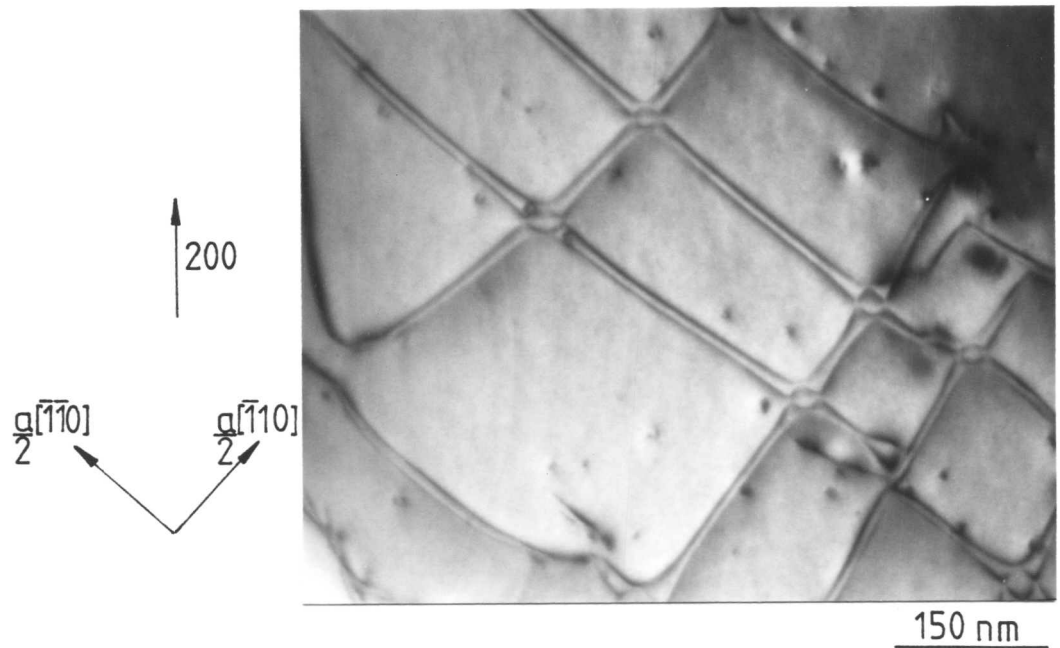


Fig. 5.13. Bright field TEM micrograph of a rectangular network of pairs of  $\frac{a}{2}[\bar{1}\bar{1}0]$  and  $\frac{a}{2}[\bar{1}\bar{1}0]$  dislocations on different {111} planes. (foil normal:  $\sim[001]$ ).

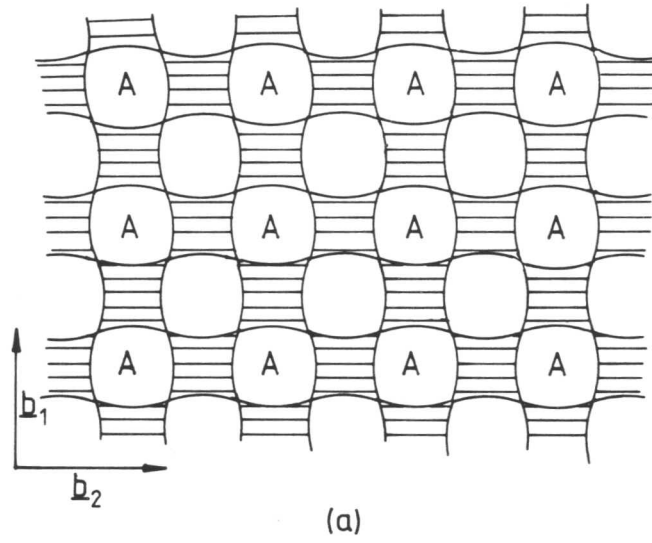
which created an APB; the next dislocation to pass will be perpendicular to the first and will destroy the APB, producing an unfaulted region. The unfaulted region (marked A on figure 5.14) must be a non-planar saddle point with the APBs on either side twisted slightly from their glide planes as shown in figure 5.14(b). Region A is perfectly stacked and as such is more stable than the APB so the region A will extend as much as possible to reduce the network energy. This explanation would produce the structures observed in deformed and annealed specimens (fig. 5.13).

It is probable that the interaction described above could only take place at high temperature when the dislocations are very mobile. Because the unfaulted region is formed the configuration will become sessile once formed, particularly when the temperature is lowered, thus explaining the large number of experimental observations of this unusual network. The stepped square networks observed had a large mesh size which allowed the superdislocations to adopt their equilibrium spacing on the  $\{111\}$  glide plane, there not being enough of a driving force to make cross-slip onto the lower energy  $\{001\}$  planes favourable. APB energies for pure screw dislocations were determined from portions of superdislocations well away from the points of intersection, thereby avoiding any change in dislocation spacing caused by the unfaulted region (6.2).

### 5.3.3 Square networks on $\{001\}$

Co-planar square dislocation networks were observed on  $(001)$  planes in foils with  $[001]$  normals (fig. 5.15). These networks were meshes of  $a[110]$  and  $a[\bar{1}\bar{1}0]$  screw superdislocations on  $[001]$ .

As described in 5.3.2 an unfaulted region is created as shown on an  $[001]$  section through  $L1_2$  in figure 5.16. The unfaulted region on  $[001]$  expanded until equal amounts of APB and unfaulted region constituted the network (fig. 5.14a). Because of the considerably lower APB energy on  $\{001\}$  planes the  $a/2\langle 110 \rangle$  dislocations are not so tightly constrained as those on  $\{111\}$  planes; consequently the unfaulted regions grow considerably larger



$$b_1 = \frac{a[110]}{2} \quad b_2 = \frac{a[\bar{1}\bar{1}0]}{2}$$

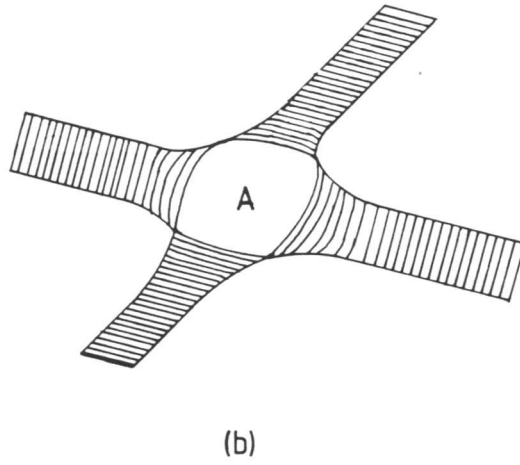


Fig. 5.14. Schematic diagrams showing plan view of a square network (a). If the network lies on two  $\{111\}$  planes the unfaulted region (A) is an unfaulted non-planar saddle point (b). See text for details.

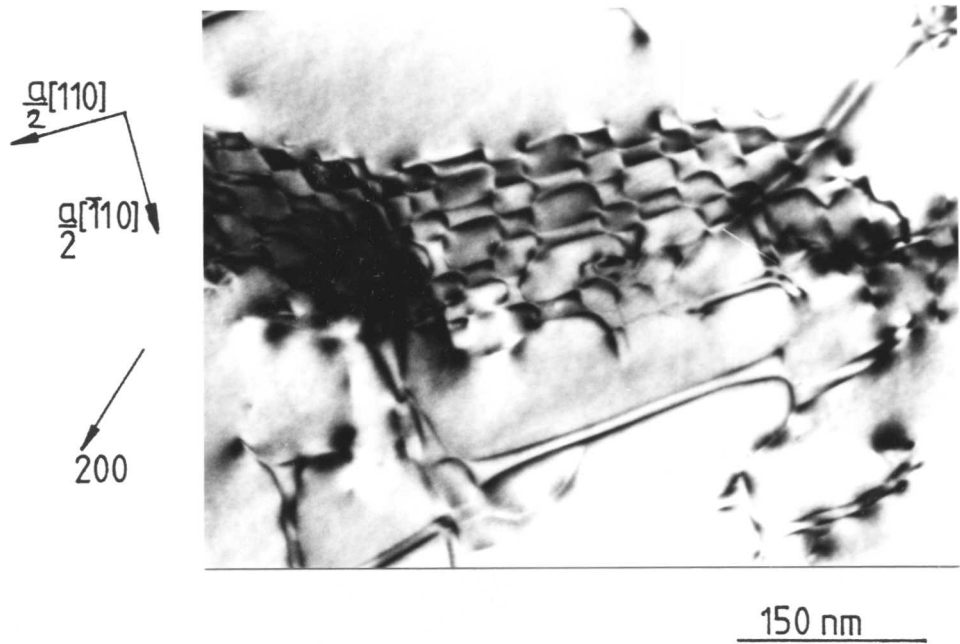


Fig. 5.15. Bright field TEM micrograph showing a square network of screw dislocations on (001). (foil normal:  $\sim[111]$ ).

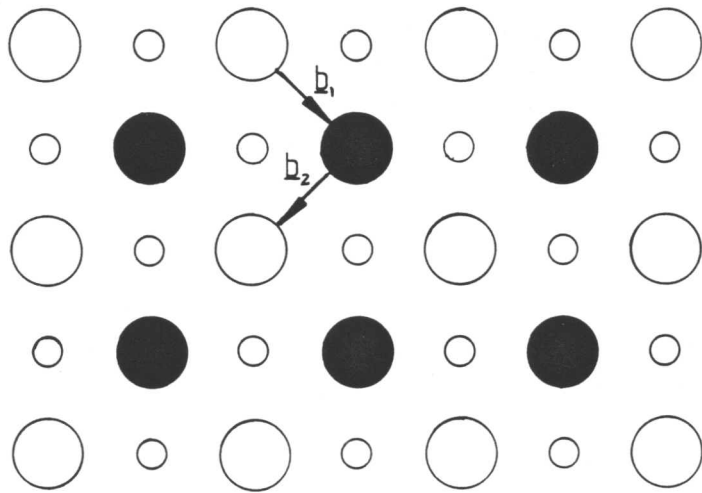


Fig. 5.16. Plan view of (001) planes in  $L1_2$  showing that the passage of a single  $a/2[\bar{1}10]$  dislocation will create an APB, but that the passage of  $a/2[110]$  will restore perfect stacking to form the unfaulted region shown in figure 5.14.

$$b_1 = a/2[\bar{1}10], b_2 = a/2[110].$$

than those on  $\{111\}$  planes. This network is very similar to that proposed by Czernickow, Gudas, Marcinkowski and Weng Feng Tseng (1971). Once the configuration has achieved its lowest energy configuration with approximately equal areas of APB and unfaulted crystal it will be effectively sessile.

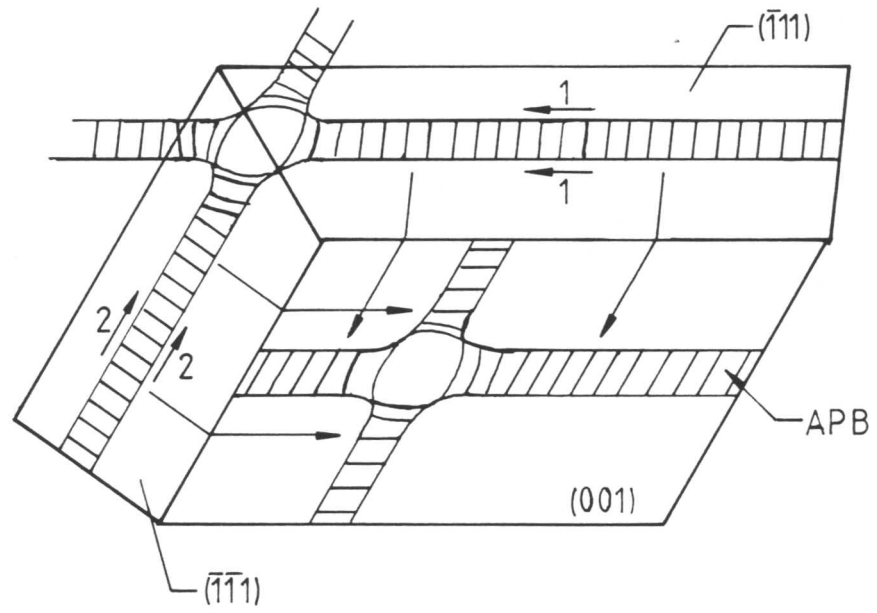
Networks on  $\{001\}$  may be formed either by glide of screw superdislocations on  $\{001\}$  or by cross-slip from  $\{111\}$ . The first mechanism seems highly unlikely due to the difficulty of slip on the non-close packed  $\{001\}$  planes (as stated in 4.3.2). It seems more likely that the networks are created by cross-slip of the  $\{111\}$  networks.  $\{111\}$  networks obviously have a high energy due to the non-planar APBs and saddle points. At the annealing temperature the  $a/2\langle 110 \rangle$  dislocations will be constricted so they will provide little barrier for cross-slip to  $\{001\}$ . Cross-slip from  $\{111\}$  to  $\{001\}$  in  $L1_2$  alloys was first suggested by Kear (1966).

If the activation for cross-slip is overcome, networks on  $\{001\}$  can form as shown schematically in figure 5.17. Limited glide will occur on  $\{001\}$  to equilibrate the structure to that shown in figure 5.15. It is proposed that the cross-slip of  $\{111\}$  networks onto an  $\{001\}$  plane will occur more readily for fine mesh networks than for coarse mesh networks. The superdislocations in the fine mesh networks on  $\{111\}$  planes are distorted and cannot adopt an equilibrium configuration on the initial glide plane. This distortion may provide some of the driving force for cross-slip onto  $\{001\}$  planes.

The mesh size of  $\{001\}$  networks was too small for the APB regions to adopt an equilibrium spacing between the unfaulted regions: consequently accurate dislocation spacings could not be measured, thus precluding the evaluation of the  $\{001\}$  APB energies.

#### 5.4 Discussion and Conclusions

The dislocation interactions discussed in this chapter are less significant to the calculation of defect energies than the supernodes



$$1 = \frac{a}{2} [110]$$

$$2 = \frac{a}{2} [1\bar{1}0]$$

Fig. 5.17. Schematic illustration showing cross-slip from a square network on  $\{111\}$  planes to form a square network on  $[001]$ .

reported previously. However, many APB energy measurements were made from isolated superdislocations and rectangular superdislocation networks, and the identification of dipoles meant that no incorrect dislocation spacings were measured, thus avoiding spurious APB energy results.

Some authors have suggested that the interactions reported here are of considerable significance to the strengthening of superalloys. Thornton et al. (1970) proposed that the glide of jogged superdislocations produced dislocation debris, such as loops, which they applied to explain the unusual work hardening characteristics of superalloy materials (Copley and Kear, 1967). There has subsequently been considerable controversy in the literature as to whether debris hardening is a significant strengthening mechanism. Staton-Bevan and Rawlings (1975a and b) found that their flow stress results correlated more closely with the mechanism proposed by Davies and Stoloff (1965) which is based solely on the traditional model for dislocation particle interaction where second phase particles pin the dislocations. More recently, Takeuchi and Kuramoto (1973) have introduced a third element into the work hardening model by proposing that cross-slip of short segments of one or both of the  $a/2\langle 110 \rangle$  dislocations of a superdislocation onto  $\{001\}$  during deformation has a major strengthening role.

In complex superalloys with large volume fractions of  $\gamma'$  it is unrealistic to adopt the premise that only one dislocation interaction or strengthening mechanism is effective. In this investigation it was noted that dislocations generated in the  $\gamma$  have great difficulty entering the  $\gamma'$  without dislocation climb occurring, showing that a significant strengthening effect is being produced by the Davies and Stoloff (1965) model. It was also noted that once inside the  $\gamma'$  dislocation interactions occurred to form networks which will further act to provide strength by reducing dislocation motion. Dislocation 'debris' in the form of loops and dipoles was also produced showing that the model of Thornton et al. (1970) was also

operative. Large flat stacking fault defects were also observed. It is likely that these occur as a consequence of the slip of small segments of dislocation onto {001} as proposed by Takeuchi and Kuramoto (1973). It is almost certain that all three of these mechanisms will play some role in the strengthening of alloys A to G.

In addition to these established strengthening mechanisms it is proposed that a further mechanism may be having some effect. The large flat extrinsic stacking faults reported in 5.2.3 have the  $DO_{24}(\text{Ni}_3\text{Ti})$  structure: it is thought that during creep deformation enough time would be available for the diffusion of Ti to the fault and the formation of a very thin planar precipitate of  $\text{Ni}_3\text{Ti}$ . This precipitate will strengthen the alloy by pinning or obstructing the passage of superdislocations. It was noted that the higher Ti containing alloy (A) contained more planar faults than either of the other alloys, indicating that if Ti is stabilising the SSFs, the effect is stronger at higher Ti contents. This effect is discussed more fully with reference to diffusion data, stress rupture data from alloys A, D and G, and SSF and APB energy measurements from hexagonal networks in chapters 6 and 7.

## CHAPTER 6

### MEASUREMENT OF ANTI-PHASE BOUNDARY ENERGY

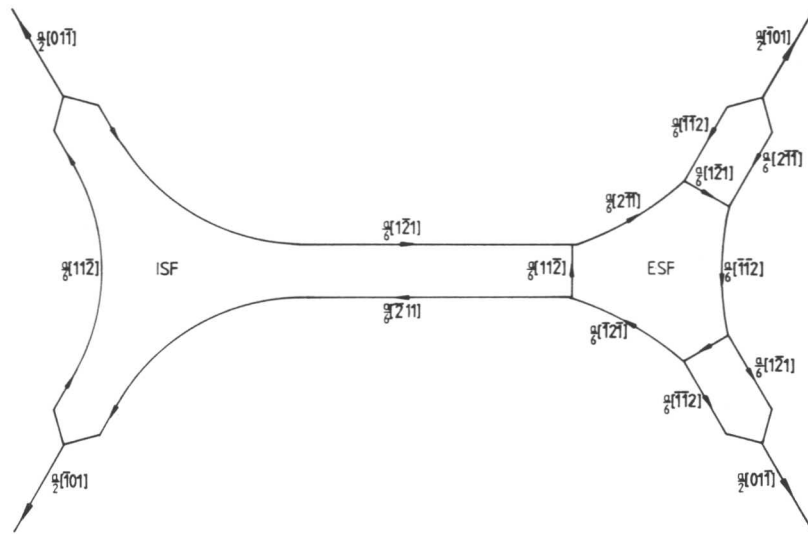
### AND SUPERLATTICE STACKING FAULT ENERGY

#### 6.1 Introduction

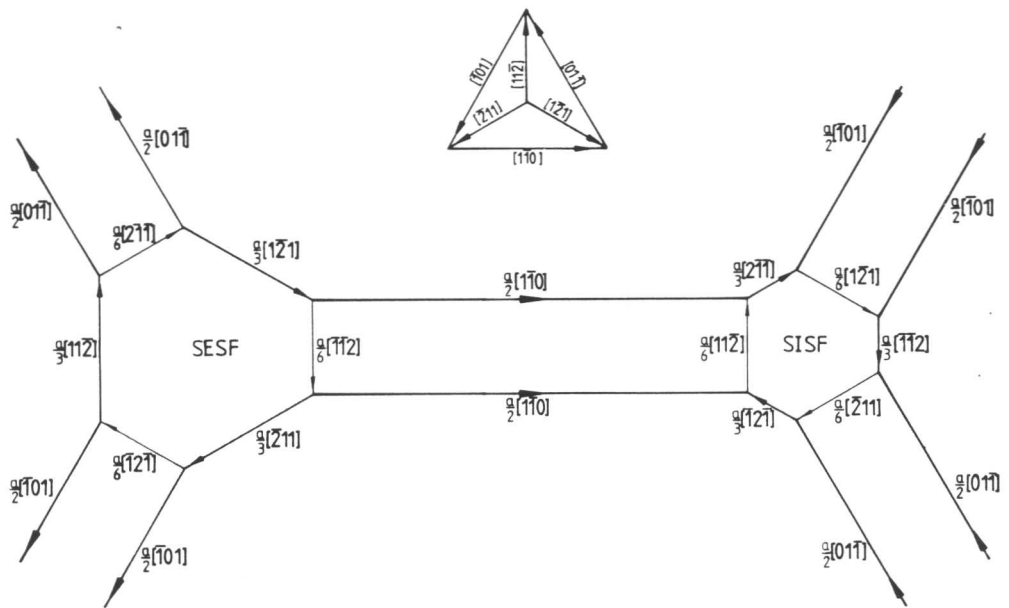
This chapter presents the experimental techniques employed and the values obtained for the anti-phase boundary (APB) energies and superlattice stacking fault (SSF) energies of alloys A, D and G. The APB energies were determined from dislocation spacing measurements made on pure screw superdislocations. This is described in 6.2.1. The results are presented and discussed in 6.2.3.

The SSF energies were considerably more difficult to measure than the APB energies. Although it is known that the shear of gamma prime can occur by pairs of  $a/3\langle 211 \rangle$  dislocations bounding ribbons of SSF (Kear et al, 1968), no evidence for this was found during this investigation. Consequently the SSF energies could not be determined by the same method as the APB energies. Instead hexagonal dislocation networks containing extended nodal points were produced by cold deformation and annealing (chapter 4.5). These extended supernodes (fig. 6.1b) were superficially similar to extended nodes in FCC materials (fig. 6.1a), but there were significant differences in the types of dislocations and faults present. Consequently the well established techniques of stacking fault energy measurements (for details see the reviews by Christian and Swann, 1965, Ruff, 1970, and Amelinckx, 1979) were found to be inapplicable to the evaluation of SSF energy from supernodes.

A new technique has been developed by Rae and Hillier (1984) in which the SSF energy can be evaluated from a supernode by calculating the



(a)



(b)

Fig. 6.1. Illustration showing an intrinsic and an extrinsic node in FCC (a) and in  $L1_2$  (b).

force exerted on one dislocation by the stress fields of the other dislocations when the superdislocation spacing is known; this is described in 6.3.1. The method has been used to evaluate SSF energies in alloys A, D and G. These results are discussed in 6.3.4.

The significance of the results with respect to the creep behaviour of superalloys is discussed in chapter 7.

## 6.2 Anti-Phase Boundary Energy Measurement

### 6.2.1 Theory

The energy of an APB can be evaluated from the equilibrium spacing between the two bounding  $a/2\langle 110 \rangle$  dislocations, since the repulsive force between the dislocations is balanced by the APB energy drawing them together.

According to Eshelby, Read and Shockley (1953) the non-vanishing stress components,  $\sigma_{ij}$ , on a straight dislocation in an anisotropic medium are:

$$\sigma_{\theta z} = \frac{c_{44} b}{2\pi\beta r} \quad \text{eqn. 6.1(a)}$$

and

$$\sigma_{rz} = \frac{c_{44}}{2\pi\beta} \frac{b}{r} \frac{(1-\beta^2) \cos\theta \sin\theta}{(\cos^2\theta + \beta^2 \sin^2\theta)} \quad \text{eqn. 6.1(b)}$$

where

$$\beta^2 = 2c_{44} / (c_{11} - c_{12}) \quad \text{eqn. 6.1(c)}$$

$c_{ij}$  are the elastic constants,  $b$  is the magnitude of the dislocation Burgers vector,  $r$  is the distance from the dislocation and  $\theta$  is the angle between the dislocation line vector,  $\underline{u}$ , and the Burgers vector.

For a pure screw dislocation  $\theta$  is zero; therefore  $\sigma_{rz} = 0$ , so the only stress component is:

$$\sigma_{\theta z} = \frac{b}{2\pi r} \left[ \frac{c_{44} (c_{11} - c_{12})}{2} \right]^{\frac{1}{2}} \quad \text{eqn. 6.2}$$

Consider the interaction between two parallel co-planar screw dislocations bounding an APB. A dislocation lying at the origin of a co-ordinate system along the z direction, as shown in figure 6.2, exerts a tangential shear stress, which is given by eqn. 6.2, on the APB plane if end effects are ignored. The force per unit length on a parallel screw dislocation at  $P(r, \theta)$  is normal to  $\sigma_{\theta z}$  and  $O$ , and is therefore along  $OP$ . It has the magnitude:

$$F = \frac{b^2}{2\pi r} \left[ \frac{c_{44}(c_{11} - c_{12})}{2} \right]^{\frac{1}{2}} \quad \text{eqn. 6.3}$$

where  $F$  is the force per unit length on the dislocation.

The energy of the APB,  $\gamma_A$ , between the dislocations can thus be determined by examining the work done on moving the dislocation  $S_x$ . Equation 6.3 was used extensively to evaluate APB energies from

superdislocation spacings measured from TEM micrographs.

Values for the elastic constants,  $c_{ij}$ , were supplied by Rolls-Royce Ltd. They were calculated from measured sound velocities in alloy A. As there are only small differences between alloy compositions and lattice parameters, these values have also been taken to be typical of alloys D and G. Unfortunately, no specific values of  $c_{ij}$  in  $\gamma'$  are available, but, as the alloys contain in excess of 0.6 volume fraction of  $\gamma'$ , the bulk alloy values were considered acceptable for use in the calculation of APB energies. The  $c_{ij}$  values used were determined at 300K and could be in error by up to 10%. They were:

$$\begin{aligned} c_{11} &= 2.5 \times 10^{11} \text{ Pa} \\ c_{12} &= 1.633 \times 10^{11} \text{ Pa} \\ c_{44} &= 1.154 \times 10^{11} \text{ Pa} \end{aligned}$$

$$\text{The anisotropy factor, } A = \frac{2c_{44}}{c_{11} - c_{12}} = 2.66 \quad \text{eqn. 6.4}$$

The only other available values for the elastic constants of  $\gamma'$  were published

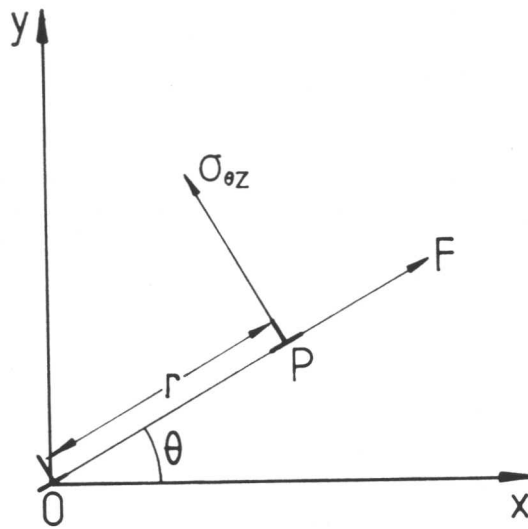


Fig. 6.2. Illustration showing the configuration used to determine the force between two  $a/2\langle 110 \rangle$  dislocations (at O and P) bounding an APB as described in the text.

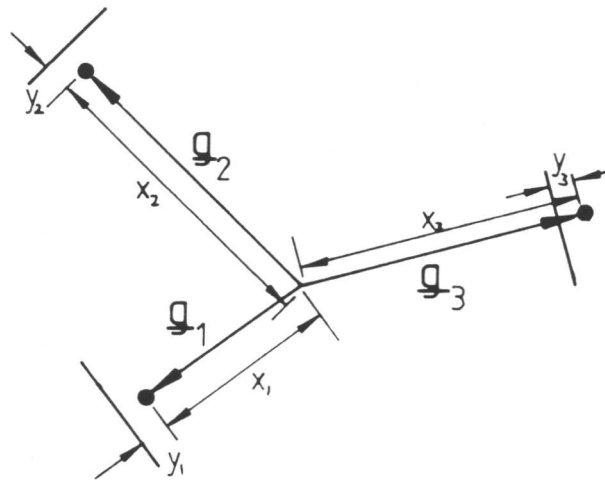


Fig. 6.3. Illustration showing the method used to evaluate the electron beam direction,  $\underline{B}$ , from a diffraction pattern with three identifiable reflections.

The beam direction

$$\underline{B} = \alpha_1 |\underline{g}_1|^2 (\underline{g}_2 \times \underline{g}_3) + \alpha_2 |\underline{g}_2|^2 (\underline{g}_1 \times \underline{g}_3) + \alpha_3 |\underline{g}_3|^2 (\underline{g}_1 \times \underline{g}_2)$$

where  $\alpha_i = \frac{(x_i + 2y_i)}{x_i}$

by Ono and Stern (1969). For pure Ni<sub>3</sub>Al containing less than 0.1% impurities, they found  $c_{11}$  and  $c_{12}$  to be about 20% lower and  $c_{44}$  to be the same as the values used in this investigation. This difference probably arises because they were studying an alloy with a smaller lattice parameter and lower density from the  $\gamma'$  in alloys A, D and G. Ono and Stern showed that the elastic constants do not vary significantly with temperature between 83K and 600K. As a result of this observation it was decided that it was reasonable to use the elastic constants measured at 300K to evaluate the APB energy at higher temperatures in the absence of any more detailed data.

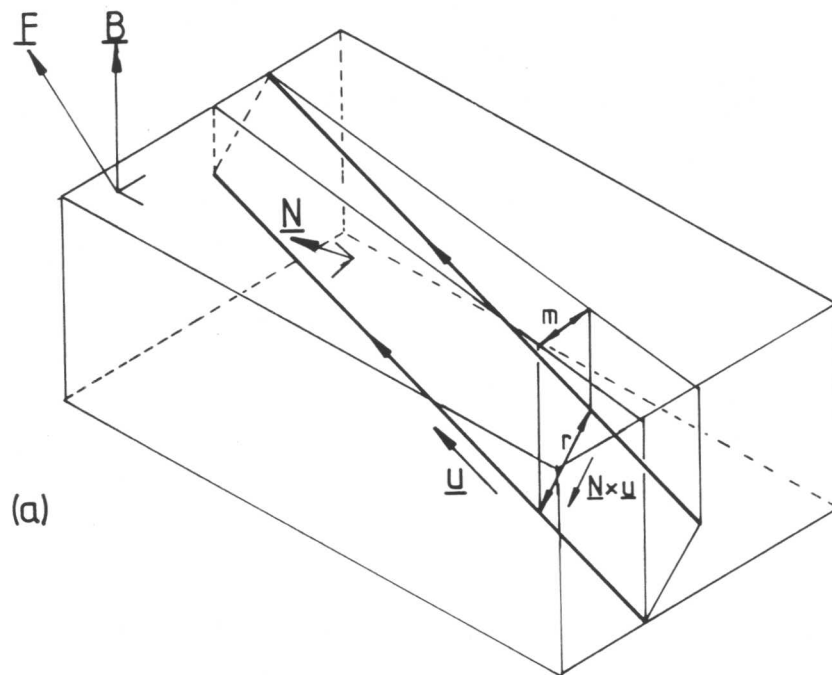
### 6.2.2 APB energy measurement

To evaluate the APB energy it was necessary to measure the true dislocation spacing,  $r$ , and to identify the bounding dislocations. The Burgers vectors were obtained by using the TEM techniques described previously (3.3.5): for dislocations separating APB from unfaulted crystal they are  $a/2\langle 110 \rangle$ . The magnitude of  $b$  calculated using the average lattice parameter of alloys A, D and G (table 2.4) is 0.253nm.

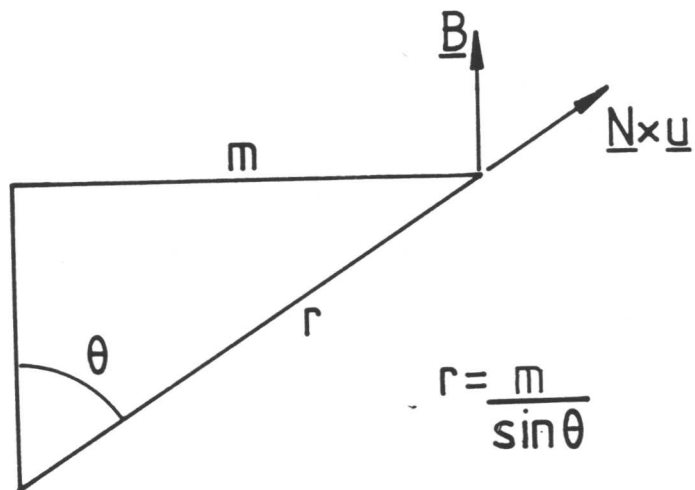
In most cases the anti-phase boundary plane was at an angle to the electron beam direction,  $\underline{B}$ . Consequently, the measured superdislocation spacing,  $m$ , was only an apparent value. To evaluate the true spacing,  $r$ , the electron beam direction,  $\underline{B}$ , and the plane normal of the superdislocation,  $\underline{N}$ , are required in addition to the dislocation line vector,  $\underline{u}$ .  $\underline{B}$  was evaluated following the technique described by Ryder and Pitsch (1968) which is shown in figure 6.3.  $\underline{N}$  was found by the trace analysis of dislocation pairs and stereo imaging. In some cases tilting experiments were also employed.

Simple geometry was then used to find  $r$ . Figure 6.4 shows that:

$$r = \frac{m}{\sin\theta} \quad \text{eqn. 6.5(a)}$$



(a)



(b)

Fig. 6.4. Illustration showing the method used to evaluate the true spacing,  $r$ , of a superdislocation from the apparent dislocation spacing,  $m$ .  $\underline{B}$  is the electron beam direction,  $\underline{N}$  is the APB normal,  $\underline{u}$  is the dislocation line sense and  $\theta$  is the angle between  $\underline{B}$  and  $\underline{N} \times \underline{u}$ . A schematic representation of the APB in the foil is shown in (a) and the geometrical configuration is shown in (b).

where

$$\sin\theta = \underline{B} \cdot (\underline{N} \times \underline{u}) \quad \text{eqn. 6.5(b)}$$

and  $\underline{B}$ ,  $\underline{N}$  and  $\underline{u}$  are unit vectors. This value of  $r$  was substituted in eqn. 6.3 to evaluate the APB energy.

### 6.2.3 Results and discussion

The APB energy results are shown in figure 6.5. The individual true dislocation spacings and APB energy values from each of the analysed networks are presented in appendix E. The results are summarised in table 6.1 which shows that the average APB energy for alloys A, D and G is  $83 \pm 20 \text{ mJm}^{-2}$ .

There appears to be no significant variation in the APB energy of  $\gamma'$  with titanium content in single crystal superalloys containing between 1.8 and 2.7 at.% titanium. There is, however, a large range of APB energies for each alloy. No obvious reason was found for this range which amounted to a difference of about 6nm in dislocation pair spacing between the lowest and the highest values. This is considerably greater than the maximum error in spacing measurement. One explanation is that it may be related to the behaviour of the dislocations during cooling of the specimens after annealing. The specimens were air cooled from 1173K and it is suggested that some glide of the dislocations bounding the APBs may have occurred in an attempt to maintain the equilibrium spacing at lower temperatures. It is thought that cooling was too rapid for the respacing to have a major effect on the APB energies; if there was any effect it would act to produce a slightly higher APB energy than that at 1173K because a smaller dislocation spacing was expected at room temperature. The possibility of the contraction of superdislocations means that it is impossible to relate the measured energies to a particular temperature but it is assumed that the values are typical of 1173K as any movement of the dislocations will have been limited by the more stable parts of the networks.

Table 6.1. Summary of the Anti-phase Boundary Energies

	Alloy		
	G	D	A
$\gamma'$ Ti content (at.%)	2.8	3.3	3.9
Mean APB energy ( $\text{mJm}^{-2}$ )	87	78	83
Overall mean APB energy ( $\text{mJm}^{-2}$ )		83	
Standard deviation ( $\text{mJm}^{-2}$ )	20	17	15
Range of results ( $\text{mJm}^{-2}$ )	56-108	55-114	57-114

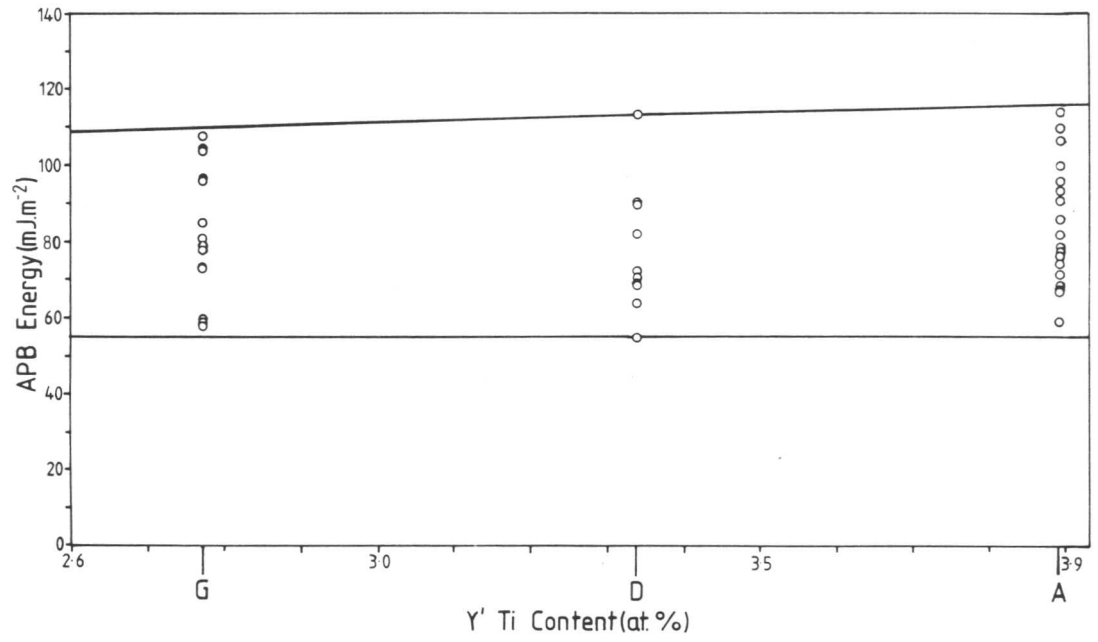


Fig. 6.5. The variation in APB energy with  $\gamma'$  titanium content for alloys A, D and G.

#### 6.2.4 Comparison with the results of other workers

In the past seventeen years many references have been made to the effect the APB energy may have on deformation in  $L1_2$  structures, for example, Copley and Kear (1967), Kear, Leverant and Oblak (1969), Kear et al. (1970), Leverant, Gell and Hopkins (1970 and 1971), Leverant and Kear (1970), Raynor and Silcock (1970), Thornton et al. (1970), Brown and Ham (1971), Leverant, Kear and Oblak (1973), Takeuchi and Kuramoto (1973), Kear (1974), Staton-Bevan and Rawlings (1975a and b), Noguchi, Oya and Suzuki (1981), and Pope and Ezz (1984). Since so much work has been reported, it is surprising that there are so few quantitative APB energy data available.

Some values have been measured, the most popular value quoted in recent papers (e.g. Pope and Ezz, 1984) being that measured in the field ion microscope (FIM) by Taunt and Ralph (1974). These authors measured a superdislocation spacing of 3nm (considerably smaller than the present data) which corresponds to a higher APB energy of between 250 and 350  $\text{mJm}^{-2}$ . This value is close to the values of 300  $\text{mJm}^{-2}$  and 254  $\text{mJm}^{-2}$  calculated theoretically for perfectly ordered pure  $\text{Ni}_3\text{Al}$  by Taunt (1973) and Copley and Kear (1967) respectively. Taunt and Ralph performed their experiments on a highly ordered pure  $\text{Ni}_3\text{Al}$  at about 77K, and they consequently gained the expected good agreement with the theoretical value.

It is unrealistic to suggest that this value is typical of the APB energy of a highly alloyed commercial superalloy in the region of 1000K. Alloying of the  $\gamma'$  means that atoms other than Ni and Al will occupy adjacent sites in the  $L1_2$  lattice. Consequently the interatomic forces will be different from those in  $\text{Ni}_3\text{Al}$  as will the change in those forces when an APB is created. Also, as temperature is increased, entropy increases, order decreases and so does APB energy. This is shown in the calculated value of 164  $\text{mJm}^{-2}$  quoted by Copley and Kear (1967) for  $\text{Ni}_3\text{Al}$  with a long range order parameter of 0.803 (they calculated the APB

energy of fully ordered  $\text{Ni}_3\text{Al}$  to be  $254\text{mJm}^{-2}$ ). As a consequence of these two factors the APB energy of most superalloys is expected to be lower than that of perfectly ordered  $\text{Ni}_3\text{Al}$ .

Experimental values measured indirectly by various means have been reported by Brown and Ham (1971). These values are mainly from small  $\gamma'$  volume fraction, low alloy superalloys with gamma prime particle sizes less than  $0.1\mu\text{m}$ . Energies calculated using equations 2.63 and 2.64 from Brown and Ham (1971) were mostly between  $150$  and  $200\text{mJm}^{-2}$ . The most important of these are due to Raynor and Silcock (1970) who reported that for a mixture of superalloys and stainless steels the APB energy of gamma prime increased with titanium additions concluding that the Ti/Al ratio affected the APB energy. This conclusion was drawn although other alloying elements in the compositions, particularly Ni and Fe, were changed by a considerably greater margin than the titanium. Raynor and Silcock's observations are contrary to the findings of this investigation; probably because they were comparing radically different alloys rather than a systematic set where one element (Ni) was replaced by another (Ti), as in this investigation. Another factor contributing to the differences might be that Raynor and Silcock's alloys contain more Ti than Al, whereas alloys A, D and G contain more Al than Ti. It seems that the compositional differences in Raynor and Silcock's alloys have a considerable effect on their APB energies, although it is not certain that these differences are due to changes in Ti. It is concluded that the alloys studied by Raynor and Silcock are too widely different from alloys A, D and G for their APB energies to be usefully compared. This is supported by the results of Miller and Ansell (1977) who evaluated the APB energies for Ni-Cr-Al-Mo alloys and Ni-Cr-Al-Ti-Mo alloys where the titanium content was larger than the Al content. Using the techniques described by Brown and Ham (1971) they found that the APB energy of the alloys with titanium was  $200\text{mJm}^{-2}$  and for alloys without titanium the lower value of

$133\text{mJm}^{-2}$  was obtained.

Data from Ni-Al-Cr alloys (Hornbogen and Mukerjee, 1964 and Hornbogen, 1965) were reprocessed by Brown and Ham (1971) and gave APB energies of about  $90\text{mJm}^{-2}$ . These results are similar to the present data but the agreement may be fortuitous as the alloys studied are so different from one another. It does, however, appear that the presence of chromium alone considerably lowers the APB energy of  $\text{Ni}_3\text{Al}$ .

The first APB energy value quoted for a commercial superalloy was a value of  $150\text{mJm}^{-2}$  (Leverant and Kear, 1970). It was not stated how this value was obtained but it is close to the theoretical value quoted by Copley and Kear (1967). In a later paper, Leverant et al. (1973) stated that after creep deformation at 1023K the superdislocation spacing was too small to be measured from bright field electron micrographs, but that after creep deformation at 1133K the spacing could be measured and was found to be 9nm. They concluded that this single observation showed an effective drop in the local APB energy on  $\{111\}$  planes between 1023 and 1133K. In this investigation superdislocations were frequently observed after annealing at 1173K. Their spacings, measured using weak beam imaging, were found to be similar to the value quoted by Leverant et al. (1973) after deformation at 1133K.

From the results presented above it is clear that no systematic study of the way in which APB energy varies with alloy composition has been undertaken previously. APB energies have been measured in significantly different alloys using a wide range of techniques and it is impossible to compare results. Other than the result reported by Leverant and Kear (1970), no other values for the APB energy of Ni-base superalloys strengthened by large volume fractions of gamma prime have been reported before this investigation.

The APB measurement technique employed here involves the measurement of dislocation spacings. This method was first used by Marcinkowski,

Brown and Fisher (1961) on pure  $\text{Cu}_3\text{Au}$ . They also calculated the variation in spacing which could be expected with change in order and showed that a change of up to 8nm was possible for a given APB energy between the fully ordered state and the point at which ordering becomes negligible. It could be that the range of spacings measured in this investigation was due to a local change in the order. However, this is highly improbable because long homogenisation and annealing times used here were deliberately employed to produce uniformly ordered materials.

In summary, it has been shown that the APB energy of three single crystal superalloys does not seem to vary with titanium content. A range of values was found which is probably due to limited glide of superdislocations during cooling from the annealing temperature rather than regions of different order. The average APB energy was  $83\text{mJm}^{-2}$  (fig. 6.5); it has been assumed that this value is typical of 1173K.

The author is not aware of any data which directly relate APB energy to temperature. An experiment could be undertaken using a heating stage in the TEM which could be of great value to the prediction of superalloy deformation mechanisms. It would also establish whether there is a major change in APB energy between 1023K and 1133K as proposed by Leverant et al. (1973).

The evaluation of APB energies from measured dislocation spacings is the most direct and accurate method available, and it is suggested that this technique should be used to study the effect of other alloying elements on the APB energies of superalloys.

### 6.3 Superlattice Stacking Fault Energy Measurement

#### 6.3.1 Theory

A method (Rae and Hillier, 1984) has been developed which enables superlattice stacking fault (SSF) energies to be deduced from the supernode configurations described previously. The SSF energy per unit area is

related to the net force acting at point O on dislocation 6 of the configuration shown in figure 6.6. To do this, the stress field due to each screw dislocation segment forming the supernode is calculated using a different set of co-ordinate axes and these stresses are then resolved along the Z direction of the co-ordinate system attached to dislocation 6 to evaluate the total force on that dislocation. A detailed description of this process is given in appendix D.

All the stresses except that resulting from dislocation 3 act to expand the node by pulling it outwards. When the stresses due to these dislocations are taken to be positive, the stress due to dislocation 3 is negative. The total force per unit length which can be equated to the SSF energy acting on the supernode,  $\gamma_{SSF}$ , is:

$$F = [\sigma_1 + \sigma_2 - \sigma_3 + \sqrt{3}\sigma_4 + \sqrt{3}\sigma_5] \cdot b_6 = \gamma_{SSF} \quad \text{eqn. 6.6}$$

The expressions from appendix D are homogeneous in  $r$ , the dislocation spacing, and  $R$ , the internal dimension of the node. They can consequently be written in terms of  $R$  and the ratio  $r/R$  which will be termed  $\rho$ . The expression can be separated into a dimensionless geometrical function of  $\rho$  multiplied by  $1/R$ . The geometrical function depends only upon the shape of the node. If the total stress is multiplied by the Burgers vector of dislocation 6 ( $b_6 = \frac{\sqrt{2}a}{3}$ ) the force per unit length at the centre of the dislocation acting on the extended node is:

$$F = \frac{\mu a}{4\pi R} \frac{\sqrt{2}a}{3} G(\rho) \quad \text{eqn. 6.7}$$

This can be equated to the SSF energy so that:

$$\gamma_{SSF} = \frac{\mu a^2}{2\sqrt{6}\pi R} G(\rho) \quad \text{eqn. 6.8}$$

where  $\mu$  is the isotropic shear modulus and is equivalent to  $[C_{44}(C_{11} - C_{12})/2]^{\frac{1}{2}}$